

Wireless High power Conversion System for Hybrid Wind Turbines

Yang Teng

Department of Electronic and Electrical Engineering

University of Strathclyde

A thesis submitted for the degree of

Doctor of Philosophy

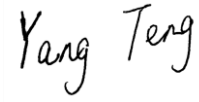
2026

Supervisor: Dr. David Campos Gaona & Prof. Olimpo Anaya Lara

Declaration

This thesis is the result of the author's original research. It has been composed by the author and has not been previously submitted for the examination which has led to the award of a degree.

The copyright of this thesis belongs to the author under the terms of the United Kingdom Copyright Acts as qualified by University of Strathclyde Regulation 3.50. Due acknowledgement must always be made of the use of any material contained in, or derived from, this thesis.

Signed: 

Date: 27 October 2026

Acknowledgements

First, thanks to my academic supervisor, Dr David Campos Gaona. Throughout these four years of my doctoral study, it is him to give me an opportunity to study a new PhD studying life as a researcher during Covid lockdown conditions. It is the one who leads and supports me to my successful progress and enhance my research capabilities, what is more, taught me how to work in balance and enjoy life. His patience, high knowledge reverse and time management not only attracts me but also becomes a vital part of my future growth. His enthusiasm and rigorous attitude on academic research make more confidence and face every challenge during my PhD research period. Also, thanks to my second supervisor, Olimpo Anaya Lara. His optimistic attitude gives me more motivation in my repeated experimental life.

To Dr Seyed Abolfazl Mortazavizadeh and Dr Reza Yazdanpanah, thanks to both who provided technical support as important as Dr David, they allowed me to have more academic thinking in the group.

My deepest thanks go to my parents, my aunt and uncle. Throughout my life, they gave me financial support to study abroad and opportunities to broaden my horizons. Also, set the right values and examples for me, giving me a clear understanding of the future development direction.

To my friends in my heart Xiao Du, your casual words and long-term vision saved me from the confusion before going abroad. I am appreciated and truly believe you provided me with spiritual comfort during my loneliness and helpless moment, which is of paramount importance to me.

To my best friend, Junxi Fu, thanks you to let me have a precious friendship, from senior high school until now. His unique vision and calm attitude when facing challenges that I admire. He makes unremitting efforts to support him also on the PhD path, which is worth learning. I sincerely hope that he can graduate successfully in the next few years and continue to pursue his dreams.

My heartfelt thanks extend to Dr Di Liu, Dr Shangen Tian, Dr. Fulin Fan. As my seniors, they give me the crucial advice and valuable experience, in some cases, they

have had a certain impact on my future career planning. Finally, thanks to all my colleagues and friends when studying abroad, Dr Guo Shi, Dr Yu Chen, Dr Helin Zhao, Dr Alan Huang, Shuxiu Cao, Qi Dong, Dr. Pannita Rajakrom Vincent, Kathy and Shiyao Yu, they are treasure and give me lot of happiness in my doctoral life. Wishing them a bright future.

Abstract

The X-ROTOR offshore wind-turbine concept places two secondary generator units on the rotating primary structure, requiring their electrical output to cross the continuously rotating rotor-to-tower boundary before connection to the stationary powertrain. Conventional slip rings can provide this function but retain sliding contact wear, contamination, inspection and brush-replacement requirements. This thesis investigates a contactless alternative based on a rotary transformer (RT) integrated with a dual active bridge (DAB) converter.

The electrical architecture of the X-ROTOR powertrain is first defined, including independent conversion of the two secondary generator outputs and their coordination through controlled DC interfaces. Inductive power transfer using an RT is selected for the rotating interface after comparison with conductive, capacitive and radiative alternatives. An integrated RT-DAB design method is then developed to relate winding voltage and current, core area, winding window, magnetic airgap, winding separation, fill factor, turns ratio, leakage and magnetising inductances, switching frequency and DAB phase shift. Five RT geometries are considered: the original radial structure, the application-driven NEW1 and NEW2 geometries, and two L-type alternatives.

The design is evaluated at three distinct investigation levels. A reduced-scale RT-DAB platform operates from a common 42 V DC source at 20 kHz with a nominal 1 mm assembled core-to-core airgap. The measured terminal voltages and fundamental power factor trends are reproduced by the prototype-matched model, although the simulated current magnitude remains lower than the measured value. An intermediate RT designed for 600 V RMS/100 kW at 2 kHz is used to compare two- and three-dimensional electromagnetic representations. Their calculated output powers are 98.832 kW and 98.787 kW, while larger differences occur in local flux density and core loss.

The analysis is subsequently extended to a three-phase MW-class linked field-circuit model. Controlled studies separate the effects of RT geometry, primary-to-secondary winding separation and fixed-window winding fill factor. Increasing winding

separation reduces coupling, current and transferred power, whereas reducing fill factor decreases the effective copper area and increases the represented winding loss. Under the retained reference conditions, NEW2 produces 991.3189 kW of output power with represented winding and core losses of 1.7865 kW and 8.7362 kW, respectively. The combined RT loss components correspond to approximately 1.06% of the output power. For the investigated 1:1 and 1:2 winding arrangements, the simulated secondary-to-primary RMS voltage ratios are 0.981 and 1.959.

The results support the RT-DAB as an electrical and electromagnetic solution for contactless power transfer across the X-ROTOR rotor-to-tower interface within the investigated conditions. The thesis contributes an application-specific RT-DAB architecture, the NEW1 and NEW2 rotary transformer geometries, and an integrated analytical, electromagnetic and linked field-circuit design and assessment method. Full-scale implementation requires further mechanical, thermal, insulation, environmental and lifetime qualification.

Contents

1 Introduction 1

1.1 Research Background 1

1.2 X-ROTOR Concept 4

1.2.1 Operating Roles and Reference Conditions 4

1.2.2 Overturning Moment and Primary Rotor Torque Balance 6

1.2.3 Projected Performance and Cost 7

1.2.4 Implication For Electrical Power Transfer 8

1.3 Rotating Electrical Interface and Slip Ring Maintenance 8

1.3.1 Sliding Contact Degradation Mechanisms 8

1.3.2 Comparable Rotary Electrical Interfaces 9

1.3.3 Slip Ring Operation at Low Speed and High Electrical Loading 10

1.3.4 Maintenance and Component Replacement Requirements 11

1.3.5 Requirements for the X-ROTOR Power Transfer Interface 12

1.4 Research Challenges, System Requirement and Objectives 13

1.4.1 RT Location and Preliminary Installation Envelope 14

1.4.2 Structural Load Path and RT Airgap Protection 15

1.4.3 System Level Design Requirements 16

1.4.4 Research Questions 18

1.4.5 Research Objectives 19

1.5 Research Contributions 20

1.6 Thesis Overview 21

1.7 Publications 22
1.8 Chapter references 23
2 Electrical Architecture and Selection of Contactless Power Transfer for the X-ROTOR 28
2.1 Introduction 28
2.2 Electrical Configuration of the X-ROTOR Powertrain 29
2.3 Secondary Generator Voltage and Converter Topology Selection 30
2.3.1 Generator Voltage Alternatives 30
2.3.2 Applicable Generator Side Converter Topologies 33
2.3.3 Selected Generator Side Arrangement 35
2.4 Electrical Power Flow and Coordination of the Two Secondary Generator Channel 36
2.4.1 Secondary Rotor Generation and Machine side Conversion 37
2.4.2 Complete Energy Conversion and Power Flow Path 37
2.4.3 Coordination Under Unequal Effective Inflow 38
2.5 Rotating Power transfer Interface: Conductive Reference and Contactless Alternatives 40
2.5.1 Electromagnetic Field Regimes and Transfer Distance 41
2.5.2 Far Field Wireless Power Transfer 43
2.5.3 Near Field WPT and Inductive Power Transfer (IPT) 43
2.5.4 Capacitive Power Transfer 45
2.5.5 Engineering Comparison of IPT and CPT 47
2.5.6 Selection of IPT for the X-ROTOR Interface 49
2.5.7 High Power WPT and RT Studies 50
2.6 Discussion 52
2.7 Chapter Summary 53

2.8 Chapter References 54
3 Design Methodology for RT-DAB Interface 62
3.1 Introduction 62
3.2 Analytical Design of Rotary Transformer 63
3.2.1 Fundamental Analytical Design Equations 64
3.2.2 Candidate RT Geometries 68
3.2.3 Half-Hat Type (NEW1) 72
3.2.4 Full-Hat Type (NEW2) 74
3.2.5 L-Type 1 and L-Type 2 75
3.3 DAB Converter Design and Operating Principles 77
3.3.1 Design Basis and Investigation Cases 78
3.3.2 Single-Phase DAB converter 80
3.3.3 Three-Phase DAB converter 82
3.4 Integrated RT-DAB Design Procedure 84
3.5 Chapter Summary 87
3.6 Chapter References 89
4 Design and Evaluation of Medium and High Power RT-Based WPT Systems 92
4.1 Introduction 92
4.2 Reduced-Scale Experimental Platform and Prototype-Matched Validation 93
4.2.1 Experiment Platform, Operating Conditions and Measurement Method 93
4.2.2 Comparison of Measured and Simulated Terminal Waveforms 98
4.2.3 FFT Based Quantitative Comparison 100
4.2.4 Effect of Core-to-Core Airgap on the Prototype-Matched Model 104
4.3 Intermediate-Scale RT Design and Comparative FEM Assessment 107

4.3.1 Design Basis and Electromagnetic Model 107
4.3.2 Comparison of 2D and 3D FEM Model 112
4.3.3 Sensitivity Analysis and RT Design Parameters 116
4.4 MW-Class Linked Field-Circuit Analysis of the Candidate Rotary Transformers 120
4.4.1 Numerical Model and Common Operating Conditions 120
4.4.2 Comparison of Candidate RT Geometries 124
4.4.3 Effects of Winding Separation and Winding Fill Factor on RT Losses 128
4.4.3.1 Definition of the Parameter Studies 129
4.4.3.2 Effect of Winding Separation 130
4.4.3.3 Effect of Winding Fill Factor 134
4.4.3.4 Design Implications 138
4.4.4 Effect of Winding Turns Ratio on Voltage Transformation 139
4.4.5 Relationship to X-ROTOR Operating Conditions 141
4.5 Chapter Summary 144
4.6 Chapter References 145
5 Conclusions and Future Work 149
5.1 Summary of Research 149
5.2 Answer to Research Questions 150
5.2.1 Research Question 1 150
5.2.2 Research Question 2 151
5.2.3 Research Question 3 152
5.3 Original Contributions and Novelty 153
5.4 Classification of Evidence 154
5.5 Limitations 155

5.6 Future Work 156
5.7 Conclusion 156
Appendix 157
Appendix A MW-Class Linked field circuit model 157
Appendix B Experimental FFT post processing 159

List of Figures

Figure 1.1 X-ROTOR rotor arrangement and qualitative load paths.....4

Figure 2.1 X-ROTOR architecture showing the primary and secondary rotors[1] 30

Figure 2.2 Efficiency curves of the compared two-level and three-level converter arrangements[3][10].....35

Figure 2.3 Electrical power path for one X-ROTOR secondary generator channel 38

Figure 2.4. Reported generator failure modes in offshore wind turbines[17].....41

Figure 2.5 Classification of WPT by field regime and coupling mechanism. 42

Figure 2.6 Inductive WPT system.....44

Figure 2.7 Capacitive WPT system [44].....46

Figure 2.8 Rotating CPT system with a Class-E inverter and Ruthroff balun[46] 47

Figure 3.1 Meridional section of the baseline single-phase radial RT showing the principal magnetic-flux path and local cross-sectional quantities 65

Figure 3.2 Core and winding geometries of the rotary transformers (a) Half hat type (NEW1) (b) Full hat type (NEW2) (c) L-type 1[3] (d) L-type 2 70

Figure 3.3 Half-hat (NEW1) type rotary transformer geometry.....72

Figure 3.4 Full-hat (NEW2) type rotary transformer geometry 74

Figure 3.5 L-type rotary transformer geometries.....76

Figure 3.6 Circuit schematics of single-phase DAB converter interfaced with the RT windings 80

Figure 3.7 Single-phase DAB voltage and current waveforms under SPS control 82

Figure 3.8 Circuit schematics of three-phase DAB converter interfaced with the RT windings 82

Figure 3.9 RT-DAB power transfer stage and principal design variables..... 84

Figure 3.10 RT-DAB design procedure 86

Figure 4.1 Configuration and implementation of the reduced-scale RT-based WPT platform..... 95

Figure 4.2 Reduced-scale RT and magnetic material 96

Figure 4.3 Prototype-matched Maxwell-Simplorer model of the reduced-scale RT-based WPT platform 97

Figure 4.4 Comparison of measured and simulated RT terminal waveforms under the laboratory operating condition (a) Phase shift angle (b) Measured Vp and Vs (c) Measured Ip and Is (d) Simulated Vp and Vs (e) Simulated Ip and Is 99

Figure 4.5 Magnetic characteristic of the M250-35A electrical steel implemented in the FEM model. 107

Figure 4.6 2D and 3D FEM representations of the 600 V/100 kW radial RT ... 111

Figure 4.7 Electrical circuit used for the 2D/3D FEM comparison with a 600 V peak, 2 kHz source and 3.6 Ω secondary load. 111

Figure 4.8 Comparison of voltage, current and load power waveforms obtained from the 2D and 3D FEM models..... 113

Figure 4.9 Instantaneous core loss outputs obtained from the 2D and 3D FEM representations under the retained excitation conditions 114

Figure 4.10 Magnetic flux-density distributions of the 2D and 3D RT models. 115

Figure 4.11 Effects of the investigated RT design variables on $P\mathrm{Cu}$, $P\mathrm{core}$ and $L\sigma$ 119

Figure 4.12 Electrical responses of the candidate RT geometries in the three-phase RT-DAB model: (a) input and output powers, (b) power transfer efficiency,

(c) primary and secondary side RT terminal voltages, (d) transfer inductance current and (e) phase shift command 126

Figure 4.13 Magnetic flux density distributions of the candidate RT geometries 128

Figure 4.14 Simulated three-phase winding loss, $P\mathrm{Cu}$, as a function of phase-shift angle and winding-to-winding separation: (a) Original radial, (b) NEW1, (c) NEW2, (d) L-type 1 and (e) L-type 2 131

Figure 4.15 Simulated three-phase core loss, $P\mathrm{core}$, for different winding separations: (a) Original radial, (b) NEW1, (c) NEW2, (d) L-type 1 and (e) L-type 2. 132

Figure 4.16 Simulated winding loss $P\mathrm{Cu}$ for $kf = 0.60,0.40\ and\ 0.28$ under the fixed winding window condition: (a) original radial type, (b) NEW1, (c) NEW2, (d) L-type 1 and (e) L-type 2. 136

Figure 4.17 Simulated primary and secondary-side RT AC-terminal voltage waveforms of the NEW2 geometry for the $Np: Ns = 24: 24$ and $24: 48$ winding arrangements. 140

List of Table

Table 1.1 Reference operating conditions of the X-ROTOR primary and secondary rotors [22][27][29].....5

Table 1.2 Reported maintenance and component replacement requirements for selected rotating electrical interfaces[21][23][25][29][33].....11

Table 1.3 Reported brush wear for selected slip ring contact pairs[29].....12

Table 1.4 System level design requirements for the proposed RT-DAB interface 17

Table 2.1 Examples of megawatt-scale PMSG voltage and converter arrangements 31

Table 2.2 Voltage classes used in the generator comparison 31

Table 2.3 Comparison of generator side converter topologies.....34

Table 2.4 Comparison of the 690 V and 3.3 kV generator-converter arrangements 36

Table 2.5 Connection options for the two secondary generator channels.....39

Table 2.6 Common compensation arrangements for resonant IPT[36]-[40] 45

Table 2.7 Engineering Comparison of IPT and CPT for the X-ROTOR Interface 48

Table 2.8 Selected High Power Magnetic IPT and Rotary transformer Studies..50

Table 3.1 Qualitative design considerations for the candidate RT geometries 71

Table 3.2 Winding and core cross-sectional areas of the five RT geometries.....71

Table 3.3 Design conditions of the three RT-DAB investigations 79

Table 3.4 lists the RT and DAB quantities used in the Chapter 4 analyses 87

Table 4.1 Operating conditions and measurement boundaries for the reduced-scale experiment and prototype-matched model.....97

Table 4.2 Experimental fundamental phasors and power components from the FFT analysis 101

Table 4.3 Comparison of measured and simulated fundamental RMS quantities 102

Table 4.4 Measured and simulated power factor and AC-terminal transfer metrics 103

Table 4.5 Simulated magnetic parameters of the prototype-matched RT at different core-to-core airgaps 105

Table 4.6 Incremental power transfer quantities for different core-to-core airgaps and phase-shift angles 105

Table 4.7 Principal analytical design parameters and retained FEM conditions of the intermediate scale RT 109

Table 4.8 Quantitative comparison of key outputs obtained from the 2D and 3D FEM models 115

Table 4.9 Definition of the intermediate-scale RT sensitivity study 117

Table 4.10 Operating and model settings of MW-class linked field-circuit simulation 122

Table 4.11 Analytical and geometrical reference parameters of the MW-class RT 123

Table 4.12 Phase-shift sequence and steady-state post-processing intervals 124

Table 4.13 Definition of the MW-class winding-separation and fixed-window fill-factor studies 129

Table 4.14 Mean per-phase coupling factor, electrical loading, DCport powers and RT loss components for the winding-separation study at phase shift angle $= 90\circ$. 133

Table 4.15 Fixed winding window and copper areas used in the fill-factor study 134

Table 4.16 Representative electrical, magnetic and loss quantities for the fixed-window fill factor study at $\text{phase shift angle} = 90°$ 137

Table 4.17 Simulated RT AC-terminal RMS voltage ratios of the selected NEW2 geometry for the investigated turns arrangements 140

Table 4.18 Relationship between the Chapter 4 investigations and the variable operating conditions of the X-ROTOR powertrain..... 142

Table 5.1 Traceability from research questions to methods, results and contributions 153

List of Abbreviations and Symbols

Abbreviations

Abbreviation	Definition
DAB	Dual active bridge
DC	Direct current
FEM	Finite element method
FFT	Fast Fourier transform
HAWT	Horizontal axis wind turbine
IEC	International Electrotechnical Commission
IPT	Inductive power transfer
MMF	Magnetomotive force
NPC	Neutral-point-clamped
PMSG	Permanent magnet synchronous generator
RMS	Root mean square
RT	Rotary transformer
SPS	Single-phase-shift
VAWT	Vertical axis wind turbine
WPT	Wireless power transfer
2D	Two-dimensional
3D	Three-dimensional

Symbols

Latin variables

Symbol	Definition	Unit
A	Rotor swept area	m²
a	Length-to-width aspect ratio of the equivalent rectangular winding window	-
A_c	Effective core cross-sectional area normal to the local principal magnetic flux	m²
A_{Cu}	Effective copper area occupying the winding window	m²
$A_{Cu,design}$	Baseline effective copper occupation used in the MW-class reference design	m²
$A_{g,eff}$	Airgap effective cross-sectional area used in the simplified reluctance model	m²
A_p	Effective overlapping plate area of a capacitive coupler	m²
A_{w}	Total winding window area available to the primary and secondary windings	m²
$A_{\perp,k}$	Cross-sectional area of core section k normal to its local principal flux	m²
a	Length-to-width aspect ratio of the equivalent rectangular winding window	-
a_{Cu}	Equivalent conductor area per turn used in the fixed-window MW-class study	mm²
B_0	Analytical design flux-density target used in the intermediate-scale study	T
B_c	Representative peak core flux density used for initial RT sizing	T
b_{down}	Lower-side winding window width of NEW1	m (or mm)
B_{design}	Analytical design flux density used for MW-class core sizing	T
B_g	Representative peak airgap flux density used for initial RT sizing	T

B_g^*	Selected target airgap flux density for the ampere-turn requirement	T
B_{peak}	Maximum or peak local magnetic flux density obtained from the numerical field solution	T
b_{up}	Upper-side winding window width of NEW1	m (or mm)
b_w	Width of a winding region in the L-type geometry	mm
c	Speed of light in free space	$m \cdot s^{-1}$
C	Effective coupling capacitance	F
C_{dc1}, C_{dc2}	Primary and secondary side DAB DC link capacitances	F
$C_{dc,p}, C_{dc2,s}$	Primary and secondary side DC link filter capacitances in the MW-class linked model	F
C_p	Aerodynamic power coefficient	-
c_p, c_s	Primary and secondary side winding to core clearances	mm
d	Separation between transmitting and receiving structures	m
d_c	Equivalent circular conductor diameter	m (or mm)
e	Relative eccentricity between the rotating and stationary RT carriers	mm
f	Electrical excitation frequency	Hz
f_e	Electrical frequency of the secondary rotor PMSG	Hz
f_{RT}	Electrical excitation frequency used in the intermediate-scale RT model	Hz
f_s	DAB switching or RT excitation frequency used by the stated model	Hz
$f_U(U)$	Wind-speed probability-density function used in the energy-weighted assessment	$(m \cdot s^{-1})^{-1}$
g_0	Nominal RT radial airgap	mm
g_c	Core-to-core magnetic airgap, its numerical value is specific to each investigated platform	mm
$g_{c,down}$	Lower core-to-core magnetic gap of NEW1	mm
$g_{c,up}$	Upper core-to-core magnetic gap of NEW1	mm

g_j	Length of local airgap section j in the segmented magnetic circuit	m
g_{min}	Worst case minimum RT airgap	mm
g_{safe}	Required minimum non-contact safety clearance	mm
h_w	Equivalent winding window length	m (or mm)
I_{base}	Power to-voltage current base used for MW-class analytical sizing	A
$I_{contact}$	Current transmitted through the brush-ring contact	A
I_{line}	Three-phase line current	A
$I_{line,690}$	Line current for the 690 V arrangement	A
$I_{line,3300}$	Line current for the 3300 V arrangement	A
I_{mag}	Equivalent magnetising current producing the principal magnetic flux	A
$I_{p,rms}$, $I_{s,rms}$	Primary and secondary side RMS winding currents	A
$I_{p/s,3\varphi,rms}$	Primary- and secondary-side three-phase RMS currents reported in the MW-class study	A
I_{rms}	RMS winding current used in current-density and loss relationships	A
$I_{w,rms,calc}$	Analytical winding current used for initial intermediate-scale sizing	A
$iL(t)$	Instantaneous current through the effective DAB transfer inductance path	A
J	RMS conductor current density	A·mm^{-2}
J_p, J_s	Allowable primary and secondary side winding current densities	A·mm^{-2}
k	Magnetic coupling coefficient	-
k_1	Ratio of the upper to lower NEW1 core-to-core magnetic gaps	-
k_2	Ratio of core-to-core magnetic airgap to winding separation for NEW2	-
k_f	Winding fill factor: fraction of window area occupied by effective conductor	-
$k_{f,design}$	Baseline winding fill factor used in the MW-class analytical design	-

$k_{ps,ph}$	Mean per-phase primary-to-secondary magnetic coupling coefficient	-
k_v	Voltage-waveform coefficient in the Faraday-law sizing relationship	-
L_b	Effective separation between the principal bearing reaction planes	m
L_{eq}	Total effective DAB transfer inductance referred to the selected RT side	H
$L_{eq,ph}$	Primary-referred effective DAB transfer inductance per phase	H
L_{ext}	Deliberately introduced external series inductance referred to the selected side	H
L_i	Self-inductance of winding i	H
L_p	Primary winding self-inductance	H
L_s	Secondary winding self-inductance	H
$L_{\sigma,ph}$	Per-phase leakage inductance used in the MW-class linked model	H
$L_{c,k}$	Local magnetic core-path length of section k	m
l_{mean}	Mean conductor length per turn	m
$l_{mean,NEW1}$	First-order mean conductor length per turn for NEW1	m
M	Mutual inductance between the coupled windings	H
M_{res}	Residual overturning moment reacted by the bearing/support system	N·m
N	Number of turns in the winding considered	-
N_P, N_s	Primary and secondary side RT winding turns	-
$n_{s,nom}$	Nominal secondary generator mechanical speed	r/min
n_t	RT turns ratio, Np/Ns	-
p	Number of generator pole pairs	-
P	Active electrical power	W
P_{3ph}	Ideal transferred power of the three-phase DAB within the stated SPS interval	W

P_{aero}	Aerodynamic power	W
$P_{contact}$	Electrical loss at the brush-ring contact	W
P_{core}	Magnetic-core loss associated with the implemented material-loss model	W
P_{cu}	Winding copper-loss contribution under the stated conductor model	W
P_{DAB}	Ideal average transferred power of the single-phase DAB	W
$P_{dc}(U)$	Mean input power presented to an RT-DAB channel at wind speed U	W
PF	Power factor	-
$PF_{1,p}, PF_{1,s}$	Primary and secondary side fundamental power factors	-
$PF_{\Delta,p}, PF_{\Delta,s}$	Baseline-referenced incremental primary and secondary side power factors	-
P_{in}	Cycle-averaged input power at the stated model boundary	W
P_{nom}	Nominal transferred-power requirement of the MW-class design	W
P_{out}	Cycle-averaged output power at the stated model boundary	W
$P_{p,1}, P_{s,1}$	Primary and secondary side fundamental active-power components	W
P_{req}	Required transferred power specified at the applicable design boundary	W
P_{trans}	Transferred active power used for preliminary RT current sizing	W
Q_i	Unloaded quality factor of winding i	-
$Q_{p,1}, Q_{s,1}$	Primary- and secondary-side fundamental reactive-power components	var
R	Primary rotor radius	m
R_1	Reference inner radius used to determine the mean annular winding radius	m (or mm)
$R_{contact}$	Effective brush-ring contact resistance	Ω
R_i	Effective AC resistance of winding i	Ω

R_{cu}	Winding DC resistance used in the first-order copper-loss relation	Ω
R_{Cu}	Winding DC resistance used in the first-order copper-loss relation	Ω
R_{ext}	Assigned series resistance of the external transfer-inductance branch	Ω
R_L	Secondary load resistance in the intermediate-scale RT model	Ω
R_m	Mean RT airgap radius	mm
R_{sh}	Reference shaft radius used in the annular core-width relationship	m (or mm)
R_m	Mean RT airgap radius	mm
R_{sh}	Reference shaft radius used in the annular core-width relationship	m (or mm)
$\mathcal{R}_g$	Approximate combined airgap reluctance	H^{-1}
$\mathcal{R}_{tot}$	Total reluctance of the segmented magnetic circuit	H^{-1}
r_v	Simulated RT RMS voltage ratio, defined as secondary-side RMS voltage divided by primary-side RMS voltage	-
r, z	Radial and axial coordinates of the meridional RT cross-section	m (or mm)
S_w	Effective conductor cross-sectional area	m^2
T	Aerodynamic torque	N·m
T_s	DAB switching period	s
$\overline{T}$	Mean aerodynamic torque	N·m
$\widetilde{T}$	Cyclic component of aerodynamic torque	N·m
t_φ	Time displacement corresponding to the DAB phase-shift angle	s
U	Wind speed used as the integration variable in the wind-energy-weighted assessment	$m \cdot s^{-1}$
U_{ci}	Turbine cut-in wind speed	$m \cdot s^{-1}$
U_{co}	Turbine cut-out wind speed	$m \cdot s^{-1}$

V_{dc1}, V_{dc2}	Primary and secondary side DAB DC link voltages	V
$V_{dc,p}, V_{dc,s}$	Primary- and secondary-side DC link voltages in the MW-class linked model	V
V_{eff}	Effective inflow velocity at a secondary rotor	m·s^{-1}
$V_{f,D}$	Diode forward-voltage parameter used in the linked circuit model	V
$V_{f,IGBT}$	IGBT forward-voltage parameter used in the linked circuit model	V
V_{orb}	Orbital velocity of a secondary rotor hub	m·s^{-1}
V_{∞}	Ambient free stream wind speed	m·s^{-1}
$v_{p,ph(t)}, v_{sph(t)}$	Instantaneous primary and primary-referred secondary bridge voltages of one phase	V
$v_{p(t)}, v_{s(t)}$	Instantaneous primary and secondary side bridge output voltages	V
$V_{p,1,rms}, V_{s,1,rms}$	Primary- and secondary-side fundamental RMS RT terminal voltages	V
V_p, V_s	Primary and secondary side RMS RT winding-terminal voltages	V
$V_{p,rms,req}$	Required primary RMS voltage for the intermediate analytical design	V
$Vrms$	RMS voltage of the winding considered	V
$v'_{s(t)}$	Secondary bridge output voltage referred to the primary side	V
w_c	Local core width used in the topology-specific geometrical relationships	m (or mm)

Greek Variable

Symbol	Definition	Unit
α	Relative angular tilt between the rotating and stationary RT carriers	rad
β	Aspect ratio between NEW2 winding window length and width	-
γ	Aspect ratio between NEW1 winding window length and lower-side width	-
δ_w	Primary-to-secondary winding separation, distinct from the core-to-core magnetic airgap	mm
ΔF	Difference between the bearing reaction forces forming the resisting couple	N
Δg_{wc}	Worst-case accumulated reduction in RT airgap	mm
ΔP_x	Baseline-referenced change in active power at terminal x	W
ΔQ_x	Baseline-referenced change in reactive power at terminal x	var
ε	Effective permittivity of the capacitive coupling region	$F \cdot m^{-1}$
ε_v	Deviation of the simulated RMS voltage ratio from the ideal turns-ratio value	%
η	Electrical conversion efficiency	-
$\eta_{E,RT-DAB}$	Wind-energy-weighted RT-DAB transfer efficiency	-
$\eta_{\Delta,AC}$	Baseline-referenced incremental AC-terminal transfer metric	-
θ	Primary rotor azimuthal position	rad
λ	Primary rotor tip speed ratio	-
λ_{em}	Electromagnetic wavelength	m
μ_0	Permeability of free space	$H \cdot m^{-1}$
$\mu_{r,k}$	Relative permeability of local magnetic core section k	-
ρ	Air density	$kg \cdot m^{-3}$
ρ_c	Electrical resistivity of the winding conductor	$\Omega \cdot m$

φ	DAB inter-bridge phase-shift angle	rad
Φ	Principal linked magnetic flux	Wb
Φ_{max}	Peak linked magnetic flux	Wb
ω	Electrical excitation angular frequency	rad·s^{-1}
Ω	Primary rotor angular speed	rad·s^{-1}

Chapter 1

1 Introduction

1.1 Research Background

Anthropogenic greenhouse-gas emissions associated with fossil-fuel use are the principal driver of observed global warming and its associated risks, including sea-level rise and loss of land ice[1]. Reducing emissions from electricity generation is therefore necessary to meet long-term decarbonisation targets. In the United Kingdom, the statutory emissions target is amended in 2019 to require net-zero greenhouse-gas emissions by 2050[2]. Offshore wind forms part of this transition because it allows large generating capacities to be installed in areas with favourable wind resources[4] .

Wind turbines convert the kinetic energy of moving air into mechanical power and subsequently into electrical power through a generator. They are commonly classified by rotor-axis orientation as horizontal-axis wind turbine (HAWT) or vertical-axis wind turbine (VAWT)[3]. HAWTs dominate present utility-scale deployment, whereas VAWTs differ in their aerodynamic behaviour, structural arrangement and drivetrain configuration. A VAWT can accept wind from different directions without an active yaw mechanism. This advantage does not, however, remove the drivetrain and cyclic-loading constraints that affected earlier large-scale VAWT developments[3][4].

During the 1980s, Flowind Inc. deployed more than 500 Darrieus turbines in Californian wind farms, while a subsidiary of Sir Robert McAlpine and Sons developed H-rotor prototypes rated up to 500 kW and tested them at Carmarthen Bay. These programmes demonstrated that large VAWTs could be constructed and operated in practice. They also exposed important engineering limitations, particularly the high

torque transmitted through a low-speed main shaft and the associated drivetrain mass, structural loading and cost relative to contemporary HAWTs[4].

For a conventional VAWT, the relative flow velocity and blade angle of attack vary with rotor azimuth. The aerodynamic torque therefore contains mean and cyclic components and may be represented as follows:

$$T(\theta) = \bar{T} + \tilde{T}(\theta) \tag{1.1}$$

where $\bar{T}$ is the mean torque and $\tilde{T}(\theta)$ is the cyclic torque component. The aerodynamic power is

$$P_{aero} = \frac{1}{2}\rho A V_{\infty}^{3} C_p \tag{1.2}$$

The tip speed ratio is defined as:

$$\lambda = \frac{\Omega R}{V_{\infty}} \tag{1.3}$$

For a given mean mechanical power

$$\bar{T} = \frac{\overline{P_{areo}}}{\Omega} = \frac{1}{2}\rho A V_{\infty}^{2} \frac{C_p}{\lambda} \tag{1.4}$$

where P_{aero} is the aerodynamic power, ρ is the air density, A is the swept area, V_{∞} is the free stream wind speed. R is the rotor radius, and Ω is the rotor angular speed. Equation (1.4) shows that the drivetrain torque increases as rotational speed decreases for a given mechanical power. A large VAWT operating at relatively low rotational speed therefore imposes a high mean torque on the shaft, bearings and supporting structure, while the cyclic torque component introduces repeated stress variation and associated fatigue loading.

The main difficulty in scaling a conventional VAWT is not aerodynamic energy capture alone. The low rotational speed requires high drivetrain torque for a given mechanical power, while the cyclic torque component introduces repeated mechanical loading. A large-scale design should therefore reduce the concentration of these loads in a single low-speed drivetrain and provide a different route for electromechanical conversion.

The V-rotor concept addresses part of this problem by distributing aerodynamic loading above and below a relatively short central support. Depending on the magnitude and position of the upper and lower aerodynamic forces, their bending-moment

contributions can partially oppose one another. The X-ROTOR extends this arrangement by separating the low-speed primary aerodynamic rotor from the higher-speed secondary generator units[4][22][27].

This arrangement introduces a separate electrical design requirement. The secondary generators and their associated power electronic converters rotate with the primary structure, whereas the downstream electrical system is stationary. Their electrical output must therefore cross the continuously rotating rotor-to-tower boundary. This requirement provides the direct motivation for the contactless power transfer interface investigated in this thesis.

Wireless power transfer (WPT) has been investigated in applications including electric-vehicle charging, marine systems, industrial equipment and rotating electrical interfaces[8]-[12][15][16][23] [26]. Relevant studies have considered reactive power minimisation[14][17], offshore charging[15], adaptive tuning under dynamic coupling [18] and combined power and information transfer[20]. Although these applications differ in rating, geometry and operating conditions, they identify magnetic coupling, alignment, reactive-power control and converter coordination as recurring design considerations for contactless electrical interfaces.

The system investigated in this thesis combines an inductive rotary transformer (RT) with a dual active bridge (DAB) converter. The RT provides magnetic coupling across the rotating interface, while the DAB generates the medium frequency excitation and controls transferred power through phase-shift modulation. The RT and DAB are therefore considered together because the magnetic characteristics of the transformer influence the converter current and voltage behaviour, while the converter operating conditions determine the excitation applied to the transformer[11][12][19][24][26].

This establishes the research chain developed in the remainder of the chapter: Section 1.2 defines the X-ROTOR operating and structural context, Section 1.3 evaluates the maintenance and reliability implications of a conventional sliding interface, and Section 1.4 converts those findings into the system requirements, research questions and objectives for the proposed RT-DAB interface.

1.2 X-ROTOR Concept

The X-ROTOR is a hybrid offshore wind-turbine architecture derived from the V-rotor vertical-axis wind-turbine concept [4]. As illustrated in Figure 1.1, the primary rotor comprises upper and lower blade sections connected through a relatively short central crossarm, while two smaller horizontal-axis secondary rotors are mounted on the lower rotating arms. The primary and secondary rotors perform different functions. The primary rotor provides the main aerodynamic torque, while the secondary rotors provide the electrical power take-off.[4]

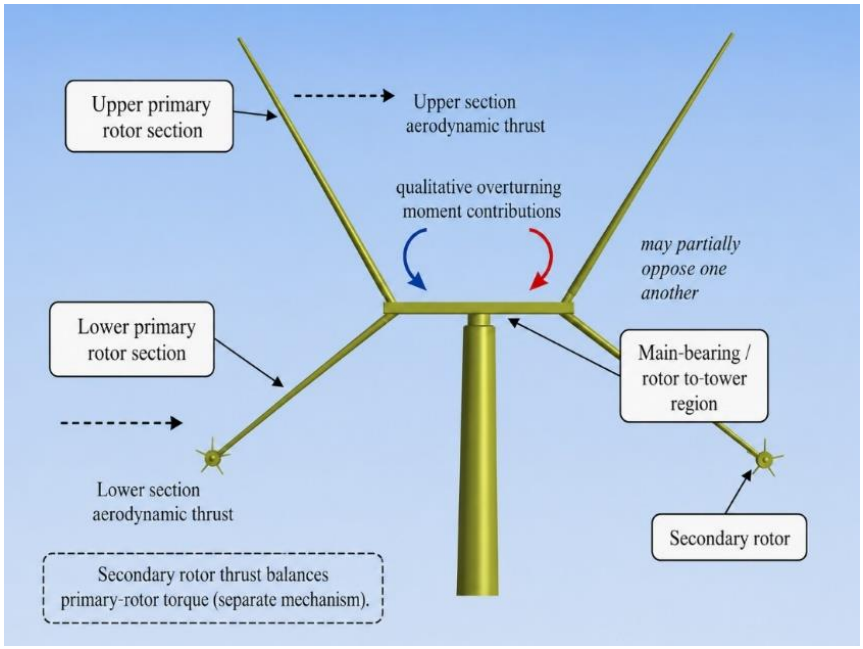


Figure 1.1 X-ROTOR rotor arrangement and qualitative load paths

1.2.1 Operating Roles and Reference Conditions

The primary rotor is the large, low-speed aerodynamic component of the X-ROTOR. It develops the aerodynamic torque that drives the rotating primary structure but is not connected directly to a central electrical generator. The project design basis places the primary rotor at approximately 8 r/min under rated conditions[27].

Electrical conversion is performed by two secondary rotor generator units mounted on the lower part of the rotating structure. Each secondary rotor drives a permanent

magnet synchronous generator (PMSG) with a project reference rating of 2.5 MW. For four pole pairs and an electrical frequency of approximately 25 Hz, the corresponding nominal mechanical speed is

$$n_{g,nom} = \frac{60 f_e}{p} = \frac{60 \times 25}{4} = \frac{375\, r}{min} \tag{1.5}$$

where $n_{g,nom}$ is the nominal generator mechanical speed, f_e is the generator electrical frequency and p is the number of pole pairs. Equation (1.5) gives approximately 375 r/min. The optimised PMSG design reported in the project documentation gives a closely corresponding rated speed of approximately 372 r/min[27][29]. The two values therefore refer to the frequency-derived operating point and the detailed machine-design point, respectively.

The secondary rotors are exposed to a relative inflow formed by the ambient wind velocity and their orbital motion about the primary rotor axis. Neglecting local induction and flow-distortion effects, this relation may be written in vector form as

$$V_{eff,i}(\theta) = V_\infty - V_{orb,i}(\theta) \tag{1.6}$$

where$V_{eff,i}$ is the effective inflow-velocity vector, V_∞ is the ambient wind-velocity vector and $V_{orb,i}$ is the orbital-velocity vector of the corresponding secondary rotor hub. The X-ROTOR project design gives a primary rotor tip speed of approximately 60 m/s under the reference operating condition[27]. The rotational motion of the secondary rotor hubs contributes to their local effective inflow. Because the magnitude and direction of the effective inflow vary with primary rotor azimuth, the two secondary rotors may experience different instantaneous aerodynamic torques, rotational speeds and generator operating points[22][27][29].

Table 1.1 Reference operating conditions of the X-ROTOR primary and secondary rotors [22][27][29]

Parameter	Primary rotor	Each secondary rotor
Principal function	Aerodynamic energy capture and production of primary rotor torque	Aerodynamic thrust production and electrical power generation
Direct electrical generator	None	One PMSG per secondary rotor

Electrical generator rating	No separate electrical generator rating	2.5 MW per generator, 5 MW combined installed rating
Nominal rotational speed	Approximately 8 r/min at rated conditions	Approximately 375 r/min nominal, approximately 372 r/min for the optimized PMSG design
Electrical frequency	Not applicable	Approximately 25 Hz
Pole pairs	Not applicable	Four
Inflow condition	Ambient wind acting on the primary VAWT structure	Effective inflow produced by the vector combination of ambient wind and secondary hub orbital motion
Operating variation	Depends on turbine operating condition	Effective inflow, torque and speed vary with primary rotor azimuth

These project-level operating conditions are distinct from the staged WPT subsystem ratings examined in this thesis. The 600 V/100 kW single-phase RT is used as an intermediate electromagnetic design case for analytical and 2D/3D finite element method (FEM) comparison. The subsequent 1.8 kV/1 MW three-phase RT-DAB model represents a MW-class electrical transfer stage used for candidate-geometry, phase-shift, parameter-sensitivity and voltage-transformation studies. Neither case represents the combined output of the two 2.5 MW secondary generators.

The secondary generator speed must also be distinguished from the relative mechanical speed across the RT. The RT is located at the primary rotor-to-tower interface and therefore rotates relative to the stationary side at approximately the primary rotor speed. Transfer of the complete turbine output would require further converter, protection and thermal design beyond the subsystem investigated here.

1.2.2 Overturning Moment and Primary Rotor Torque Balance

A conventional large VAWT can impose a substantial overturning moment on its main support because the aerodynamic force resultants act over the height of the rotor. In the X-ROTOR, the upper and lower parts of the primary structure provide separate

aerodynamic load paths. The corresponding moment about the central support may be represented qualitatively as

$$M_{ov} = r_U \times F_U + r_L \times F_L \tag{1.7}$$

where r_U and r_L are the position vectors from the reference support to the upper- and lower-section aerodynamic resultants F_U and F_L respectively. Depending on the directions and moment arms of these resultants, their signed bending-moment contributions can partially oppose one another. The resulting reduction depends on rotor geometry, force magnitude, centre-of-pressure position, azimuth and operating condition. Exact cancellation is not assumed because separate numerical upper- and lower-section load resultants and moment arms are not available for this assessment.

This bending-moment redistribution is separate from torque balance about the primary vertical axis. The aerodynamic torque acting on the primary rotor is balanced through the thrust developed by the secondary rotors, whose associated PMSGs perform the electrical power conversion. Residual bending moments and cyclic loads are reacted through the bearing and supporting structure, as discussed further in Section 1.4.2.

1.2.3 Projected Performance and Cost

The X-ROTOR is proposed to reduce dependence on a large central drivetrain operating at low rotational speed and to improve the structural and maintenance characteristics of large offshore wind turbines. Project studies report potential reductions of up to 26% in levelized cost of energy and up to 55% in operation and maintenance expenditure relative to the selected reference concept[5][6]. These values are project-level projections rather than results established independently in this thesis. Their realisation depends on the aerodynamic design, structural mass, secondary generator system, electrical architecture, offshore installation strategy and long-term reliability of the rotating interface.

The present work addresses the contactless RT-DAB interface within this wider system. It is examined through analytical modelling, a reduced-scale laboratory platform, an intermediate 600 V/100 kW electromagnetic study and a separate 1.8 kV/1

MW linked field-circuit model. The roles and evidence limits of these investigation levels are defined in Section 1.4.3.

1.2.4 Implication For Electrical Power Transfer

Locating the two generator channels and their machine side converters on the rotating primary structure requires the generated power to cross a continuously rotating rotor-to-tower interface. A conductive slip ring could provide this connection, but its suitability depends on more than voltage and current rating. Contact wear, surface condition, environmental exposure, inspection, replacement access and long-term reliability are also relevant.

These considerations make the rotating electrical interface a distinct design problem within the X-ROTOR powertrain. The operating and maintenance characteristics of sliding electrical interfaces are considered next before the requirements for the contactless alternative are defined.

1.3 Rotating Electrical Interface and Slip Ring Maintenance

1.3.1 Sliding Contact Degradation Mechanisms

Brushed slip rings are mature components used to transmit electrical power and signals across rotary joints. The sliding contact is, however, subject to wear and contamination and requires maintenance, which is a concern for a continuously rotating, high power offshore interface.

Friction between the brushes and rings causes gradual material loss. Wear debris can increase the risk of conductive contamination, short circuits, localised heating and unstable contact. Brush misalignment and unsuitable contact geometry may also produce chatter, intermittent contact and electrical arcing[7][30].

A stable surface film is important to both the electrical and tribological behaviour of the contact. Its formation depends on the brush and ring materials, contact pressure, humidity, contamination, current density and temperature. An unstable or non-uniform film can increase brush and ring wear and cause variation in the contact voltage [30][35].

Electrical loading also affects degradation through local contact heating. Higher current and increased effective contact resistance increase the electrical loss at the interface. Run-out, uneven brush pressure, oxide formation, debris and temperature can cause the effective contact resistance to vary during operation[21][30][31][32][35]. These effects increase inspection and component replacement requirements, particularly in offshore operation where access is weather-dependent and unplanned maintenance can reduce system availability.

1.3.2 Comparable Rotary Electrical Interfaces

The need to transfer electrical power across a rotating boundary is not unique to wind turbines. Rotary transformers have been developed for brushless excitation of electrically excited synchronous machines[23]. Other manufactured and tested RT systems have also demonstrated contactless power transfer across rotating magnetic interfaces[24], while alternative RT topologies have been investigated to increase transferred-power capability[26].

Capacitive power transfer has also been investigated as a replacement for conventional brush and slip ring excitation in wound-field synchronous machines[25]. In this arrangement, electrical power is transferred through a rotating capacitive interface rather than through sliding contacts. These examples show that non-contact transfer across a rotating boundary has been considered in several classes of electrical machine, although the power rating, geometry, speed and operating environment differ from those of the X-ROTOR.

A relevant high power conductive comparison is a marine-certified industrial slip ring system rated at approximately 2.5 MW, 3.3 kV and 20 r/min[29]. Its rating is comparable with the electrical and low-speed operating regime considered for the X-ROTOR interface, although its mechanical arrangement, environmental conditions and

duty cycle are not identical. It is therefore used here as an engineering reference for a high power rotating electrical interface rather than as a direct prediction of X-ROTOR performance or service life.

1.3.3 Slip Ring Operation at Low Speed and High Electrical Loading

Low rotational speed does not eliminate sliding contact degradation. A lower surface speed may reduce the frictional loss associated directly with sliding motion, but contact resistance, current-dependent heating, brush-force variation and surface-film stability remain relevant to the electrical and mechanical condition of the interface.

The electrical loss at the brush-ring interface could be expressed as

$$P_{contact} = I^2 R_{contact} \tag{1.8}$$

where I is the transmitted current and R_{contact} is the effective resistance of the brush-ring interface. At high current, even a relatively small increase in contact resistance can produce appreciable local heating. The effective resistance is not constant in practice and can be affected by brush pressure, surface-film condition, contamination, wear debris, temperature and local contact geometry [21][30]-[32][35].

Mechanical run-out and eccentricity can also produce non-uniform brush pressure around the ring. The suitability of a slip ring for the X-ROTOR application therefore cannot be determined from rotational speed or nominal current rating alone. Contact material, current density, brush pressure, contact resistance, surface condition, cooling, contamination and maintenance accessibility must also be considered.

For the X-ROTOR, the relevant operating condition combines low rotational speed with substantial continuous electrical loading. Quantitative values of sliding velocity, contact pressure, interface temperature and wear rate depend on the final ring radius, brush geometry, contact material, loading and thermal boundary conditions. These parameters are not defined in sufficient detail in the present work to support a full slip ring lifetime calculation. The discussion is therefore used to identify the operating and maintenance requirements of the rotating electrical interface rather than to predict a specific brush life.

1.3.4 Maintenance and Component Replacement Requirements

Reported maintenance intervals for slip rings vary with contact material, current density, rotational speed, environment and duty cycle. The values summarised in Table 1.2 therefore represent specific technologies and operating conditions rather than universal service intervals. For marine-certified industrial slip ring example introduced in Section 1.3.2, the cited project and manufacturer information recommends removal and servicing after approximately five years, with brush replacement during the service[29][33]. This value is used as an application-specific comparison and is not adopted as the expected service interval of the X-ROTOR interface.

Table 1.2 Reported maintenance and component replacement requirements for selected rotating electrical interfaces[21][23][25][29][33]

Interface	Operating context	Inspection/service requirement	Component replacement requirement
Copper-graphite slip ring	Contacting rotary interface	Reported service interval approximately 0.25 year	Reported brush life/replacement interval approximately 5 years
Graphite-graphite slip ring	Contacting rotary interface	Reported service interval approximately 1 year	Reported brush life/replacement interval approximately 5 years
Marine certified industrial slip ring	Approximately 2.5 MW, 3.3 kV and 20 r/min	Removal and servicing recommended after approximately 5 years	Brushes replaced during the proposed service
Rotary transformer excitation interface	Brushless excitation of an electrically excited synchronous machine	Inspection of insulation, temperature, alignment and bearing condition remains necessary	No routine brush replacement
Capacitive rotating interface	Contactless excitation of a wound-field synchronous machine	Inspection of insulation and coupler condition remains necessary	No routine brush replacement
Proposed X-ROTOR rotary transformer interface	Continuous high power rotor-to-tower transfer	Inspection of insulation, temperature, airgap,	No routine brush replacement, other replacement intervals are not yet established

		alignment, sealing, vibration and supporting bearings	

The project comparison also reports the brush-wear values reproduced in Table 1.3. These values provide additional context for the effect of contact-pair selection on maintenance demand.

Table 1.3 Reported brush wear for selected slip ring contact pairs[29]

Friction Pair	Reported brush wear per 1000 hours
Copper-graphite	4 - 7 mm
Graphite-graphite	< 0.5 mm

The reported wear rates differ markedly between the two contact pairs, but they cannot be transferred directly to the X-ROTOR. Brush wear depends on current density, brush pressure, rotational speed, ring geometry, surface condition, temperature and operating environment. The values in Table 1.2 and Table 1.3 are therefore used to define the maintenance context of the rotating electrical interface rather than to predict a specific X-ROTOR brush life.

Removing the sliding electrical contact eliminates routine brush inspection and replacement, but it does not remove the need for maintenance. A contactless RT interface still requires monitoring and inspection of insulation condition, winding and core temperature, airgap stability, alignment, sealing, moisture ingress, vibration, eccentricity and supporting-bearing condition[6][21][31][34]. These requirements are carried forward to the system-level design constraints defined in Section 1.4

1.3.5 Requirements for the X-ROTOR Power Transfer Interface

An adequately rated slip ring can provide a conductive path across the rotating interface, but it retains the wear, conductive debris, contact-resistance variation, inspection and brush-replacement requirements discussed in the preceding sections.

These characteristics are undesirable for a continuously rotating offshore system in which access is limited and maintenance can reduce availability.

A rotary transformer removes the sliding electrical contact and its associated brush-wear mechanism. It therefore avoids routine brush inspection and replacement, but introduces different requirements associated with insulation, winding and core temperature, airgap stability, alignment, sealing, vibration and supporting-bearing condition. The contactless interface must consequently be assessed as an electromagnetic, electrical and mechanical system rather than as a direct maintenance-free replacement for the slip ring.

For the X-ROTOR, the resulting design problem is to transfer electrical power across the rotor-to-tower boundary while maintaining the required airgap and electrical performance under the expected mechanical and environmental conditions. These requirements provide the basis for the system constraints developed in Section 1.4 and for the comparison of contactless power transfer approaches in Chapter 2.

1.4 Research Challenges, System Requirement and Objectives

The X-ROTOR architecture places the secondary generator units and their associated power electronic conversion on the rotating primary structure. Electrical power must therefore cross the rotor-to-tower boundary before reaching the stationary electrical system. As discussed in Section 1.3, a conductive slip ring could provide this connection, but it would retain sliding contact wear, inspection and component-replacement requirements.

The rotating electrical interface must satisfy electrical, electromagnetic, power electronic, mechanical, thermal and maintenance requirements at the same time. The RT, DAB converter and phase-shift control are therefore treated as a coupled design problem[19][24][26][28][29]. The following sections define the physical interface, the mechanical load path and the principal system requirements used in the subsequent analytical and numerical studies.

1.4.1 RT Location and Preliminary Installation Envelope

The RT is located at the primary rotor-to-tower boundary as a concentric, non-contact electrical interface. The inner magnetic core and winding are carried by the rotating primary structure, while the outer magnetic core and winding are supported from the stationary tower side. The two magnetic halves rotate relative to one another across a controlled radial airgap. The RT transfers electrical power across this boundary but is not intended to act as a main structural bearing or to transmit the primary rotor aerodynamic loads[28][29].

The preliminary interface geometry gives an outer radius of approximately 1.220 m for the inner rotating cylinder and an inner radius of approximately 5.470 m for the outer stationary cylinder. The corresponding gross radial installation envelope is

$$\Delta R_{gross} = 5.470 - 1.220 = 4.250\, m \tag{1.9}$$

Equation (1.9) gives approximately 4.250 m at the rotor-to-tower interface. This dimension defines the gross radial region within which the magnetic cores, windings, mechanical carriers, insulation, cooling provisions and installation clearances must be accommodated. It is distinct from the much smaller electromagnetic core-to-core airgap used in the RT design.

The preliminary envelope does not preclude the proposed RT arrangement, but it does not constitute a complete mechanical packaging verification. Detailed integration requires the analytical and FEM dimensions developed in Chapters 3 and 4 to be incorporated into an integrated CAD and tolerance model including the bearing housing, RT carriers, flanges, insulation, cooling passages, sealing, cabling and assembly clearances.

1.4.2 Structural Load Path and RT Airgap Protection

The bearing arrangement reacts the residual aerodynamic loads rather than eliminating the overturning moment. The upper and lower rotor load distribution reduces the net moment transmitted to the central support, while any remaining moment is reacted by a force couple at separated bearing-reaction planes and transferred to the stationary tower[27][28][29].

In a first-order static representation, the difference between the bearing reaction forces is of the order

$$\Delta F \approx \frac{M_{res}}{L_b} \tag{1.10}$$

where M_{res} is the residual overturning moment and L_b is the effective separation between the bearing-reaction planes. This relation defines the principal load path but does not determine the corresponding structural displacement. Translation and angular tilt also depend on shaft and support stiffness, bearing clearance or preload, internal bearing-load distribution and housing flexibility.

The structural load path proceeds from the rotor and hub through the shaft and supporting structure, then through the separated bearing-reaction planes and into the stationary tower. The RT is not part of this primary load path. The rotating RT half is mounted on a local carrier referenced to the rotating structure, while the stationary half is mounted on a tower-side carrier. Neither magnetic half is intended to carry the primary rotorthrust or overturning moment.

The bearing and support system must therefore maintain the relative concentricity and angular alignment of the two RT carriers. A conservative worst-case airgap-deviation budget is defined as

$$\begin{aligned}\Delta g_{\mathrm{wc}} = |e| + R_m|\alpha| + |\Delta g_{\mathrm{man}}| + |\Delta g_{\mathrm{ass}}| + |\Delta g_{\mathrm{bear}}| + |\Delta g_{\mathrm{struct}}| + |\Delta g_{\mathrm{run}}| \\ +|\Delta g_{\mathrm{thermal}}| + |\Delta g_{\mathrm{vib}}|\end{aligned} \tag{1.11}$$

where e is the relative radial eccentricity, R_m is the reference radius at which the angular displacement is evaluated, α is the relative angular tilt, and the remaining terms represent manufacturing and assembly error, bearing displacement, structural deflection,

run-out, thermal growth and vibration-induced variation. The corresponding minimum local airgap is

$$g_{min} = g_0 - \Delta g_{\mathrm{wc}} \tag{1.12}$$

and the non-contact condition is

$$g_{min} \geq g_{safe} > 0 \tag{1.13}$$

Equations (1.11) - (1.13) provide a conservative geometric tolerance framework for the rotor-to-tower interface[37][38]. They define the minimum-clearance requirement to be satisfied during subsequent mechanical integration and are not presented as results from a completed full-scale structural or bearing model.

A separate project-level electromagnetic sensitivity study considers a nominal airgap of 10 mm with an imposed static eccentricity of 2 mm, producing local airgaps of 8 and 12 mm[29]. The reported electrical response changes only moderately for this offset, although the magnetic-force magnitude increases. These results indicate the electromagnetic sensitivity of the investigated RT design to static eccentricity. They do not constitute validation of bearing stiffness, structural deflection, thermal expansion or dynamic vibration of the complete X-ROTOR interface.

Airgap variation also affects magnetic coupling, magnetising and leakage inductance and converter current[24][26]. The non-contact condition therefore requires the calculated and measured minimum airgap to satisfy Equation (1.13) over the applicable design-load envelope. The corresponding mechanical limits must ultimately be checked against the electromagnetic airgap requirements developed in Chapters 3 and 4.

1.4.3 System Level Design Requirements

The principal requirements of the proposed RT-DAB interface are summarised in Table 1.4. They arise from the X-ROTOR operating conditions, the rotor-to-tower installation boundary described in Sections 1.4.1 and 1.4.2, and the electrical and electromagnetic studies developed later in the thesis.

Three investigation levels are used. The reduced-scale laboratory platform examines phase-shift-controlled transfer and provides measured RT-terminal quantities

under its own operating conditions. The 600 V/100 kW case is used to assess the analytical and electromagnetic modelling procedure, while the 1.8 kV/1 MW linked field-circuit model is used to investigate MW-class electrical behaviour. These three cases serve different purposes, the laboratory platform is not a geometrically, electrically or thermally scaled prototype of either high power design.

Table 1.4 therefore distinguishes the design requirement, the basis used in this thesis, the evidence developed for that requirement and the work that remains necessary for complete turbine-level implementation.

Table 1.4 System level design requirements for the proposed RT-DAB interface

Requirement	Design requirement	Evidence in this thesis	Further verification
Installation envelope	Accommodate the RT within the rotor-to-tower region without interfering with the main structural load path	Preliminary 1.220-5.470 m radial envelope together with analytical and FEM RT dimensions	Integrated CAD, tolerance, installation and removal analysis
Mass and physical integration	Limit active and structural mass within the available installation region	Candidate magnetic structures are compared under defined geometrical conditions	Carrier, housing, cooling and structural mass calculation
Power rating	Provide MW-class rotor-to-tower power transfer	600 V/100 kW electromagnetic case and 1.8 kV/1 MW linked field-circuit case	Full generator-output aggregation, redundancy and fault isolation
Voltage and isolation	Provide galvanic isolation and the required voltage relationship	1.8 kV design basis and investigated 1:1 and 1:2 winding arrangements	Insulation coordination and final generator/converter integration
Power factor and con-verter load-ing	Limit unnecessary reactive current and converter kVA	FFT-based active/reactive-power and power factor analysis	Assessment over the complete turbine operating range
Losses and efficiency	Limit RT and converter losses at the specified operating point	AC-terminal experimental quantities, FEM losses and linked field-circuit powers	Full electrothermal assessment including converter and cooling losses

Mechanical loading	Keep primary structural loads out of the RT magnetic structure	Structural load path and bearing reaction model in Section 1.4.2	Coupled structural analysis under normal, cyclic and extreme loads
Airgap and alignment	Maintain positive clearance and acceptable electromagnetic behaviour	Airgap tolerance equations and numerical gap-sensitivity studies	Combined eccentricity, tilt, bearing displacement, thermal and vibration assessment
Thermal management	Keep windings, core, semiconductor devices and insulation within allowable temperatures	Calculated winding/core losses and reduced-scale observations	Cooling-system design and full-duty electrothermal testing
Offshore environment and maintenance	Remove routine brush maintenance while retaining inspect ability	Slip ring comparison and RT maintenance requirements in Section 1.3	Long-term sealing, corrosion, insulation, bearing and vibration assessment
Protection and availability	Limit fault propagation and maintain channel availability	Electrical system architecture and modular channel requirements	Protection coordination, fault isolation, monitoring and redundancy design

1.4.4 Research Questions

Based on the X-ROTOR operating conditions, the limitations of sliding contact power transfer and the system level requirements established above, this thesis addresses the following research questions:

1. To what extent can an integrated RT-DAB interface support high power contactless power transfer across the mechanically constrained rotor-to-tower boundary of the X-ROTOR?

2. How do candidate RT geometry, core airgap, winding-to-winding separation, winding fill factor, turns ratio and converter operating conditions affect transferred power, current behaviour, magnetic response and represented losses at the investigated MW-class operating points?

3. Can voltage transformation be incorporated into the RT through winding turns-ratio selection while maintaining acceptable magnetic and converter operation?

These questions are addressed using analytical, FEM, linked field-circuit and experimental evidence at their respective investigation scales.

1.4.5 Research Objectives

The research questions are addressed through analytical design, electromagnetic modelling, linked field-circuit analysis and reduced-scale experimental evaluation. The corresponding objectives are:

1.To establish an integrated analytical design method for the RT-DAB system, relating magnetic sizing, winding design, airgap, turns ratio, magnetising and leakage inductances, switching frequency and phase-shift-controlled power transfer.

2.To develop and assess an electromagnetic modelling method using the 600 V/100 kW single-phase RT design, including comparison between analytical calculations and two-dimensional (2D) and three-dimensional(3D) FEM results.

3.To develop and compare the original radial, NEW1, NEW2, L-type 1 and L-type 2 RT geometries under defined electrical, magnetic and converter operating conditions.

4.To evaluate MW-class RT-DAB operation using the 1.8 kV/1 MW linked field-circuit model, including transferred power, voltage and current behaviour, magnetic response and represented winding and core losses.

5.To evaluate voltage transformation within the RT using analytical turns-ratio relationships and linked field-circuit simulations of the investigated 1:1 and 1:2 winding configurations.

6.To construct and test a reduced-scale RT-DAB platform using independently selected low-voltage parameters, and to compare the measured voltage, current and Fast Fourier Transform (FFT) derived power quantities with the analytical and numerical operating trends.

7.To define the integration boundary of the proposed rotor-to-tower interface, including the installation envelope, structural load path, airgap tolerance, alignment, thermal management, environmental protection, maintenance and condition monitoring,

and to identify the further verification required for complete turbine-level implementation.

1.5 Research Contributions

This thesis makes original contributions to the development of rotary transformer-based WPT for the rotating electrical interface of the X-ROTOR wind-turbine concept. These contributions are developed through analytical derivation, electromagnetic finite-element modelling, linked field-circuit simulation and reduced-scale experimental evaluation. The principal contributions are:

1.An application-specific RT-DAB architecture for the X-ROTOR rotor-to-tower power path.

The architecture combines a contactless RT with a phase-shift-controlled DAB interface for transferring electrical power from the rotating side to the stationary electrical system. It defines the electrical boundary of the proposed contactless interface while retaining the distinction between the investigated RT-DAB subsystem and the complete turbine-level powertrain.

2.Development of the application driven NEW1 and NEW2 RT geometries.

NEW1 and NEW2 are developed within the X-ROTOR design space as alternatives to the original radial and L-type reference geometries. Their modified magnetic paths and winding window arrangements provide different possibilities for winding accommodation, leakage-field behaviour and physical integration. The geometries are evaluated under defined analytical and numerical comparison boundaries rather than presented as universally optimal solutions.

3.A coupled magnetic and converter design method for the RT-DAB interface.

The method relates core area, winding window, conductor area, core airgap, winding separation, turns ratio, magnetising and leakage inductances to switching frequency, phase shift, converter current, transferred power and represented losses. Turns-ratio selection is also incorporated as a design variable for voltage matching within the RT. The method provides a constraint-based route from analytical sizing to FEM and linked field-circuit evaluation.

4.A staged analytical, numerical and experimental evaluation route.

The reduced-scale RT-DAB platform examines phase-shift-controlled operation under independently selected low-voltage conditions. The separate 600 V/100 kW case is used to compare analytical, 2D and 3D electromagnetic models, while the 1.8 kV/1 MW linked field-circuit model examines MW-class operation. These investigation levels are complementary and are not treated as geometrically, electrically or thermally scaled equivalents.

5.MW-class linked field-circuit evaluation of the candidate RT-DAB designs.

The three-phase 1.8 kV/1 MW model is used to compare the candidate RT geometries and to examine the effects of winding separation, fixed-window winding fill factor, converter operating condition and turns ratio. The analysis also assesses the investigated 1:1 and 1:2 voltage-transformation cases. These studies provide numerical evidence of how RT geometry and winding variables interact with converter current, transferred power, magnetic behaviour and represented losses at the investigated operating points.

Quantitative support for these contributions is developed in Chapters 3 and 4 and assessed against the research questions in Chapter 5.

1.6 Thesis Overview

Chapter 2 establishes the electrical architecture of the X-ROTOR system. It examines the two secondary generator channels, generator voltage alternatives, applicable converter topologies and the electrical power path from the rotating generator units to the stationary side. Conductive and contactless transfer options are then reviewed, and inductive WPT using an RT is selected for the rotor-to-tower interface after comparison with the principal alternatives.

Chapter 3 develops the analytical design method for the RT-DAB interface. It presents magnetic sizing, winding and airgap design, develops the original radial, NEW1, NEW2 and L-type RT geometries, and describes the operating principles of the single-phase and three-phase DAB converters. The RT design, converter operating

conditions and phase-shift control are then combined into an integrated design procedure that provides the parameter sets used in Chapter 4.

Chapter 4 evaluates the proposed interface at three investigation levels. A reduced-scale RT-DAB platform is first used to examine phase-shift-controlled operation and to compare measured and simulated terminal quantities. A separate 600 V/100 kW RT study compares analytical, 2D and 3D electromagnetic results. The investigation is then extended to a 1.8 kV/1 MW linked field-circuit model for comparison of the candidate RT geometries, winding-separation and fixed-window fill-factor effects, converter operating conditions and voltage transformation.

Chapter 5 answers the research questions using the results developed in the preceding chapters and consolidates the original contributions of the thesis. It distinguishes conclusions supported by experimental measurements from those obtained through analytical, FEM and linked field-circuit studies, identifies the limitations of the present work and defines the further mechanical, thermal, insulation, environmental and reliability studies required for full-scale implementation.

1.7 Publications

Journals

1. *Yang Teng, S. A. Mortazavizadeh, R. Yazdanpanah, D. Campos Gaona, O. Anaya Lara. " Wireless high power transfer system based on rotary transformer for novel wind turbine systems ", submitted to IEEE transactions on Energy conversion and is currently under review 2026.*

Conferences

1. *Yang Teng, O. Anaya Lara, R. Yazdanpanah, D. Campos Gaona and S. A. Mortazavizadeh, "Design and Analysis of a 100kW Rotary Transformer for XROTOR Wind Generators," 2023 IEEE Workshop on Electrical Machines Design, Control and Diagnosis (WEMDCD), Newcastle upon Tyne, United Kingdom, 2023, pp. 1 5.*
2. *Yazdanpanah, S. A. Mortazavizadeh, Y. Teng, O. Anaya Lara and D. Campos Gaona, "An Integrated Rotary Transformer and 3 Phase Dual Active Bridge Converter for High*

power Transfer in Novel X-ROTOR Wind Turbines," 2023 IEEE International Magnetic Conference (INTERMAG), Sendai, Japan, 2023, pp. 1 5.

1.8 Chapter references

[1] *O. Hoegh Guldberg et al., "Impacts of 1.5 C global warming on natural and human systems," Global warming of 1.5 C. An IPCC Special Report, 2018.*

[2] *The Climate Change Act 2008 (2050 Target Amendment) Order 2019, SI 2019/1056. London, UK: The Stationery Office, 2019.*

[3] *M. K. Johari, M. Jalil, and M. F. M. Shariff, "Comparison of horizontal axis wind turbine (HAWT) and vertical axis wind turbine (VAWT)," International Journal of Engineering and Technology, vol. 7, no. 4.13, pp. 74 80, 2018.*

[4] *W. Leithead, A. Camciuc, A. K. Amiri, and J. Carroll, "The X-ROTOR offshore wind turbine concept," in Journal of Physics: Conference Series, 2019, vol. 1356, no. 1: IOP Publishing, p. 012031.*

[5] *C. Flannigan, J. Carroll, and W. Leithead, "Operations expenditure modelling of the X-ROTOR offshore wind turbine concept," Journal of Physics: Conference Series, vol. 2265, no. 3, p. 032054, 2022.*

[6] *J. McMorland, C. Flannigan, J. Carroll, M. Collu, D. McMillan, W. Leithead, and A. Coraddu, "A review of operations and maintenance modelling with considerations for novel wind turbine concepts," Renewable and Sustainable Energy Reviews, vol. 165, p. 112581, 2022.*

[7] *H. O. Ohmstedt, "Collector ring marking or brush footprinting," in Conference Record of the 1990 Annual Pulp and Paper Industry Technical Conference, Seattle, WA, USA, 1990, pp. 51-55, doi: 10.1109/PAPCON.1990.109863.*

[8] *X. Zhu, B. Lin, L. Liu, and Y. Luan, "Power transfer performance and cutting force effects of contactless energy transfer system for rotary ultrasonic grinding," IEEE Transactions on Industrial Electronics, vol. 63, no. 5, pp. 2785-2795, May 2016.*

[9] *C. S. Wang, G. A. Covic, and O. H. Stielau, "Power transfer capability and bifurcation phenomena of loosely coupled inductive power transfer systems," IEEE Transactions on Industrial Electronics, vol. 51, no. 1, pp. 148-157, Feb. 2004.*

[10]*X. Zhu, B. Lin, and L. Liu, "Efficiency based compensations and the mechanical load dependencies of rotary transformer for rotary ultrasonic machining applications," IET Power Electronics, vol. 8, no. 6, pp. 986-993, 2015.*

[11]*R. Manko, S. Čorović, and D. Miljavec, "Analysis and design of rotary transformer for wireless power transmission," in 2020 IEEE Problems of Automated Electrodrive: Theory and Practice (PAEP), 2020.*

[12]*S. Botha and N. Gule, "Design and evaluation of a laminated three-phase rotary transformer for DFIG applications," Energies, vol. 15, no. 11, p. 4061, 2022.*

[13]*D. Guo, W. Zhu, L. Hai, D. Li, and B. Cheng, "A novel dual receivers/rectifier reconstructed WPT system with inherent CC to CV transmission characteristics and reactive power minimization," IEEE Journal of Emerging and Selected Topics in Power Electronics, vol. 13, no. 5, pp. 6709-6718, Oct. 2025, doi: 10.1109/JESTPE.2025.3571206.*

[14] *H. Xu, L. Tan, and X. Huang, "Design of a magnetic coupler for wireless power transfer systems with high rotational misalignment tolerance based on rotating magnetic flux," IEEE Journal of Emerging and Selected Topics in Power Electronics, vol. 13, no. 5, pp. 6741-6752, Oct. 2025, doi: 10.1109/JESTPE.2025.3575612.*

[15]*C. F. Ieong, P. I. Chan, I. W. Iam, and C. S. Lam, "An LCC S S compensated three coil wireless charging system for offshore USV charging," IEEE Journal of Emerging and Selected Topics in Power Electronics, vol. 13, no. 5, pp. 6768-6779, Oct. 2025, doi: 10.1109/JESTPE.2025.3582859.*

[16]*K. Detka and K. Górecki, "Wireless power transfer-A review," Energies, vol. 15, no. 19, p. 7236, 2022.*

[17]*Y. Zhang et al., "A dual side detuned S S compensated IPT system with high misalignment tolerance using a low coupling variation coil," IEEE Journal of Emerging and Selected Topics in Power Electronics, vol. 13, no. 5, pp. 6733-6740, Oct. 2025, doi: 10.1109/JESTPE.2025.3571752.*

[18]*J. Xie, Y. Chen, S. Qu, C. Luo, and J. Guo, "Dual side adaptive tuning cooperative control for tracking zero phase angle and maximum output voltage in dynamic LCC S WPT system," IEEE Journal of Emerging and Selected Topics in Power Electronics, vol. 13, no. 5, pp. 6685-6698, Oct. 2025, doi: 10.1109/JESTPE.2025.3565744.*

[19]*Y. Cui, D. Wang, and A. Emadi, "Three-phase dual active bridge converter design considerations," in IECON 2017-43rd Annual Conference of the IEEE Industrial Electronics Society, 2017.*

[20]*X. Duan, G. Yan, J. Huang, J. Qiu, C. Rong, and W. Han, "A single input dual output wireless power and information transfer system using DDQ nested coils for motor drives," IEEE Journal of Emerging and Selected Topics in Power Electronics, vol. 13, no. 5, pp. 6676-6684, Oct. 2025, doi: 10.1109/JESTPE.2025.3565497.*

[21]*S. J. van Heerden and H. J. Vermeulen, "Model based condition monitoring of a doubly fed induction generator slip ring component," in 2013 48th International Universities' Power Engineering Conference (UPEC), 2013, pp. 1-6, doi: 10.1109/UPEC.2013.6714965.*

[22]*L. Morgan, W. Leithead, and J. Carroll, "On the use of secondary rotors for vertical axis wind turbine power take off," Wind Energy, vol. 27, no. 6, pp. 569-582, 2024.*

[23]*H. Krupp and A. Mertens, "Rotary transformer design for brushless electrically excited synchronous machines," in 2015 IEEE Vehicle Power and Propulsion Conference (VPPC), Montreal, QC, Canada, 2015, pp. 1-6, doi: 10.1109/VPPC.2015.7353009.*

[24]*Y. Zhang, J. Yang, D. Jiang, D. Li, and R. Qu, "Design, manufacture, and test of a rotary transformer for wireless power transfer system," IEEE Transactions on Magnetics, vol. 58, no. 2, pp. 1-6, Feb. 2022, Art. no. 8400206, doi: 10.1109/TMAG.2021.3094135.*

[25]*D. C. Ludois, K. Hanson, and J. K. Reed, "Capacitive power transfer for slip ring replacement in wound field synchronous machines," in 2011 IEEE Energy Conversion Congress and Exposition, Phoenix, AZ, USA, 2011, pp. 1664-1669, doi: 10.1109/ECCE.2011.6063982.*

[26]*T. Raminosoa, R. H. Wiles, and J. Wilkins, "Novel rotary transformer topology with improved power transfer capability for high speed applications," IEEE Transactions on Industry Applications, vol. 56, no. 1, pp. 277-286, Jan.-Feb. 2020, doi: 10.1109/TIA.2019.2955050.*

[27]*D. Campos Gaona, A. Stock, W. Leithead, and O. Anaya Lara, Secondary Rotors and Power Train Design, X-ROTOR Project Deliverable D5.1, University of Strathclyde, Dec. 2021, Grant Agreement No. 101007135.*

[28]*R. Yazdanpanah, S. A. Mortazavizadeh, D. Campos Gaona, and O. Anaya Lara, Scaled Rotatory Transformer Models, Design and Control, X-ROTOR Project Deliverable D5.2, University of Strathclyde, Dec. 2022, Grant Agreement No. 101007135.*

[29]*S. A. Mortazavizadeh, R. Yazdanpanah, D. Campos Gaona, and O. Anaya Lara, Control System for the Power Electronics and Rotatory Transformer Arrangement, X-ROTOR Project Deliverable D5.3, University of Strathclyde, Feb. 2024, Grant Agreement No. 101007135.*

[30]*D. Hall and R. P. Roberge, "Carbon brush performance on slip rings," in Conference Record of 2010 Annual Pulp & Paper Industry Technical Conference, 2010, pp. 1-6, doi: 10.1109/PAPCON.2010.5556522.*

[31]*W. Würfel and W. Hofmann, "Monitoring of the transmission properties of the rotor slip ring system of doubly fed induction generators," in IEEE International Conference on Electric Machines and Drives, 2005, pp. 295-299, doi: 10.1109/IEMDC.2005.195737.*

[32]*T. H. Houenouvo and W. Hofmann, "Diagnostics of the transmission properties of the slip ring system in doubly fed induction generators," in 2014 IEEE 60th Holm Conference on Electrical Contacts, 2014, pp. 1-7, doi: 10.1109/HOLM.2014.7031019.*

[33]*G. Dorsey, "High reliability slip ring design for wind turbines," Moog Inc., White Paper MS3333, Apr. 2019.*

[34]*K. Kate singnoy and S. Premrudeepreechacharn, "Age estimation of electrographite brush in generator system for optimised maintenance planning of Sirikit hydro power plant," in 2014 North American Power Symposium (NAPS), 2014, pp. 1-6, doi: 10.1109/NAPS.2014.6965393.*

[35]*K. Fukuda, K. Sawa, and T. Ueno, "Relationship between brush current change and contact voltage drop in sliding contact with steel slip ring and various silver graphite brushes," in 2020 IEEE 66th Holm Conference on Electrical Contacts and Intensive Course, 2020, pp. 105-109, doi: 10.1109/HLM49214.2020.9307888.*

[36]*R. C. Reuter, Jr., and M. H. Worstell, "Torque ripple in a vertical axis wind turbine," Sandia Laboratories, Rep. SAND78 0577, Apr. 1978.*

[37]*K. W. Chase and A. R. Parkinson, "A survey of research in the application of tolerance analysis to the design of mechanical assemblies," Research in Engineering Design, vol. 3, pp. 23-37, 1991, doi: 10.1007/BF01580066.*

[38]*ISO 1101:2017, Geometrical Product Specifications (GPS)-Geometrical Tolerancing-Tolerances of Form, Orientation, Location and Run-out. Geneva, Switzerland: International Organization for Standardization, 2017.*

Chapter 2

2 Electrical Architecture and Selection of Contactless Power Transfer for the X-ROTOR

2.1 Introduction

Chapter 1 defined the X-ROTOR rotor-to-tower electrical power transfer problem and the principal requirements of a contactless interface. This chapter establishes the electrical architecture needed to place that interface within the X-ROTOR powertrain. It considers the secondary generator channels, generator voltage and converter alternatives, coordination of the two generator outputs, and the selection of the rotating power transfer technology.

Sections 2.2-2.4 examine the generator side of the system. The two secondary PMSG channels are treated as independently controlled electrical sources because their instantaneous mechanical and electrical operating points need not be identical. The 690 V and 3.3 kV generator-converter alternatives are compared before the complete power path is defined from the secondary rotor shaft and variable-frequency PMSG output to the controlled rotating direct current (DC) interface.

Sections 2.5 and 2.6 consider the transfer across the rotating boundary. The slip ring is retained as the conductive reference, after which near-field and far-field wireless power transfer methods are distinguished and inductive and capacitive coupling are compared. This comparison leads to the selection of a rotary transformer-based inductive interface for the RT-DAB design developed in Chapter 3.

2.2 Electrical Configuration of the X-ROTOR Powertrain

The mechanical roles and reference operating conditions of the primary and secondary rotors are defined in Section 1.2. From an electrical perspective, generation is provided by two permanent-magnet synchronous generators (PMSGs) mounted on the rotating primary structure, with one 2.5 MW generator driven by each secondary rotor. The primary rotor does not directly drive a central electrical generator[1][2][3][4].

The two generator channels need not operate at identical instantaneous mechanical or electrical conditions because the effective inflow, shaft torque and rotational speed of each secondary rotor vary with primary rotor azimuth[1][2][3][4]. Each PMSG is therefore connected to an independently controlled, fully rated machine side converter. The converter regulates stator current and electromagnetic torque and converts the variable-frequency three-phase generator output to controlled DC power. Direct paralleling of the uncontrolled PMSG terminals is not adopted because their voltage magnitudes, frequencies and phase angles are not inherently identical.

In the project-level architecture, each three-phase wireless power transfer channel is represented by three RT phase units, giving six electromagnetic RT units for the two generator channels[4]. The 1.8 kV/1 MW three-phase RT-DAB model investigated later in the thesis represents a MW-class transfer stage within this wider architecture rather than the complete combined output of the two 2.5 MW generators. Full turbine-level implementation would also require definition of channel rating, current sharing, protection, redundancy and thermal coordination.

Figure 2.1 shows the physical arrangement of the primary and secondary rotors. For the electrical analysis developed in the following sections, the system is treated as two independently controlled rotating generator-converter channels feeding the rotor-to-tower power transfer interface. Section 2.3 establishes the generator voltage and converter basis, while Section 2.4 follows the electrical power path and coordination of the two channels.

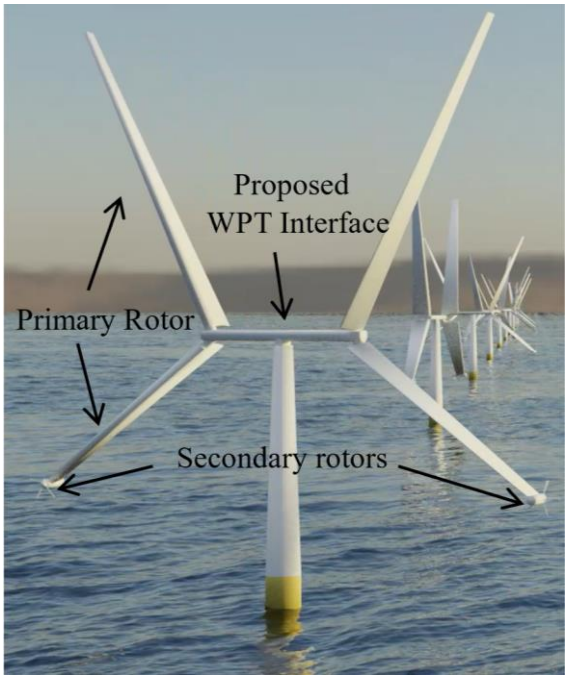


Figure 2.1 X-ROTOR architecture showing the primary and secondary rotors[1]

2.3 Secondary Generator Voltage and Converter Topology Selection

The generator terminal voltage and the machine side converter must be considered together because the selected voltage determines the current requirement, conductor rating, converter structure, insulation coordination, protection requirements and practical operating range. The 690 V low-voltage and 3.3 kV medium voltage alternatives are therefore compared at the same 2.5 MW generator rating[3].

2.3.1 Generator Voltage Alternatives

Commercial megawatt-scale PMSG systems have used both low- and medium voltage architectures. Table 2.1 gives representative examples that establish the design context for the X-ROTOR generator study, it is not intended as a current manufacturer catalogue. Table 2.2 identifies 690 V as low voltage and 3.3 kV as medium voltage under the International Electrotechnical Commission (IEC) voltage classification adopted in this thesis. Rated power alone does not determine the generator voltage because

converter topology, current rating, insulation, manufacturer practice and drivetrain integration also influence the selection[5]-[10].

Table 2.1 Examples of megawatt-scale PMSG voltage and converter arrangements

System / Design case	Rated power	Rated voltage	Typical converter arrangement
GE 2.5XL	2.5 MW	690 V	Low voltage fully rated converter
Avantis AV928	2.5 MW	690 V	Low voltage fully rated converter
Areva M5000	5 MW	3.3 kV	Medium voltage multilevel converter
ABB PCS6000 application	6 MW	3.3 kV	Medium voltage multilevel converter
X-ROTOR secondary generator alternatives	2.5 MW	690 V/3.3 kV	Compared to equal power rating

Table 2.2 Voltage classes used in the generator comparison

Voltage class	IEC based range used in this thesis	Representative level
Low voltage	Below 1kV AC	690 V
Medium voltage	1 35 kV AC	3.3 kV

Under the IEC terminology adopted in this thesis, 690 V is classified as low voltage and 3.3 kV as medium voltage, as summarised in Table 2.2[6].

For a balanced three-phase generator, the line current is

$$I_{line} = \frac{P}{\sqrt{3}V_{LL}\eta\, PF} \tag{2.1}$$

where P is active power, V_{LL} is line-to-line root mean square (RMS) voltage, I_{line} is line current, η is efficiency and PF is power factor. At equal power, efficiency and power factor.

$$\frac{I_{line,690}}{I_{line,3300}} \approx \frac{3300}{690} = 4.78 \tag{2.2}$$

Equation (2.2) shows the fundamental current reduction obtained by increasing the generator voltage. The optimised project generator models report RMS q-axis current values of approximately 2531 A for the 690 V design and 526 A for the 3.3 kV design[3].

These are model quantities rather than independent measurements of line current, but their ratio is consistent with the current reduction expected when the voltage is increased at comparable power. The lower-voltage design therefore places a substantially greater current burden on the generator windings, converter devices, busbars, cables and associated cooling system.

The 690 V arrangement is compatible with mature modular two-level converter technology. Parallel converter modules can be used to provide the required current capability and a degree of redundancy, although this introduces current-sharing, circulating-current, conductor and cooling requirements[7][8][9][10].

The 3.3 kV arrangement reduces the current requirement and is compatible with a three-level medium voltage converter. This reduces the current rating required of cables, busbars and other current-dependent components, but introduces medium voltage insulation coordination, electrical-clearance, protection, switching, isolation and test-equipment requirements. Although 690 V is classified as low voltage under the IEC terminology used here, it remains a high energy industrial system requiring competent personnel and controlled access. Work on the 3.3 kV system additionally requires personnel authorised for medium voltage switching, isolation and testing in accordance with the applicable site electrical-safety procedures[3][5][8] [12].

The project generator comparison gives stator outer diameters of approximately 1846 mm for the 690 V design and 1633 mm for the 3.3 kV design [3]. The corresponding permanent-magnet masses are 754.88 kg and 743.42 kg, while the total generator masses are 7686.64 kg and 7702.03 kg, respectively. The compared 3.3 kV design therefore has a smaller stator outer diameter, but the differences in permanent-magnet mass and total generator mass are small. These results do not support a general conclusion that increasing the generator voltage necessarily produces a substantially lighter machine or substantially reduces permanent-magnet material. Machine dimensions and material requirements remain dependent on the complete electromagnetic, thermal and mechanical design.

The calculated generator efficiencies are also close, at approximately 98.607% for the 690 V design and 98.52% for the 3.3 kV design[3]. Generator voltage is therefore selected at generator-converter-system level, taking account of current rating, converter

architecture, insulation, conductors, protection and operating requirements rather than generator mass or efficiency alone.

2.3.2 Applicable Generator Side Converter Topologies

Three generator side alternatives are considered: a parallel two-level active voltage-source converter (VSC), a three-level neutral-point-clamped (NPC) active VSC, and a passive diode-front-end converter followed by controlled downstream conversion[6][9].

The two-level active VSC is a mature solution for low-voltage Type-IV wind turbines. It provides direct control of generator current and electromagnetic torque and converts the variable-frequency PMSG output to a regulated DC link. At 690 V and 2.5 MW, however, the high current requires parallel converter modules, with associated current-sharing, circulating-current and cooling requirements.

The three-level NPC converter is appropriate to the 3.3 kV alternative because the DC link voltage stress is distributed among multiple semiconductor devices. The reduced current lowers the required current rating of the converter and conductors. The principal penalties are the increased semiconductor count, neutral-point-voltage balancing, more complex gate-drive and protection arrangements and lower modular redundancy[3][5][7][10][11][12][13].

A passive diode-front-end reduces the number of controlled semiconductor devices, but it does not regulate the PMSG phase currents in the same manner as an active VSC. Characteristic current harmonics can produce electromagnetic-torque ripple, which is undesirable for the secondary rotor drivetrain. The passive arrangement is therefore not retained as the reference generator side topology[9].

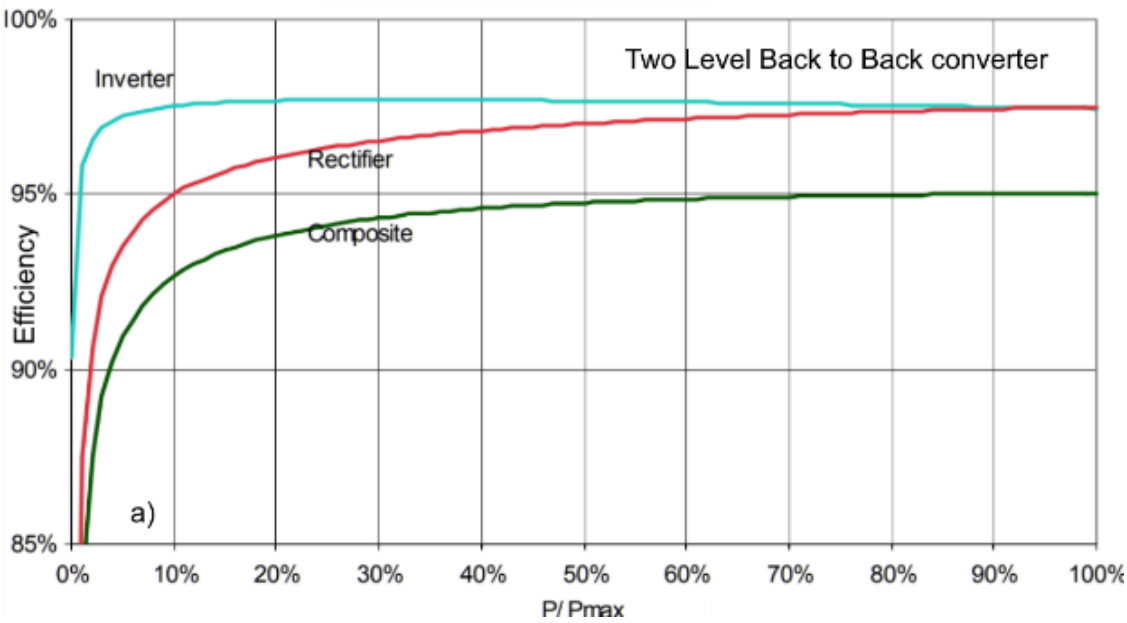
The machine side converter is distinct from the DAB used at the rotating interface. The former converts the variable-frequency PMSG output to controlled DC power, whereas the DAB converts that DC power to medium frequency AC for transfer through the RT before DC power is reconstructed on the stationary side. Detailed single-phase and three-phase DAB operation is developed in Chapter 3[14][15][16].

The main advantages and limitations of the three generator side converter arrangements are summarised in Table 2.3.

Table 2.3 Comparison of generator side converter topologies

Topology	Main advantages	Main limitations	Application to X-ROTOR
Parallel two-level active VSC	Mature technology, modularity, redundancy, full generator-current control	High current at 690 V, current sharing and cooling requirements	690 V alternative
Three-level NPC active VSC	Lower current at 3.3 kV, distributed semiconductor voltage stress	Higher device count, neutral-point balancing, Medium Voltage insulation and protection	3.3 kV reference arrangement
Passive diode front end	Low controlled-switch count, simple rectification	Uncontrolled current harmonics, reduced generator-current control	Not selected

Figure 2.2 shows the representative converter-efficiency trends reported for the low- and medium voltage arrangements used in the source comparison. The figure provides supporting context for the converter assessment, but the reported efficiency difference is not used as the principal basis for selecting the generator side arrangement. The voltage and converter selection is instead considered together with current rating, converter structure, conductor requirements, insulation, protection and system integration.



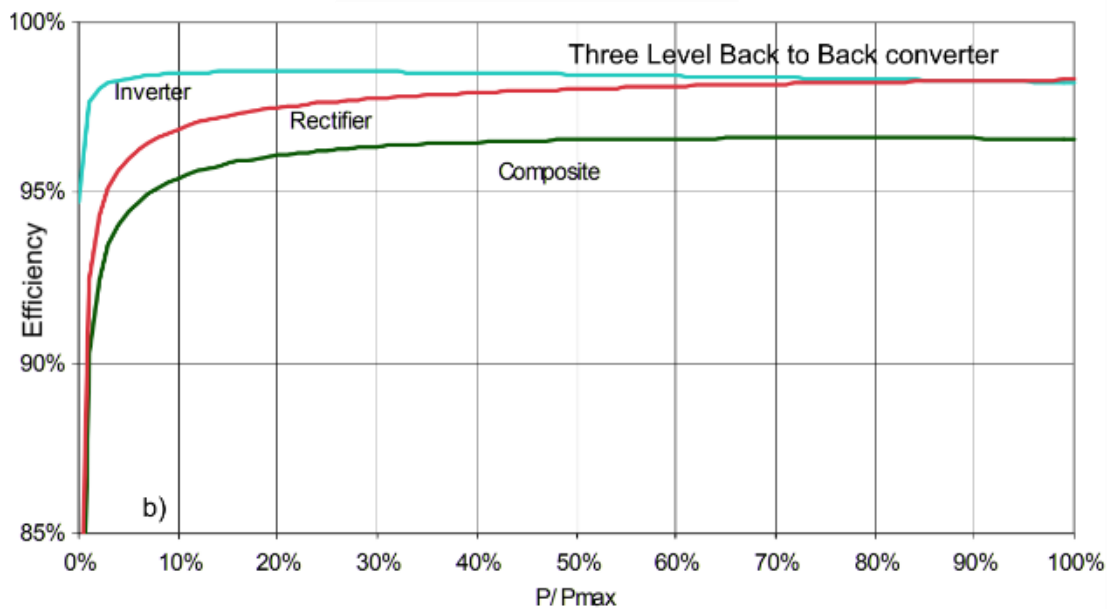


Figure 2.2 Efficiency curves of the compared two-level and three-level converter arrangements[3][10].

2.3.3 Selected Generator Side Arrangement

For the project-level secondary generator drivetrain, the 3.3 kV PMSG with an independently controlled three-level NPC converter is adopted as the reference generator side arrangement. The principal reasons are the lower current requirement, the smaller stator outer diameter reported for the compared project design, the reduced cable and busbar current burden and compatibility with medium voltage conversion. The selection is not based on an assumption that the 3.3 kV generator is universally lighter, more efficient or less costly.

The 690 V alternative remains technically credible. It benefits from mature modular two-level converter technology and greater converter redundancy, but the approximately fivefold current increase at the same power level requires parallel converter modules and high current conductors. The 3.3 kV alternative reduces the current burden but introduces medium voltage insulation, protection, switching and maintenance requirements.

The principal differences between the 690 V and 3.3 kV generator-converter arrangements are summarised in Table 2.4.

Table 2.4 Comparison of the 690 V and 3.3 kV generator-converter arrangements

Characteristic	690 V arrangement	3.3 kV arrangement
Rated generator power	2.5 MW	2.5 MW
Reported RMS q-axis current (project model)	2531 A	526 A
Approximate DC link basis	1.2 kV	5.3-5.4 kV
Converter arrangement	Parallel two level VSC modules	Three level NPC VSC
Stator outer diameter	1846 mm	1633 mm
PM mass	754.88 kg	743.42 kg
Total generator mass	7686.64 kg	7702.03 kg
Calculated efficiency	98.607%	98.52%
Main engineering consequence	High current, mature modular low-voltage converter technology	Lower current, additional Medium Voltage insulation and protection requirements

The converter comparison uses an approximately 5.3 kV DClink basis, while the later turbine-level control model uses a nominal value of approximately 5.4 kV. This small difference results from model development and rounding and does not represent a different electrical architecture[3][5].

The 3.3 kV arrangement defines the project-level generator side reference used in the subsequent system architecture. The 1.8 kV/1 MW RT-DAB model investigated in Chapters 3 and 4 is a separate MW-class subsystem study and is not a direct one-to-one implementation of either complete 2.5 MW generator channel.

2.4 Electrical Power Flow and Coordination of the Two Secondary Generator Channel

The generator voltage and converter comparison in Section 2.3 defines the source-side electrical arrangement. This section follows the power path from each secondary

rotor shaft to the stationary grid-side interface and considers how the two generator channels can operate under different instantaneous mechanical inputs.

2.4.1 Secondary Rotor Generation and Machine side Conversion

Each secondary rotor drives an individual PMSG. Because the generator operating point varies with secondary rotor speed and effective inflow, its shaft torque, terminal voltage and electrical frequency can vary with primary rotor azimuth, as discussed in Section 1.2.1.

Each PMSG is connected to an independently controlled, fully rated active machine side converter. The converter regulates the generator currents and electromagnetic torque. Under the adopted vector-control representation, the q-axis current principally controls electromagnetic torque and active power, while the d-axis current is assigned according to the selected flux and reactive-current strategy[3][4]. The variable-frequency three-phase generator output is converted to controlled DC power, so the two PMSGs do not require direct electrical-frequency or phase synchronisation before the downstream power transfer stage.

2.4.2 Complete Energy Conversion and Power Flow Path

Figure 2.3 shows the complete energy conversion path for one secondary generator channel. Aerodynamic power captured by the secondary rotor is converted to mechanical shaft power and then to variable-frequency three-phase AC by the PMSG. The machine side converter regulates the generator current and torque and supplies controlled DC power to the rotating DC link. The rotating-side DAB bridge converts this DC power to medium frequency three-phase AC for excitation of the RT. Power is transferred magnetically across the rotating airgap, after which the stationary-side DAB bridge reconstructs the stationary DC link. The grid-side converter then converts the

DC power to grid-frequency AC for delivery through the required grid-interface equipment[4].

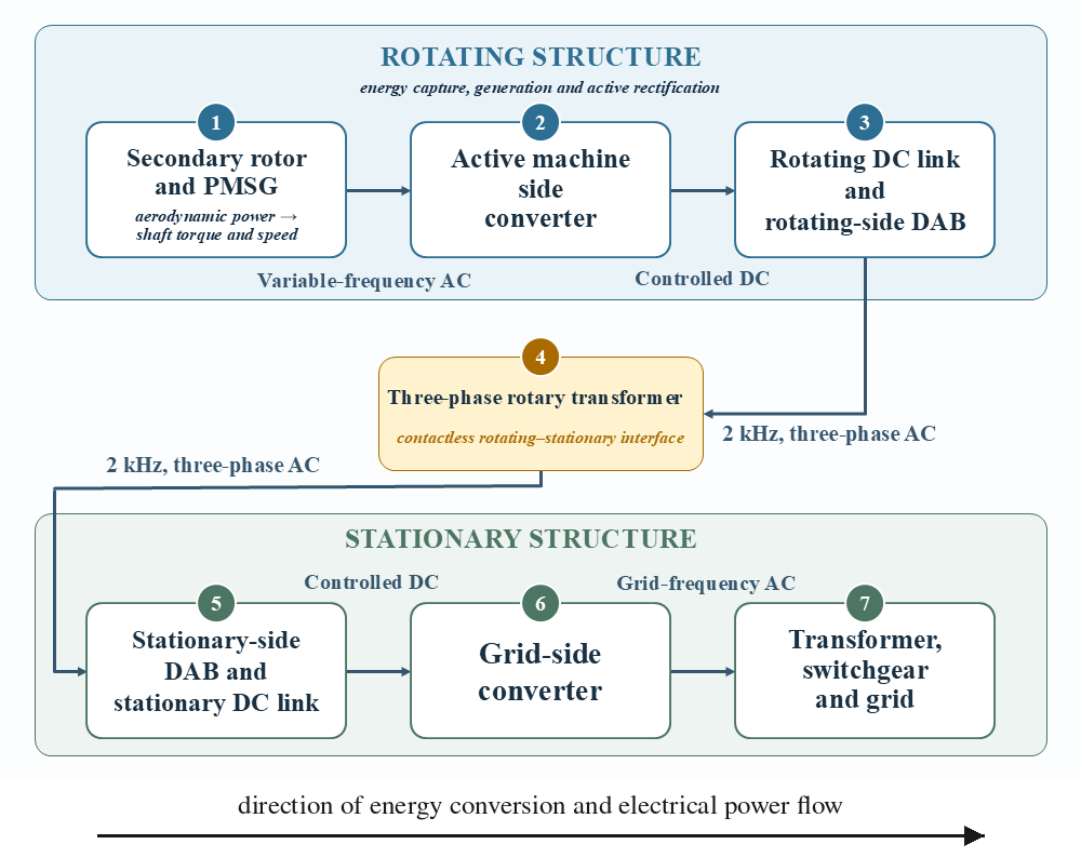


Figure 2.3 Electrical power path for one X-ROTOR secondary generator channel

2.4.3 Coordination Under Unequal Effective Inflow

Azimuthal variation of the effective inflow can produce different instantaneous mechanical conditions at the two secondary rotors. Their PMSGs may therefore operate at different rotational speeds and shaft torques and produce different instantaneous electrical powers.

Generator speed determines electrical frequency and contributes to the back-EMF magnitude, while each active machine side converter regulates its own generator current and electromagnetic torque. The two PMSGs can therefore operate at different electrical

frequencies while supplying controlled DC power to the downstream interface. Direct synchronisation of the generator terminals is not required.

Coordination is performed through the individual generator-current and torque commands, DC link voltage limits and the power commands applied to the downstream RT-DAB channels[4]. A short-duration difference between generated and transferred power can be absorbed by the DC link capacitance within its permitted voltage range. Supervisory control is required to keep the generator converters, DC links and RT-DAB stages within their specified current, voltage and thermal limits.

Table 2.5 Connection options for the two secondary generator channels

Architecture	Advantages	Limitations	Use in this thesis
Direct AC paralleling	Minimum aggregation hardware	Requires matched voltage, frequency and phase, mismatch may produce circulating current	Not adopted
Separate AC channels with independent conversion	Independent generator operation, clear fault isolation	Duplicated conversion hardware	Feasible
Independent active converters feeding a common rotating DC bus	Allows asynchronous generator operation and DC domain aggregation	Common-bus fault duty and protection requirements	Compatible with the adopted DC domain coordination
Independent DC links with coordinated RT-DAB channels	Greater modularity and fault isolation	Additional converter/magnetic hardware and power sharing control	Alternative DC domain arrangement

Direct AC paralleling is not adopted because the two PMSG outputs are not inherently matched in voltage magnitude, electrical frequency and phase. Independent active machine side conversion allows each generator to operate at its own instantaneous operating point before coordination in the DC domain.

A common rotating DC bus can reduce downstream converter duplication, whereas independent DC links and RT-DAB channels provide greater modularity and fault isolation. Selection between these two DC domain implementations depends on turbine-level protection, redundancy, packaging, availability and maintenance

requirements. The present thesis therefore adopts independent active conversion followed by DC domain coordination as the architectural principle, without prescribing the final number or rating of full-turbine RT-DAB channels.

2.5 Rotating Power transfer Interface: Conductive Reference and Contactless Alternatives

Section 1.3 examined the degradation and maintenance mechanisms associated with sliding electrical contacts. This section uses the slip ring as the conductive reference for the X-ROTOR rotor-to-tower interface.

Figure 2.4 shows the generator-specific failure distribution. Slip ring-related faults account for approximately 31% of the identified generator failures in that dataset. The reported percentage is specific to the turbine population, slip ring design, operating environment and maintenance practice represented in [17].

For offshore systems, the consequence of component maintenance also depends on access, intervention requirements and the wider O&M strategy, which are particularly relevant to novel wind-turbine concepts[18][19].

Condition-monitoring studies have examined slip ring transmission characteristics, contact voltage and brush condition, including model-based diagnosis, brush-age estimation and experimental measurements of brush current and contact-voltage behaviour[20]-[26]. These methods can assist fault detection and maintenance planning, but they do not remove the sliding electrical contact or the eventual need to inspect and replace wear components. Industrial guidance similarly emphasises contact-material selection, sealing, debris control, brush pressure and planned maintenance[27].

A suitably rated slip ring therefore remains a technically feasible means of transferring power across the rotating boundary. For the present X-ROTOR study, however, a contactless interface is preferred because it removes the sliding electrical contact and its associated brush-wear mechanism. The following section therefore compares the available wireless power transfer mechanisms against the electrical, mechanical and integration requirements of the rotor-to-tower interface.

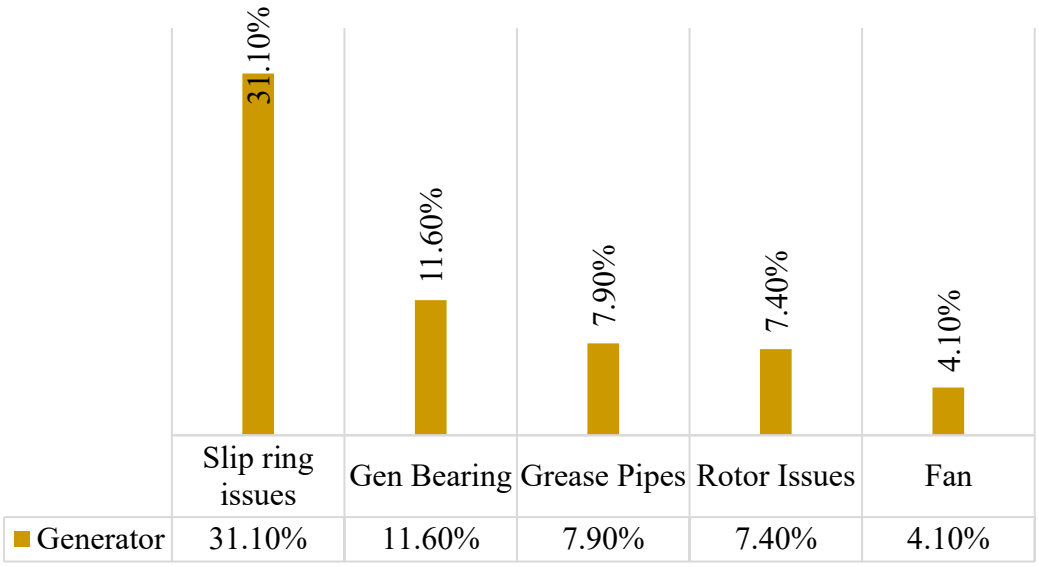


Figure 2.4. Reported generator failure modes in offshore wind turbines[17]

2.5.1 Electromagnetic Field Regimes and Transfer Distance

The distinction between near-field and far-field WPT is based on electromagnetic field behaviour rather than a universal distance threshold[28]-[31]. For an excitation frequency f, the free space wavelength is

$$\lambda_{em} = \frac{c}{f} \tag{2.3}$$

where c is the speed of light. A commonly used order of magnitude indicator for the reactive near field region is

$$d \ll \frac{\lambda_{em}}{2\pi} \tag{2.4}$$

where d is the separation between the transmitting and receiving structures. Equation (2.4) is a field-regime indicator rather than a universal engineering boundary. Practical near-field WPT must also be considered relative to the physical dimensions of the coupler and the resulting mutual inductance or coupling capacitance.

Near-field systems include millimetre-scale clearances in rotary transformers, centimetre-scale industrial couplers and separations of several tens or hundreds of millimetres in some stationary and dynamic vehicle-charging systems[32]-[35]. Far-field applications operate over substantially longer distances and may extend from metres to kilometres, depending on frequency, antenna or optical-aperture dimensions, transmitted power, pointing accuracy and atmospheric conditions[30][31].

The RT arrangements considered in this thesis operate with millimetre-scale magnetic clearances. The intermediate 600 V/100 kW RT uses a nominal 1 mm core-to-core airgap. The published 1.8 kV/1 MW X-ROTOR RT-DAB study uses a 5 mm magnetic airgap[48]. In the final MW-class sensitivity study developed in Chapter 4, the topology-specific core gaps are retained while the separate 5, 10 and 15 mm series refers to primary-to-secondary winding separation. Magnetic airgap and winding separation are treated as separate geometric quantities in the analyses that follow.

Figure 2.5 summarises the classification used in this thesis, separating near-field inductive and capacitive coupling from far-field radio frequency, microwave and optical transfer.

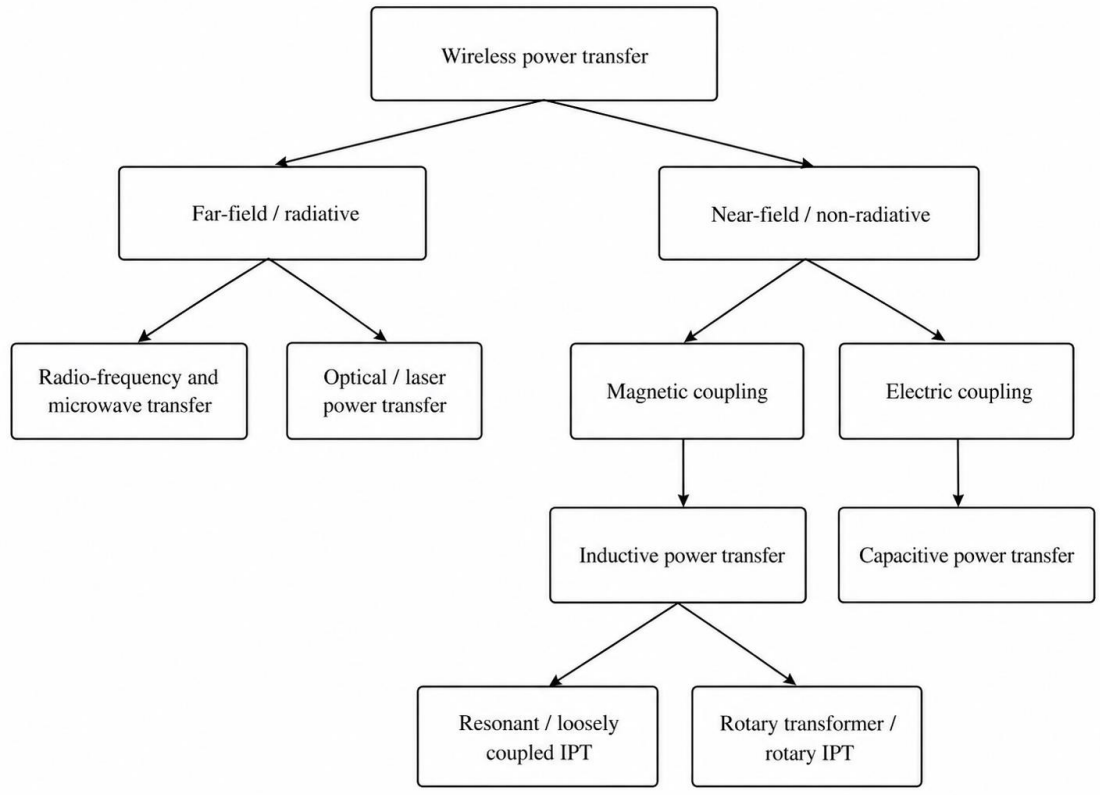


Figure 2.5 Classification of WPT by field regime and coupling mechanism.

2.5.2 Far Field Wireless Power Transfer

Far Field WPT transfers energy through propagating electromagnetic radiation. Radio frequency and microwave systems use transmitting antennas and receiving antennas or rectennas, while optical systems use a directed light source and a photovoltaic or photoelectric receiver[30][31].

Microwave power transfer can operate over long distances but requires directional antennas, adequate receiving aperture, electromagnetic-compatibility control and multiple conversion stages. Optical power transfer can provide a more concentrated beam but requires an unobstructed line of sight, accurate pointing and tracking, and consideration of atmospheric attenuation and personnel safety.

The X-ROTOR interface requires power transfer only across a controlled millimetre-scale rotating clearance. A radiative system would introduce antenna or optical conversion, alignment and containment requirements without providing a useful transfer-distance advantage for this application. Far-field WPT is therefore not retained for the rotor-to-tower interface.

2.5.3 Near Field WPT and Inductive Power Transfer (IPT)

In an IPT system, alternating current in the transmitting winding produces a time-varying magnetomotive force (MMF) and magnetic flux. A portion of this flux links the receiving winding and induces an electromotive force in accordance with Faraday's law. The transmitting and receiving windings therefore form a magnetically coupled system separated by a physical clearance[32] [35].

The alternating excitation is generated by a power electronic inverter. In parts of the WPT literature, this circuit is referred to as an oscillator because it converts a DC link voltage into periodic medium or high frequency AC excitation. In this thesis, the term power electronic inverter is used when referring to this function to distinguish it from mechanical oscillation.

The unloaded quality factor of winding Q_i is

$$Q_i = \omega \frac{L_i}{R_i} \tag{2.5}$$

where ω is the excitation angular frequency in rad s^{-1}, L_i is the winding self-inductance in H, R_i is the effective AC winding resistance in Ω, and Q_i is dimensionless.

The magnetic coupling coefficient is

$$k = \frac{M}{\sqrt{L_p L_s}} \tag{2.6}$$

where M is mutual inductance and L_p and L_s are the primary and secondary winding self-inductances, respectively.

Power transfer capability and efficiency depend jointly on coupling coefficient, winding quality factors, compensation, loading and converter operating point. Neither transferable power nor efficiency can be inferred from physical separation alone[34]-[40].

A rotary transformer is an application-specific form of IPT in which the primary and secondary windings and their associated magnetic-core sections are separated by a controlled rotating airgap. One magnetic assembly is attached to the rotating structure and the other to the stationary structure. The airgap permits relative mechanical rotation between the two assemblies, the transferred electrical power is produced by electromagnetic excitation rather than by the mechanical rotation itself[41][42].

In the proposed X-ROTOR architecture, the RT is located between the rotating-side and stationary-side active bridges of the DAB converter. The bridges generate the medium frequency excitation and regulate active-power transfer through their commanded phase displacement[14][15][16][43]. The RT can also provide voltage transformation through its winding turns ratio. The extent to which this function can replace other transformer stages remains dependent on insulation coordination, protection and grid-interface requirements.

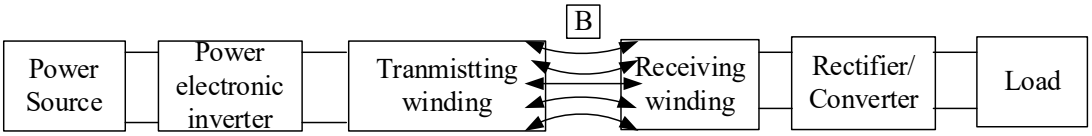


Figure 2.6 Inductive WPT system

Figure 2.6 illustrates the functional stages of a generic inductive WPT link. The source-side power electronic stage produces the alternating excitation applied to the transmitting winding, magnetic coupling transfers energy to the receiving winding, and the receiving-side conversion stage supplies the electrical load. For the proposed X-ROTOR interface, the transmitting and receiving windings correspond to the rotating and stationary RT windings, while the generic source- and receiver-side conversion stages are replaced by the two actively controlled DAB bridges shown in Figure 2.3 and developed in Chapter 3.

The compensation arrangements in Table 2.6 are representative of conventional resonant IPT systems. They are not adopted as separate compensation networks in the RT-DAB stage considered in this thesis. Here, transferred power is regulated by the relative phase displacement between the two active bridges, while the effective transfer inductance comprises the RT leakage inductance together with any deliberately introduced series inductance. The electrical behaviour of this transfer path is developed quantitatively in Chapter 3.

These arrangements are representative of conventional resonant IPT systems but are not used as separate compensation networks in the RT-DAB stage considered here.

Table 2.6 Common compensation arrangements for resonant IPT[36]-[40]

Compensation arrangement	Transmitter side	Receiver side
Series-Series	Series capacitor	Series capacitor
Series-Parallel	Series capacitor	Parallel capacitor
Parallel-Series	Parallel capacitor	Series capacitor
Parallel-Parallel	Parallel capacitor	Parallel capacitor

2.5.4 Capacitive Power Transfer

CPT transfers energy through an alternating electric field established between conductive electrodes. A high frequency inverter applies an alternating voltage to the transmitting electrodes, producing displacement current through the coupling

capacitance. A compensation network and receiving-side rectifier or active converter then deliver power to the load[44][45][46][47].

For an idealised parallel plate arrangement

$$C \approx \frac{\varepsilon A_p}{d} \tag{2.7}$$

where ε is the effective permittivity, A_p is the effective overlapping plate area and d is the plate separation. Equation (2.7) shows that the nominal coupling capacitance increases with plate area and permittivity and decreases as the separation increases. Practical CPT systems also contain fringing fields, parasitic capacitances, non-uniform electric-field distributions and common-mode paths that are not represented by the ideal parallel-plate relationship.

CPT avoids the magnetic core required by an RT and therefore removes the associated magnetic-core mass and core loss. Its coupling capacitance can, however, be relatively small, requiring higher plate voltage, operating frequency or compensation current for a specified transferred power. Plate separation and overlap directly influence the coupling capacitance, while insulation, moisture, contamination, edge-field concentration and common-mode current require separate consideration.

The generic CPT power path is shown in Figure 2.7, comprising high frequency excitation, the capacitive coupling interface and receiving-side power conversion.

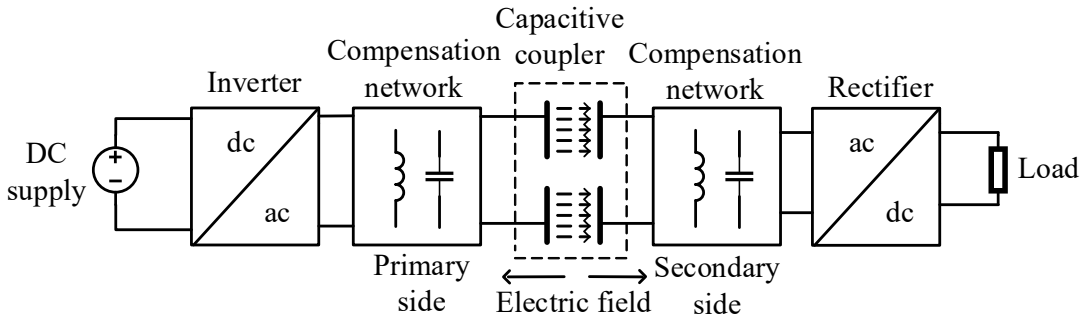


Figure 2.7 Capacitive WPT system [44]

A rotating CPT system employing a Class-E inverter and a Ruthroff balun is reported in [46]. In this system, the transmitter is stationary and the receiver rotates across the capacitive interface. The Class-E inverter converts the DC input to 6.78 MHz AC excitation and feeds a 1:1 Ruthroff transmission-line balun designed for a 50 Ωsystem. The balun divides the Class-E output into two out-of-phase signals that are

applied to the resonant capacitive interface. It is also connected to the shield plate to stabilise its ground potential. The Ruthroff balun therefore forms part of the transmitter-side high frequency excitation circuit rather than the contactless power transfer interface itself. Figure 2.8 shows the resulting functional arrangement.

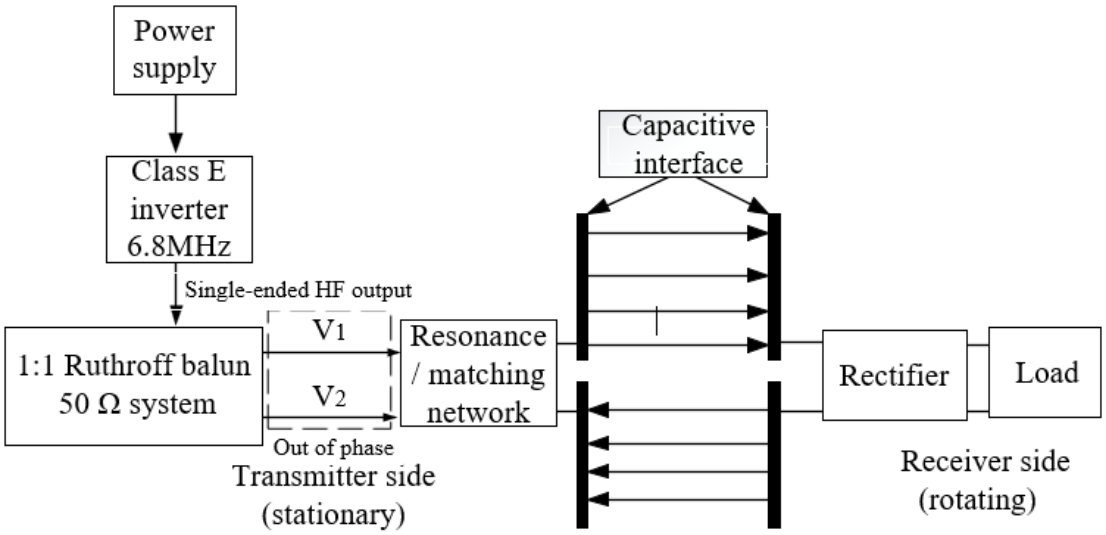


Figure 2.8 Rotating CPT system with a Class-E inverter and Ruthroff balun[46]

CPT has also been investigated for contactless excitation of wound-field synchronous machines[47]. In this application, the capacitive interface replaces the brush-and-slip ring path used to supply rotor-field current. CPT therefore replaces the rotating electrical excitation contact rather than the electrical machine itself, and its use does not determine the broader choice between permanent-magnet and wound-field generator architectures.

2.5.5 Engineering Comparison of IPT and CPT

The choice between IPT and CPT depends on the required power, mechanical clearance, coupler geometry, alignment, operating frequency, electrical stress and converter arrangement. CPT offers a low-profile electrode structure, whereas IPT provides a guided magnetic path and transformer action through the winding turns ratio. Figure 2.7 compares these characteristics for the X-ROTOR interface [35][39][44]-[47].

Table 2.7 Engineering Comparison of IPT and CPT for the X-ROTOR Interface

Criterion	IPT / rotary transformer	CPT
Coupling mechanism	Mutual magnetic flux links the primary and secondary windings	Displacement current flows through the electric field between the electrodes
Gap sensitivity	Increasing the magnetic airgap increases reluctance and generally reduces magnetic coupling	Increasing plate separation reduces coupling capacitance
Efficiency	Depends on coupling, leakage and magnetising inductance, winding/core losses and converter operation	Depends on coupling capacitance, operating voltage, frequency, parasitic capacitance, compensation and converter losses
Power capability	Depends on magnetic cross-section, winding area, current density, frequency, flux density and cooling	Depends on electrode area, voltage, frequency, insulation and compensation current
Alignment	Displacement changes mutual coupling, leakage and local magnetic field	Displacement changes electrode overlap and coupling capacitance
Coupler dimensions	Set by core area, winding window, turns, conductor area and clearances	Set by electrode area, separation, edge clearance, return path and insulation
Active-area effect	Larger core or winding area can increase magnetic and current-loading capability, power does not scale directly with area	Larger electrode area increases capacitance for fixed separation and permittivity, power does not scale directly with area
Field-control requirements	Requires control of magnetic leakage field, insulation and temperature	Requires control of electric field, insulation and common-mode current
Rotating operation	Rotary transformers are established for continuous rotating interfaces	Requires control of electric field, insulation and common-mode current
Voltage transformation	Available through winding turns ratio	No equivalent magnetic turns-ratio function
Converter integration	Directly compatible with the DAB arrangement used in this thesis	Requires a suitable high frequency excitation, compensation and receiving-side conversion stage

Coupler size alone is not sufficient to estimate transferred power or efficiency. For CPT, Equation (2.7) shows that coupling capacitance increases with effective plate area and decreases with plate separation. The resulting power transfer also depends on operating voltage, frequency, compensation, parasitic capacitance and converter losses. For IPT, increasing magnetic cross-section and winding area can increase the available magnetic and electrical loading, but the transferred power also depends on flux density, current density, coupling, leakage and magnetising inductance, operating frequency, losses and thermal limits. The dimensions reported for different WPT systems should therefore be considered together with their electrical operating conditions.

2.5.6 Selection of IPT for the X-ROTOR Interface

For the X-ROTOR rotor-to-tower interface, IPT is selected in the form of an annular rotary transformer. The rotating and stationary structures are approximately coaxial and separated by a short controlled clearance, allowing the magnetic core and winding dimensions to be chosen within the available annular installation space.

The RT provides galvanic isolation and allows voltage transformation through the winding turns ratio. It also interfaces directly with the DAB stage: the two active bridges generate the medium frequency excitation, their phase displacement controls transferred power, and the RT leakage inductance contributes to the effective transfer inductance[14][15][16][41][42][43][48].

CPT remains a possible contactless solution for rotating interfaces, as discussed in Sections 2.5.4 and 2.5.5. Its application to the present high power interface would require sufficient coupling capacitance to be maintained through the available electrode area and mechanical clearance, together with suitable insulation, plate-voltage control, electric-field management and protection against parasitic and common-mode currents. The rotating CPT system reported in [46] demonstrates the principle at a different rating and geometry.

For the X-ROTOR configuration considered here, the annular RT is carried forward because it matches the approximately coaxial rotating geometry, provides galvanic

isolation and turns-ratio voltage transformation, and can be incorporated directly into the phase-shift-controlled DAB stage.

2.5.7 High Power WPT and RT Studies

High power magnetic IPT has been reported for road-vehicle charging, public transport, railway and industrial applications, including successive developments of roadway-powered OLEV systems[49]-[52]. Table 2.8 compares selected systems in terms of coupler form, reported power, physical clearance, efficiency and operating frequency. The values are quoted according to the definitions used in the individual sources, since the reported power and efficiency do not always refer to the same system boundary.

The 50 kW/85 kHz ETH Zurich studies include the power electronic implementation, system optimisation and comparison of alternative coil geometries reported in [54]-[57]

Table 2.8 Selected High Power Magnetic IPT and Rotary transformer Studies

System/ source	Mechanism and coupler form	Reported power	Gap	Reported efficiency	Frequency
KAIST roadway system [50] [52]	IPT-track coupler	27 / 22 kW	200 mm	74 / 71%	20 kHz
WAVE bus charger [53]	IPT-discrete coil	50 kW	178 mm	92%	23.4 kHz
ETH Zurich prototype [54] [57]	IPT-discrete coil	50 kW	100 200 mm	95.8%	85 kHz
Fraunhofer prototype [58][59]	IPT-discrete coil	22 kW	135 mm	97%	100 kHz
KRRI railway system [60]	IPT-track coupler	818 kW total system basis	50 mm	82.7%	60 kHz
Showa Aircraft system [61]	IPT-discrete coil	30 kW	150 mm	92%	22 kHz
NYU prototype [62][63]	IPT-discrete coil	25 kW	210 mm	91%	85 kHz

Conductix Wampfler system [57]	IPT-discrete coil	120 kW total system basis	40 mm	90%	20 kHz
600 V/100 kW X-ROTOR RT study [64]	IPT-single-phase RT	100 kW	1 mm	98.8% design/FEM basis	2 kHz
1.8 kV/1 MW X-ROTOR RT-DAB study [48]	IPT-three RT phases with three-phase DAB	1 MW system	5 mm	96.3% simulated system	1 kHz
Toscani large-shaft rotary transformer [41]	IPT-coaxial rotary transformer	1-6 kW design/FEM range	1mm	not explicitly reported for this design point	20 kHz design condition
Botha-Gule three-phase rotary transformer prototype[65]	IPT-three-phase laminated axial-airgap RT	6 kVA prototype	0.6 mm	>95% measured	50Hz
Manko et al. rotary transformer literature comparison[66]	IPT-axial/radial RT topologies	20 W-11.3 kW across reported cases	0.5-1.5 mm	70-98%	5-520 kHz

All systems listed in Table 2.8 use magnetic IPT. The terms track coupler, discrete coil and rotary transformer identify different physical forms of the magnetic coupler. Reported power may refer either to one coupler or to a complete multi-pickup system, while efficiency may be quoted for the coupler, compensated transfer stage or complete converter system. The values are therefore retained in the form reported by the original sources.

The transport systems in Table 2.8 operate across clearances of several tens to hundreds of millimetres. Rotary transformer applications use much smaller magnetic airgaps. Toscani et al. considered a large-shaft coaxial RT with a 1 mm airgap[41]. Botha and Gule manufactured and tested a three-phase axial-airgap RT with an approximately 0.6 mm clearance and measured an efficiency above 95% under the reported full-load condition[65]. The review by Manko et al. includes several rotary transformer designs

with airgaps between approximately 0.5 and 1.5 mm[66]. These studies provide independent examples of millimetre-scale magnetic clearances in rotating power transfer interfaces.

The published X-ROTOR studies occupy a different power range from the independent RT examples. The 600 V/100 kW single-phase RT study uses a 1 mm magnetic airgap[64], while the published 1.8 kV/1 MW three-phase RT-DAB study uses a 5 mm magnetic airgap[48]. These studies belong to the same research programme as this thesis and are included to show the development of the X-ROTOR RT design, they are not treated as independent confirmation of the present results. The 5 mm value reported for the published 1 MW study refers to its magnetic airgap. In the later MW-class sensitivity study in Chapter 4, the topology-specific core gaps are retained while the 5, 10 and 15 mm controlled series refers to primary-to-secondary winding separation.

The data in Table 2.8 should not be scaled directly from coupler dimensions. As discussed in Section 2.5.5, IPT power capability also depends on magnetic loading, winding area, current density, coupling, frequency, losses and cooling. Table 2.8 is therefore used to compare reported operating points rather than to derive a size-to-power or size-to-efficiency relationship.

2.6 Discussion

The electrical arrangement considered in this chapter separates the two secondary generator channels before the rotating power transfer interface. Each PMSG is connected to its own active machine side converter, allowing its variable-frequency output to be regulated independently when the two secondary rotors operate at different instantaneous speeds and torques. Coordination is then carried out on the DC side, avoiding the need to synchronise the generator terminals directly.

For the generator side reference arrangement, the 3.3 kV option is retained together with an actively controlled three-level converter. At the same transferred power, the higher generator voltage reduces the current relative to the 690 V alternative and consequently reduces the required conductor current rating. This benefit is accompanied by the insulation, protection, switching and maintenance requirements

associated with medium voltage equipment. The comparison therefore supports the selected project arrangement without implying that a 3.3 kV generator is inherently lighter, more efficient or less costly in every design.

At the rotating interface, a slip ring remains an electrically feasible solution, but it retains the sliding contact wear and maintenance mechanisms discussed in Sections 1.3 and 2.5. Far-field transfer is not suited to the short rotating clearance considered here, while both IPT and CPT can operate without electrical contact. The comparison in Section 2.5 shows why an annular rotary transformer is selected for the present work: it is compatible with the approximately coaxial rotating geometry, provides galvanic isolation and turns-ratio voltage transformation, and can be connected directly between the two active bridges of the DAB stage.

The three investigations differ in scale and purpose. The reduced-scale platform provides the experimental evidence, 600 V/100 kW case examines the electromagnetic modelling procedure, and the 1.8 kV/1 MW model examines MW-class linked field-circuit operation. The two high power cases are therefore not inferred from the laboratory system by geometric or electrical scaling.

The system choices made in this chapter define the electrical arrangement but do not fix the final RT geometry or operating point. Core dimensions, winding arrangement, magnetic airgap, winding separation, turns ratio, leakage and magnetising inductance, flux density, current density, switching frequency and phase shift remain design variables. Leakage inductance must be considered together with the transfer-inductance requirement of the DAB rather than reduced independently. Chapter 3 develops the analytical RT and DAB relationships used to select these quantities and introduces the candidate RT geometries examined subsequently in Chapter 4.

2.7 Chapter Summary

This chapter defined the electrical arrangement required to transfer power from the two secondary generators of the X-ROTOR to the stationary tower. The two PMSG outputs are treated as independent electrical channels, each connected to an actively controlled machine side converter before coordination on the DC side. The 690 V and

3.3 kV generator alternatives and the applicable converter topologies are compared, with the 3.3 kV PMSG and three-level active converter retained as the reference generator side arrangement. The complete power path is then defined from the secondary rotor shaft to the stationary DC link and subsequent grid-side conversion.

The rotating power transfer interface is considered against both conductive and contactless alternatives. A slip ring provides the conventional electrical reference but retains sliding contact wear and maintenance requirements. Far-field transfer is not suited to the short rotor-to-tower clearance, while both IPT and CPT can provide near-field contactless transfer. For the X-ROTOR arrangement examined in this thesis, the rotary transformer form of IPT is retained because it is compatible with the annular rotating geometry, provides galvanic isolation and turns-ratio voltage transformation, and can be connected directly to the DAB converter stage. The high power WPT and rotary transformer studies reviewed in this chapter provide operating examples for comparison but are not used to derive a direct relationship between coupler size, transferred power and efficiency.

Chapter 3 develops the analytical design of the selected RT-DAB interface. It considers the magnetic dimensions, winding arrangement, magnetic airgap, winding separation, turns ratio, leakage and magnetising inductance, switching frequency and phase-shift control required for the RT and DAB to operate together. The resulting design quantities are then used in the numerical and experimental studies presented in Chapter 4.

2.8 Chapter References

[1]*W. Leithead, A. Camciuc, A. K. Amiri, and J. Carroll, "The X-ROTOR offshore wind turbine concept," Journal of Physics: Conference Series, vol. 1356, no. 1, p. 012031, 2019, doi: 10.1088/1742 6596/1356/1/012031.*

[2]*L. Morgan, W. Leithead, and J. Carroll, "On the use of secondary rotors for vertical axis wind turbine power take off," Wind Energy, vol. 27, no. 6, pp. 569-582, 2024.*

[3]*D. Campos Gaona, A. Stock, W. Leithead, and O. Anaya Lara, Secondary Rotors and Power Train Design, X-ROTOR Project Deliverable D5.1, University of Strathclyde, Glasgow, UK, Dec. 2021, Grant Agreement No. 101007135.*

[4]*S. A. Mortazavizadeh, R. Yazdanpanah, D. Campos Gaona, and O. Anaya Lara, Control System for the Power Electronics and Rotatory Transformer Arrangement, X-ROTOR Project Deliverable D5.3, University of Strathclyde, Glasgow, UK, Feb. 2024, Grant Agreement No. 101007135.*

[5]*V. Yaramasu and B. Wu, "Predictive control of a three-level boost converter and an NPC inverter for high power PMSG based medium voltage wind energy conversion systems," IEEE Transactions on Power Electronics, vol. 29, no. 10, pp. 5308-5322, 2014, doi: 10.1109/TPEL.2013.2292068.*

[6]*IEC 60038:2009, IEC Standard Voltages, International Electrotechnical Commission, Geneva, Switzerland, 2009.*

[7]*V. Yaramasu, B. Wu, P. C. Sen, S. Kouro, and M. Narimani, "High power wind energy conversion systems: State of the art and emerging technologies," Proceedings of the IEEE, vol. 103, no. 5, pp. 740-788, 2015, doi: 10.1109/JPROC.2014.2378692.*

[8]*B. Wu, Y. Lang, N. Zargari, and S. Kouro, Power Conversion and Control of Wind Energy Systems. Hoboken, NJ, USA: Wiley, 2011.*

[9]*W. Erdman and M. Behnke, Low Wind Speed Turbine Project Phase II: The Application of Medium Voltage Electrical Apparatus to the Class of Variable Speed Multi Megawatt Low Wind Speed Turbines. Golden, CO, USA: National Renewable Energy Laboratory, 2005.*

[10]*R. Erickson, S. Angkititrakul, O. Al Naseem, and G. Lujan, Novel Power Electronics Systems for Wind Energy Applications: Final Report. Golden, CO, USA: National Renewable Energy Laboratory, 2002.*

[11]*J. Rodriguez, S. Bernet, P. K. Steimer, and I. E. Lizama, "A survey on neutral point clamped inverters," IEEE Transactions on Industrial Electronics, vol. 57, no. 7, pp. 2219-2230, 2010, doi: 10.1109/TIE.2009.2032430.*

[12]*S. Kouro et al., "Recent advances and industrial applications of multilevel converters," IEEE Transactions on Industrial Electronics, vol. 57, no. 8, pp. 2553-2580, 2010, doi: 10.1109/TIE.2010.2049719.*

[13]*X. Yuanye, K. H. Ahmed, and B. W. Williams, "Different torque ripple reduction methods for wind energy conversion systems using a diode rectifier and boost converter," in Proc. IEEE International Electric Machines and Drives Conference, 2011, pp. 729-734, doi: 10.1109/IEMDC.2011.5994902.*

[14]*R. Yazdanpanah, S. Mortazavizadeh, D. Campos Gaona, and O. Anaya Lara, Scaled Rotatory Transformer Models, Design and Control, X-ROTOR Project Deliverable D5.2, University of Strathclyde, Glasgow, UK, Dec. 2022, Grant Agreement No. 101007135.*

[15]*Y. Cui, D. Wang, and A. Emadi, "Three-phase dual active bridge converter design considerations," in Proc. 43rd Annual Conference of the IEEE Industrial Electronics Society, 2017, pp. 4696-4701, doi: 10.1109/IECON.2017.8216809.*

[16]*R. T. Naayagi, A. J. Forsyth, and R. Shuttleworth, "High power bidirectional DCDC converter for aerospace applications," IEEE Transactions on Power Electronics, vol. 27, no. 11, pp. 4366-4379, 2012, doi: 10.1109/TPEL.2012.2184771.*

[17]*J. Carroll, A. McDonald, and D. McMillan, "Failure rate, repair time and unscheduled O&M cost analysis of offshore wind turbines," Wind Energy, vol. 19, no. 6, pp. 1107-1119, 2016.*

[18]*C. Flannigan, J. Carroll, and W. Leithead, "Operations expenditure modelling of the X-ROTOR offshore wind turbine concept," Journal of Physics: Conference Series, vol. 2265, no. 3, p. 032054, 2022, doi: 10.1088/1742 6596/2265/3/032054.*

[19]*J. McMorland et al., "A review of operations and maintenance modelling with considerations for novel wind turbine concepts," Renewable and Sustainable Energy Reviews, vol. 165, p. 112581, 2022, doi: 10.1016/j.rser.2022.112581.*

[20]*R. D. Hall and R. P. Roberge, "Carbon brush performance on slip rings," in Proc. Annual Pulp and Paper Industry Technical Conference, 2010, pp. 1-6, doi: 10.1109/PAPCON.2010.5556522.*

[21]*J. K. Skjølberg, H. F. Ohma, and M. Runde, "Wear rates and current distribution of carbon brushes on steel slip rings," IEEE Transactions on Energy Conversion, vol. 24, no. 4, pp. 835-840, 2009, doi: 10.1109/TEC.2009.2025416.*

[22]*W. Würfel and W. Hofmann, "Monitoring of the transmission properties of the rotor slip ring system of doubly fed induction generators," in Proc. IEEE International*

Conference on Electric Machines and Drives, 2005, pp. 295-299, doi: 10.1109/IEMDC.2005.195737.

[23]*S. J. van Heerden and H. J. Vermeulen, "Model based condition monitoring of a doubly fed induction generator slip ring component," in Proc. 48th International Universities' Power Engineering Conference, 2013, pp. 1-6, doi: 10.1109/UPEC.2013.6714965.*

[24]*T. H. Houenouvo and W. Hofmann, "Diagnostics of the transmission properties of the slip ring system in doubly fed induction generators," in Proc. IEEE 60th Holm Conference on Electrical Contacts, 2014, pp. 1-7, doi: 10.1109/HOLM.2014.7031019.*

[25]*K. Kate singnoy and S. Premrudeepreechacharn, "Age estimation of an electrographite brush in a generator system for optimised maintenance planning of Sirikit hydropower plant," in Proc. North American Power Symposium, 2014, pp. 1-6, doi: 10.1109/NAPS.2014.6965393.*

[26]*K. Fukuda, K. Sawa, and T. Ueno, "Relationship between brush current change and contact voltage drop in sliding contact with a steel slip ring and various silver-graphite brushes," in Proc. IEEE 66th Holm Conference on Electrical Contacts, 2020, pp. 105-109, doi: 10.1109/HLM49214.2020.9307888.*

[27]*G. Dorsey, "High reliability slip ring design for wind turbines," Moog Inc., white paper. [Online]. Available: https://www.moog.com/content/dam/moog/literature/products/slip rings/wind turbine slip rings/Moog High Reliability Slip Ring Design for Wind Turbines White Paper.pdf*

[28]*K. Detka and K. Górecki, "Wireless power transfer-A review," Energies, vol. 15, no. 19, p. 7236, 2022, doi: 10.3390/en15197236.*

[29]*A. M. Jawad, R. Nordin, S. K. Gharghan, H. M. Jawad, and M. Ismail, "Opportunities and challenges for near field wireless power transfer: A review," Energies, vol. 10, no. 7, p. 1022, 2017, doi: 10.3390/en10071022.*

[30]*N. Shinohara, Wireless Power Transfer via Radiowaves. Hoboken, NJ, USA: Wiley, 2014.*

[31]*A. Massa, G. Oliveri, F. Viani, and P. Rocca, "Array designs for long distance wireless power transmission: State of the art and innovative solutions," Proceedings of the IEEE, vol. 101, no. 6, pp. 1464-1481, 2013.*

[32]*M. Aboualalaa, H. Elsadek, and R. K. Pokharel, "Wireless power transfer: Recent techniques for improving system efficiency," in Wireless Power Transfer-Recent Development, Applications and New Perspectives. London, UK: IntechOpen, 2021.*

[33]*W. Yan and J. Chen, "A general design of a magnetic coupling resonant wireless power transmission circuit," IOP Conference Series: Earth and Environmental Science, vol. 69, no. 1, p. 012197, 2017.*

[34]*C. S. Wang, G. A. Covic, and O. H. Stielau, "Power transfer capability and bifurcation phenomena of loosely coupled inductive power transfer systems," IEEE Transactions on Industrial Electronics, vol. 51, no. 1, pp. 148-157, 2004, doi: 10.1109/TIE.2003.822038.*

[35]*X. Mou, D. T. Gladwin, R. Zhao, and H. Sun, "Survey on magnetic resonant coupling wireless power transfer technology for electric vehicle charging," IET Power Electronics, vol. 12, no. 12, pp. 3005-3020, 2019.*

[36]*H. Hong, D. Yang, and S. Won, "Analysis for selecting compensating capacitances of a two coil resonant wireless power transfer system," in Proc. IEEE International Conference on Energy Internet, 2017, pp. 220-225.*

[37]*Y. Zhang, Z. Yan, Z. Liang, S. Li, and C. C. Mi, "An LCL N compensated strongly coupled wireless power transfer system for high power applications," in Proc. IEEE Applied Power Electronics Conference and Exposition, 2019, pp. 3088-3091.*

[38]*A. Rakhymbay, M. Bagheri, and M. Lu, "A simulation study on four different compensation topologies in EV wireless charging," in Proc. International Conference on Sustainable Energy Engineering and Application, 2017, pp. 66-73.*

[39]*K. Aditya and S. S. Williamson, "Design considerations for a loosely coupled inductive power transfer system for electric vehicle battery charging: A comprehensive review," in Proc. IEEE Transportation Electrification Conference and Expo, 2014, pp. 1-6.*

[40]*Y. H. Sohn, B. H. Choi, E. S. Lee, G. C. Lim, G. H. Cho, and C. T. Rim, "General unified analyses of two capacitor inductive power transfer systems: Equivalence of current source SS and SP compensations," IEEE Transactions on Power Electronics, vol. 30, no. 11, pp. 6030-6045, 2015, doi: 10.1109/TPEL.2015.2409734.*

[41]*N. Toscani, M. Brunetti, M. S. Carmeli, F. Castelli Dezza, and M. Mauri, "Design of a rotary transformer for installations on large shafts," Applied Sciences, vol. 12, no. 6, p. 2932, 2022, doi: 10.3390/app12062932.*

[42]*Y. Zhang, J. Yang, D. Jiang, D. Li, and R. Qu, "Design, manufacture, and test of a rotary transformer for a contactless power transfer system," IEEE Transactions on Magnetics, vol. 58, no. 2, pp. 1-6, 2022, doi: 10.1109/TMAG.2021.3094135.*

[43]*M. N. Kheraluwala, R. W. Gascoigne, D. M. Divan, and E. D. Baumann, "Performance characterisation of a high power dual active bridge DCto-DC converter," IEEE Transactions on Industry Applications, vol. 28, no. 6, pp. 1294-1301, 1992, doi: 10.1109/28.175280.*

[44]*F. Lu, H. Zhang, and C. C. Mi, "A review on the recent development of capacitive wireless power transfer technology," Energies, vol. 10, no. 11, p. 1752, 2017, doi: 10.3390/en10111752.*

[45]*C. Liu, A. P. Hu, and N. K. C. Nair, "Coupling study of a rotary capacitive power transfer system," in Proc. IEEE International Conference on Industrial Technology, 2009, pp. 1-6.*

[46]*S. Ahmad, A. Muharam, and R. Hattori, "Rotary capacitive power transfer with a Class E inverter and balun circuit," in Proc. IEEE PELS Workshop on Emerging Technologies: Wireless Power Transfer, 2020, pp. 330-333.*

[47]*D. C. Ludois, K. Hanson, and J. K. Reed, "Capacitive power transfer for slip ring replacement in wound field synchronous machines," in Proc. IEEE Energy Conversion Congress and Exposition, 2011, pp. 1664-1669.*

[48]*R. Yazdanpanah, S. A. Mortazavizadeh, Y. Teng, O. Anaya Lara, and D. Campos Gaona, "An integrated rotary transformer and three-phase dual active bridge converter for high power transfer in novel X-ROTOR wind turbines," in Proc. IEEE International Magnetics Conference, Sendai, Japan, 2023, pp. 1-5, doi: 10.1109/INTERMAG50591.2023.10265091.*

[49]*S. Y. Choi and C. T. Rim, "Recent progress in developments of online electric vehicles," in Proc. 6th International Conference on Power Electronics Systems and Applications, 2015, pp. 1-8.*

[50]*C. C. Mi, G. Buja, S. Y. Choi, and C. T. Rim, "Modern advances in wireless power transfer systems for roadway poared electric vehicles," IEEE Transactions on Industrial Electronics, vol. 63, no. 10, pp. 6533-6545, 2016, doi: 10.1109/TIE.2016.2574993.*

[51]*S. Y. Choi, S. Y. Jeong, B. W. Gu, G. C. Lim, and C. T. Rim, "Ultraslim S type power supply rails for roadway poared electric vehicles," IEEE Transactions on Power Electronics, vol. 30, no. 11, pp. 6456-6468, 2015, doi: 10.1109/TPEL.2015.2444894.*

[52]*S. Y. Choi, B. W. Gu, S. Y. Jeong, and C. T. Rim, "Advances in wireless power transfer systems for roadway poared electric vehicles," IEEE Journal of Emerging and Selected Topics in Power Electronics, vol. 3, no. 1, pp. 18-36, 2015, doi: 10.1109/JESTPE.2014.2343674.*

[53]*H. H. Wu and M. P. Masquelier, "An overview of a 50-kW inductive charging system for electric buses," in Proc. IEEE Transportation Electrification Conference and Expo, 2015, pp. 1-4, doi: 10.1109/ITEC.2015.7165747.*

[54]*R. Bosshard and J. W. Kolar, "All SiC 9.5 kW/dm3 onboard power electronics for a 50 kW/85 kHz automotive IPT system," IEEE Journal of Emerging and Selected Topics in Power Electronics, vol. 5, no. 1, pp. 419-431, 2017, doi: 10.1109/JESTPE.2016.2624285.*

[55]*R. Bosshard and J. W. Kolar, "Multi objective optimisation of a 50 kW/85 kHz IPT system for public transport," IEEE Journal of Emerging and Selected Topics in Power Electronics, vol. 4, no. 4, pp. 1370-1382, 2016, doi: 10.1109/JESTPE.2016.2598755.*

[56]*R. Bosshard, U. Iruretagoyena, and J. W. Kolar, "Comprehensive evaluation of rectangular and double D coil geometry for a 50 kW/85 kHz IPT system," IEEE Journal of Emerging and Selected Topics in Power Electronics, vol. 4, no. 4, pp. 1406-1415, 2016, doi: 10.1109/JESTPE.2016.2600162.*

[57]*R. Bosshard, Multi Objective Optimization of Inductive Power Transfer Systems for EV Charging, doctoral dissertation, ETH Zurich, Zurich, Switzerland, 2015.*

[58]*B. Goeldi, J. Tritschler, and S. Reichert, "Measurement results of a 22-kW bidirectional inductive charger," in Proc. PCIM Europe, 2015, pp. 1-8.*

[59]*J. Tritschler, S. Reichert, and B. Goeldi, "A practical investigation of a high power bidirectional charging system for electric vehicles," in Proc. 16th European Conference on Power Electronics and Applications, 2014, pp. 1-7, doi: 10.1109/EPE.2014.6910809.*

[60]*J. H. Kim et al., "Development of a 1 MW inductive power transfer system for a high speed train," IEEE Transactions on Industrial Electronics, vol. 62, no. 10, pp. 6242-6250, 2015, doi: 10.1109/TIE.2015.2417122.*

[61]*N. Shinohara, "Wireless power transmission progress for electric vehicles in Japan," in Proc. IEEE Radio and Wireless Symposium, 2013, pp. 109-111, doi: 10.1109/RWS.2013.6486657.*

[62]*M. Bojarski, E. Asa, K. Colak, and D. Czarkowski, "Analysis and control of a multiphase inductively coupled resonant converter for wireless electric vehicle charger applications," IEEE Transactions on Transportation Electrification, vol. 3, no. 2, pp. 312-320, 2017, doi: 10.1109/TTE.2016.2566921.*

[63]*M. Bojarski, E. Asa, K. Colak, and D. Czarkowski, "A 25 kW industrial prototype wireless electric vehicle charger," in Proc. IEEE Applied Power Electronics Conference and Exposition, 2016, pp. 1756-1761, doi: 10.1109/APEC.2016.7468105.*

[64]*Y. Teng, O. Anaya Lara, R. Yazdanpanah, D. Campos Gaona, and S. A. Mortazavizadeh, "Design and analysis of a 100-kW rotary transformer for X-ROTOR wind generators," in Proc. IEEE Workshop on Electrical Machines Design, Control and Diagnosis, Newcastle upon Tyne, UK, 2023, pp. 1-5.*

[65]*S. Botha and N. Gule, "Design and evaluation of a laminated three-phase rotary transformer for DFIG applications," Energies, vol. 15, no. 11, Art. no. 4061, 2022, doi: 10.3390/en15114061.*

[66]*R. Manko, S. Čorović, and D. Miljavec, "Analysis and design of rotary transformer for wireless power transmission," in Proc. 2020 IEEE Problems of Automated Electrodrive: Theory and Practice (PAEP), 2020, pp. 1-6, doi: 10.1109/PAEP49887.2020.9240870.*

Chapter 3

3 Design Methodology for RT-DAB Interface

3.1 Introduction

Chapter 2 established the electrical architecture of the X-ROTOR powertrain and selected an inductive rotary transformer (RT) for the rotor-to-tower contactless power transfer interface. The present chapter develops the RT and dual active bridge (DAB) design required for the subsequent numerical and experimental studies.

The RT is first sized from the electrical and magnetic requirements of the transfer stage. The analytical relationships relate winding voltage and frequency to magnetic flux, winding turns and effective core area, and relate winding current to conductor area, current density and winding window utilisation. Magnetic reluctance, mean conductor length and first-order winding loss are then introduced to complete the initial sizing calculation. The core-to-core magnetic airgap, primary-to-secondary winding separation and winding-to-core clearances are treated as separate geometrical quantities because they affect the magnetic path and winding arrangement in different ways.

The analytical design is applied to five RT geometries: the original radial type, NEW1, NEW2, L-type 1 and L-type 2. The radial structure provides the reference geometry, while NEW1 and NEW2 are developed in this thesis for the X-ROTOR design space. The geometries differ in magnetic return path, winding window arrangement, conductor placement and installation access. These differences also affect leakage, magnetising behaviour and winding length, and are examined quantitatively in Chapter 4.

Section 3.3 considers the DAB converter. The single-phase arrangement is used to define the bridge-voltage waveforms, RT turns ratio, effective transfer inductance and phase-shift-controlled power relationship. The same notation is then carried into the three-phase arrangement used for the MW-class linked field-circuit model. The RT leakage inductance forms part of the effective transfer inductance seen by the converter, while the bridge voltages, switching frequency and phase shift determine the current imposed on the RT. The magnetic and converter quantities must therefore be selected together.

The three investigation levels used later in the thesis are also distinguished in this chapter. The reduced-scale system provides the experimental RT-DAB platform, the 600 V/100 kW case is used for analytical and electromagnetic model comparison, and the 1.8 kV/1 MW three-phase model is used for MW-class linked field-circuit evaluation. They have different electrical and modelling boundaries and are not obtained from one another by direct scaling.

Section 3.4 brings the RT and DAB calculations together in the design procedure used to generate the parameter sets examined in Chapter 4. Local field distribution, geometry-dependent leakage, magnetic non-linearity and converter-coupled operating behaviour are then obtained from the numerical models rather than inferred from the analytical equations alone.

3.2 Analytical Design of Rotary Transformer

The RT design begins with the electrical, magnetic and geometrical quantities required to define a feasible transformer geometry before finite-element analysis. The initial calculation determines the winding turns, conductor area, winding window dimensions, effective core area and the magnetic clearances used in the subsequent candidate designs.

A rotary transformer operates according to the same electromagnetic induction principle as a conventional transformer, but the primary and secondary magnetic structures remain mechanically separated to permit continuous relative rotation. The resulting airgap increases the magnetic reluctance and affects magnetising current,

leakage and coupling. Core geometry and winding arrangement must therefore be included in the initial design rather than treated as secondary geometrical details[1][2][3]. Three clearances are distinguished in the analysis. The core-to-core magnetic airgap is denoted by g_c, the primary-to-secondary winding separation by δ_w, and the primary- and secondary-side winding-to-core clearances by c_p and c_s, respectively. The magnetic airgap forms part of the principal magnetic path, whereas winding separation and winding-to-core clearance mainly determine conductor placement and the available leakage paths. These dimensions are therefore retained as separate variables throughout Chapters 3 and 4.

3.2.1 Fundamental Analytical Design Equations

The initial RT dimensions are obtained from Faraday's law, conductor current density, winding window utilisation and the magnetic-circuit relationships. These equations provide first-order dimensions for the analytical design, local fringing, flux crowding, magnetic non-linearity and topology-dependent leakage are subsequently obtained from the FEM models. Frequency-dependent conductor and magnetic effects must also be considered at medium frequency operation[4][5][6]..

For periodic excitation, the RMS voltage of an N turn winding is written in waveform general form as

$$V_{rms} = k_v f_s N \Phi_{pk} \tag{3.1}$$

where V_{rms} is the RMS winding voltage, is the number of turns, fis the excitation frequency, Φ_{pk} is the peak linked magnetic flux, and $\mathrm{k_v}$ is the voltage-waveform coefficient. For sinusoidal excitation $k_v = 4.44$, whereas an ideal symmetrical square-wave excitation gives $k_v = 4.0$.

The linked flux may be written locally as

$$\Phi_{pk} \approx B_c A_c \approx B_g A_{g,\mathrm{eff}} \tag{3.2}$$

where B_c and B_g are the representative core and airgap flux densities. The corresponding areas A_c and $A_{g,\mathrm{eff}}$ are defined normal to the local principal flux direction. $A_{g,\mathrm{eff}}$ includes the first-order fringing allowance used in the analytical model. This local

definition is used throughout the reluctance calculation and when interpreting the axisymmetric FEM results[17].

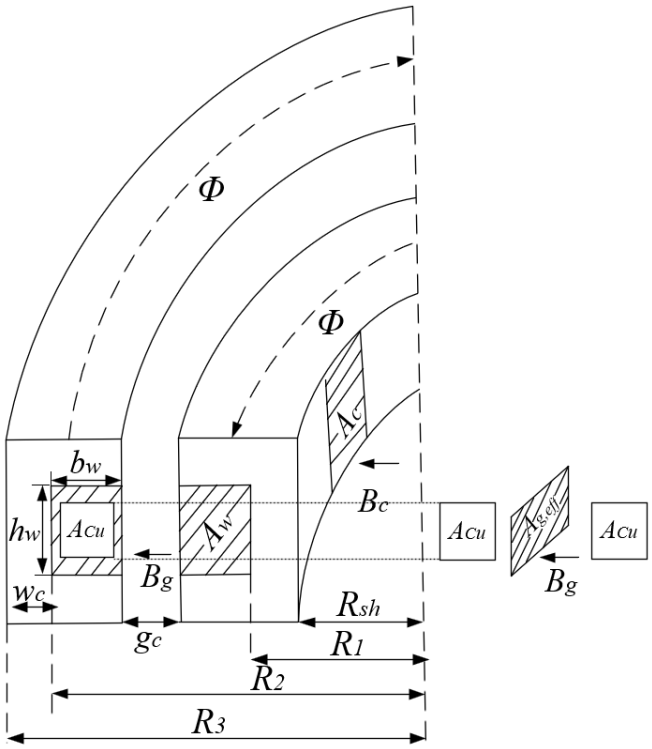


Figure 3.1 Meridional section of the baseline single-phase radial RT showing the principal magnetic-flux path and local cross-sectional quantities

Figure 3.1 shows the meridional section of the baseline radial-flux RT used for the analytical model. The principal magnetic-flux path Φ crosses the core-to-core airgap and returns through the annular core. The indicated core and airgap areas represent local cross-sections normal to the principal magnetic-flux direction.

For preliminary winding sizing, the conductor current density is:

$$J = \frac{I_{rms}}{a_{\mathrm{Cu}}} \tag{3.3}$$

where J is the RMS current density,I_{rms} is the RMS winding current and a_{Cu} is the effective copper area of one turn.

For the initial single-phase sizing case, the winding current may be estimated from

$$I_m \approx \frac{P_{trans}}{V_{rms}} \tag{3.4}$$

where P_{trans} is the required transferred active power at the specified design boundary. This expression gives the current required for initial sizing. The current

produced by the DAB contains switching-frequency and circulating components and is obtained from the linked circuit model for the final operating points.

When both windings occupy the available window, the required total winding window area is

$$A_w = \frac{1}{k_f}\left(\frac{N_p I_{p,\mathrm{rms}}}{J_p} + \frac{N_s I_{s,\mathrm{rms}}}{J_s}\right) \tag{3.5}$$

where N_p and N_s are the primary and secondary turns, $I_{p,\mathrm{rms}}$ and $I_{s,\mathrm{rms}}$ are the corresponding RMS currents, J_p and J_s are the allowable current densities, and k_f denotes the fraction of the available winding window occupied by effective conductor after allowance for insulation, spacing and packing.

Equation (3.4) is used when the window is being sized. For prescribed turns, currents and current densities, a lower k_f requires a larger winding window. In the fixed-window study of Chapter 4, the window dimensions are instead held constant and the effective copper occupation is varied according to

$$A_{\mathrm{Cu}} = k_f A_w = N_p a_{\mathrm{Cu},p} + N_s a_{\mathrm{Cu},s} \tag{3.6}$$

This distinction is maintained in Chapter 4: the topology-specific winding window remains fixed while k_f changes the represented copper area.

For the rectangular equivalent winding window used in the initial radial design, the aspect ratio is defined as

$$a = \frac{h_w}{b_w} \tag{3.7}$$

where h_w and b_w are the window length and width, respectively. The required width is therefore

$$b_w = \sqrt{\frac{A_w}{a}} \tag{3.8}$$

and the corresponding window length is

$$h_w = \frac{A_w}{b_w} \tag{3.9}$$

For an equivalent circular conductor, the diameter is

$$d_{Cu} = 2\sqrt{\frac{a_{Cu}}{\pi}} \tag{3.10}$$

Equation (3.9) defines an equivalent conductor area for initial sizing. A practical high frequency winding requires separate specification of strand diameter, strand number, insulation and packing. These quantities determine the additional AC resistance associated with skin and proximity effects[4].

For the annular radial-flux reference, the required core area is related to the shaft radius and local core width by

$$w_c = \frac{A_c}{2\pi R_{\mathrm{sh}}} \tag{3.11}$$

where w_c is the required core width and R_{sh} is the reference shaft radius. Equation (3.11) applies to the radial reference geometry, the corresponding active section is defined separately for each candidate topology.

The DC resistance and first-order copper loss of one winding are

$$P_{\mathrm{cu}} = I_{\mathrm{rms}}^2 R_{\mathrm{cu}} = \frac{\rho_c N l_{\mathrm{mean}} I_{\mathrm{rms}}^2}{S_w} \tag{3.12}$$

where ρ_c is the conductor resistivity, R_{cu} is the winding DC resistance and l_{mean} is the mean conductor length per turn. For the baseline annular winding

$$l_{\mathrm{mean}} = 2\pi\left(R_1 + \frac{b_w}{2}\right) \tag{3.13}$$

The symbol l_{mean} is used throughout the thesis for mean turn length. The analytical loss represents the resistive conductor loss obtained from the mean conductor length and equivalent conductor area. In the Chapter 4 Maxwell models, Stranded Loss represents the corresponding winding-loss component under the stranded-conductor assumption. Strand-level skin and proximity effects are not resolved by that model.

For a magnetic path divided into core and airgap sections, the total reluctance is

$$\mathcal{R}_{tot} \approx \sum_k \frac{\ell_{c,k}}{\mu_0 \mu_{r,k} A_{\perp,k}} + \sum_j \frac{g_j}{\mu_0 A_{g,eff,j}}, \qquad \Phi = \frac{N I_{mag}}{\mathcal{R}_{tot}}, \qquad B_{g,j} = \frac{\Phi}{A_{g,eff,j}} \tag{3.14}$$

Here, k and j index core and airgap sections, $\ell_{c,k}$ is the local path length, μ_0 is the permeability of free space, $\mu_{r,k}$ is the local relative permeability, and I_{mag} is the equivalent magnetising current. Each $A_{\perp,k}$ and $A_{g,\mathrm{eff},j}$ is normal to the local principal flux. A common analytical framework does not imply that the five candidate geometries have the same reluctance. Their path lengths, section areas, gap positions and winding windows are topology specific.

When the magnetic reluctance is dominated by one effective airgap of total length g_{eff}, and fringing and core reluctance are neglected, the approximate airgap flux density becomes

$$B_g \approx \frac{\mu_0 N I_{\text{mag}}}{g_c} \tag{3.15}$$

Equation (3.14) shows directly that B_g is determined by the applied MMF and magnetic gap. For fixed NI,

$$g_{\text{eff}} \uparrow \Longrightarrow B_g \downarrow \tag{3.16}$$

Conversely, maintaining the same target B_g as the magnetic gap increases requires a larger MMF:

$$NI \propto B_g g_{\text{eff}} \tag{3.17}$$

The winding turns are therefore selected after the target flux density and winding current have been established, together with the voltage-frequency-flux relationship in Equation (3.1).

These relationships provide the initial winding, window and magnetic dimensions used to construct the candidate RT geometries. The analytical model gives the expected dependence on voltage, frequency, current density, copper occupation and magnetic gap. The resulting local flux distribution, leakage, coupling and magnetic non-linearity are examined using the FEM models in Chapter 4.

3.2.2 Candidate RT Geometries

The radial C-type RT provides the reference geometry for the analytical model in Section 3.2.1. For the X-ROTOR interface, however, the winding window and magnetic return path must also fit the available annular installation region and permit practical winding, insulation and assembly. Changes in core and winding geometry alter the magnetic path length, leakage path, available conductor area and mean turn length, and can therefore change both magnetic and electrical behaviour.

Rotary transformer studies in the literature use different radial, axial and enclosed magnetic arrangements to accommodate shaft dimensions, winding placement and

construction requirements[7]-[9],[17]-[25]. On this basis, five geometries are considered here: the original radial type, NEW1, NEW2, L-type 1 and L-type 2. NEW1 and NEW2 are developed in this thesis for the X-ROTOR design space, while the radial and L-type structures provide comparison geometries with different winding window and magnetic-return-path arrangements.

Figure 3.2 shows the meridional core and winding sections of the four alternative geometries. The winding regions are shown together with the steel sections so that their positions within each magnetic window are explicit. These are geometrical sections used to define the analytical and axisymmetric models, they are not magnetic flux-density plots.

The original radial type retains a regular annular magnetic path and enclosed winding window. Its geometry corresponds directly to the analytical radial-flux model and is therefore used as the baseline for comparison. The enclosed C-type window limits the directions available for winding placement and coil insertion.

NEW1 uses an asymmetric half-hat window. The unequal upper and lower regions allow the winding and magnetic return area to be redistributed where the available radial and axial installation space is not symmetric. The changed return path and conductor position also alter the mean conductor length, leakage path and local magnetic loading.

NEW2 extends this arrangement by enclosing a larger part of the winding region within the magnetic core. This produces a different magnetic return path and reduces the exposed winding region, while providing a more compact core-winding package. The more enclosed structure places greater constraints on coil insertion, insulation access and assembly.

The two L-type structures use more open winding regions. Their principal advantage is the additional access available for coil manufacture, insulation and cooling, together with greater freedom in radial or axial winding placement. The open magnetic structure also changes the leakage path and local flux distribution, so the electromagnetic consequences are assessed separately for the two orientations.

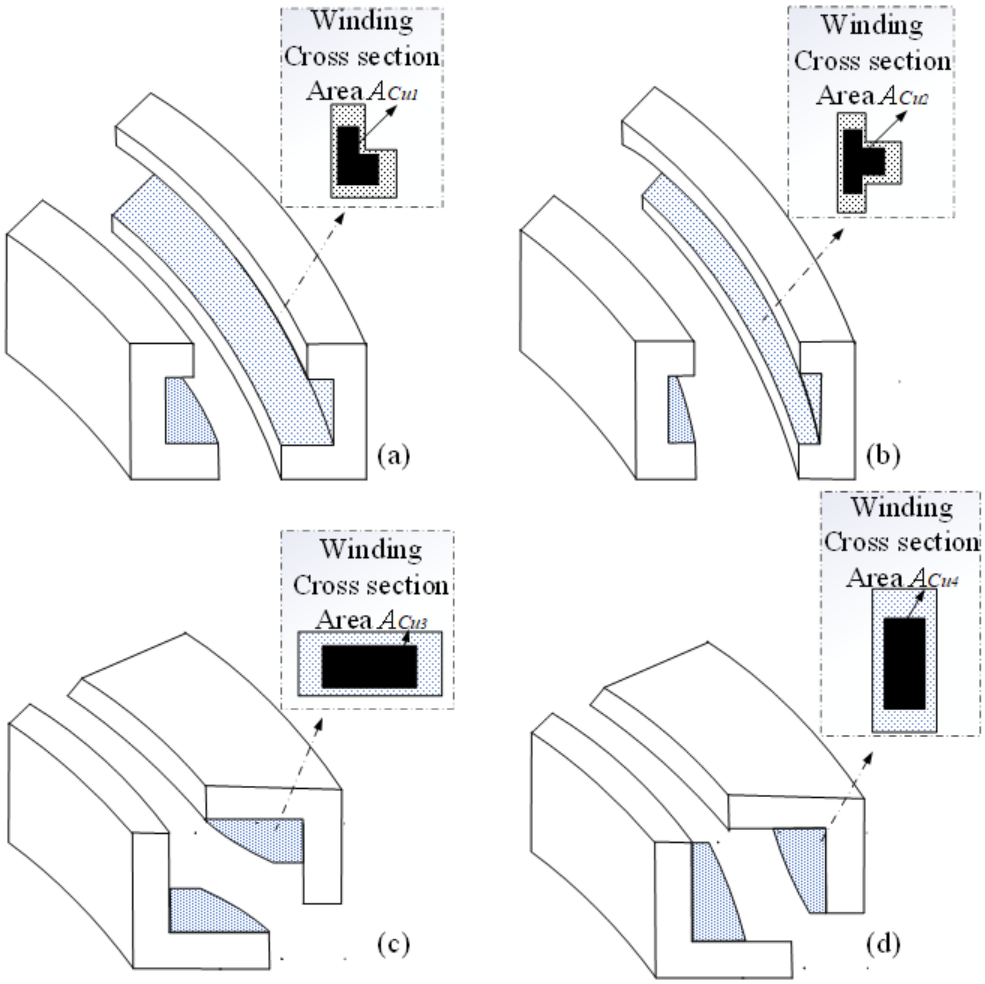


Figure 3.2 Core and winding geometries of the rotary transformers (a) Half hat type (NEW1) (b) Full hat type (NEW2) (c) L-type 1[3] (d) L-type 2

L-type 1 and L-type 2 provide more open winding arrangements and redistribute part of the winding cross section relative to the radial direction. They are therefore relevant where winding accessibility, radial/axial packaging flexibility or direct thermal access is prioritized. A removable or separately wound coil may be easier to place around an open limb than inside a more enclosed C type window, although the actual manufacturing route remains design specific. Their more open magnetic arrangement can alter the leakage path, require core cross section and local flux distribution and therefore require a different compromise between electromagnetic performance and practical installation.

Table 3.1 summarises the principal geometrical, magnetic and practical characteristics of the five candidate RT structures. Their electromagnetic performance is evaluated in Chapter 4.

Table 3.1 Qualitative design considerations for the candidate RT geometries

Geometry	Geometrical feature	Magnetic and winding effect	Practical consideration
Original radial	Regular annular C-type path and enclosed window	Provides the radial-flux reference geometry and an enclosed winding arrangement	Coil insertion and winding access are constrained by the enclosed window
NEW1	Asymmetric half-hat window	Produces unequal magnetic return paths and redistributes the available winding region	Allows the winding and core sections to be redistributed where radial and axial space differ
NEW2	More enclosed full-hat structure	Encloses a larger part of the winding within the magnetic return path	The more enclosed winding region reduces direct access for winding and insulation
L-type 1	Open L-shaped winding region	Changes the winding position and magnetic return path relative to the radial reference	Provides direct access to the winding and insulation from the open side
L-type 2	Alternative L-shaped orientation	Changes the winding position, mean turn length and magnetic path relative to L-type 1	Provides a second winding and installation orientation

The five candidates are implemented with comparable, although not identical, active winding and core sections, as listed in Table 3.2. The values are given separately because each geometry has its own winding window and magnetic return path.

Table 3.2 Winding and core cross-sectional areas of the five RT geometries

Geometry	Winding section (mm^2)	Core section (mm^2)
Original radial	8494	12008
NEW1	8665	11670
NEW2	8718	12106
L-type 1	8494	11747
L-type 2	8494	11751

The geometries therefore represent complete RT candidates rather than a core-shape-only comparison. Differences in Chapter 4 can arise from the combined effects of core shape, winding position, magnetic path, leakage and the small differences in

active section listed in Table 3.2. Active material mass is obtained from the complete model volume and material density rather than from these sectional values alone.

The numerical comparison consequently considers transferred power, winding current, coupling, leakage and magnetising behaviour, flux distribution and loss together. A candidate carrying less current may also transfer less power, so absolute loss alone is not used to rank the five structures.

3.2.3 Half-Hat Type (NEW1)

NEW1 introduces an asymmetric winding window and return path relative to the radial reference. Figure 3.3 identifies the upper and lower core-to-core gaps as $g_{c,\mathrm{up}}$ and $g_{c,\mathrm{down}}$. Both are magnetic clearances and are distinct from the primary-to-secondary winding separation δ_w.

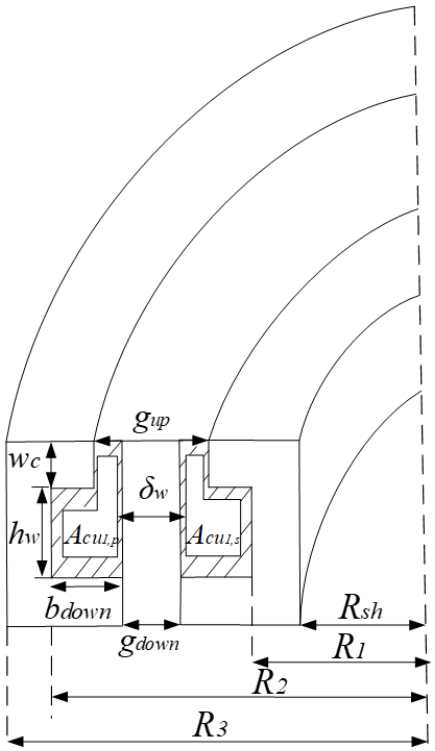


Figure 3.3 Half-hat (NEW1) type rotary transformer geometry

When the two airgap sections dominate the core reluctance and fringing is neglected, their combined reluctance is approximated by

$$\mathcal{R}_g \approx \frac{g_{c,\mathrm{up}} + g_{c,\mathrm{down}}}{\mu_0 A_g} \tag{3.18}$$

The corresponding airgap flux density is

$$B_g \approx \frac{\mu_0 N I_{\text{mag}}}{g_{c,\text{up}} + g_{c,\text{down}}} \tag{3.19}$$

where I_{mag} is the equivalent magnetising current producing the principal flux. For fixed NI_{mag}, increasing either core gap increases the total reluctance and lowers B_g. If a specified B_g is to be maintained, the required ampere turns are:

$$NI_{\text{mag}} \approx \frac{B_g^*\left(g_{c,\text{up}} + g_{c,\text{down}}\right)}{\mu_0} \tag{3.20}$$

Equation (3.20) is used as an ampere-turn requirement together with Equation (3.1), the selected winding current and the converter operating conditions.

The asymmetric window is parameterised using the lower width b_{down}, upper width b_{up}, length h_w and dimensionless aspect parameter γ:

$$h_w = \gamma b_{\text{down}} \tag{3.21}$$

For the idealised geometry in Figure 3.3, the lower width is

$$b_{\text{down}} = \sqrt{\frac{A_w - \left[\left(g_{c,\text{up}} - g_{c,\text{down}}\right)/2\right]w}{\gamma}} \tag{3.22}$$

The corresponding upper side window width is

$$b_{\text{up}} = b_{\text{down}} - \frac{g_{c,\text{up}} - g_{c,\text{down}}}{2} \tag{3.23}$$

The gap asymmetry is described by

$$k_1 = \frac{g_{c,\text{up}}}{g_{c,\text{down}}} \tag{3.24}$$

This ratio is a geometrical descriptor, it does not imply a linear electromagnetic response. Local flux density, leakage and magnetising behaviour are obtained from FEM. The first-order mean turn length is

$$l_{\text{mean,NEW1}} = 2\pi\left(R_1 + \frac{b_{\text{down}}}{2}\right) \tag{3.25}$$

This expression provides the first order conductor length required for winding resistance and copper loss calculation. The actual conductor path may differ locally

because of the asymmetric window arrangement and is therefore represented explicitly in the detailed numerical geometry.

The asymmetric window provides additional freedom in the placement of the winding and core return path. Its effect on leakage, local flux density and winding loss is examined with the other candidate geometries in Chapter 4.

3.2.4 Full-Hat Type (NEW2)

NEW2 extends the modified radial geometry by enclosing a larger part of the winding region within the magnetic return path. The winding window is described by the common width and length shown in Figure 3.4. Compared with NEW1, the geometry provides a more enclosed core-winding arrangement but reduces direct access to the winding during insulation and assembly.

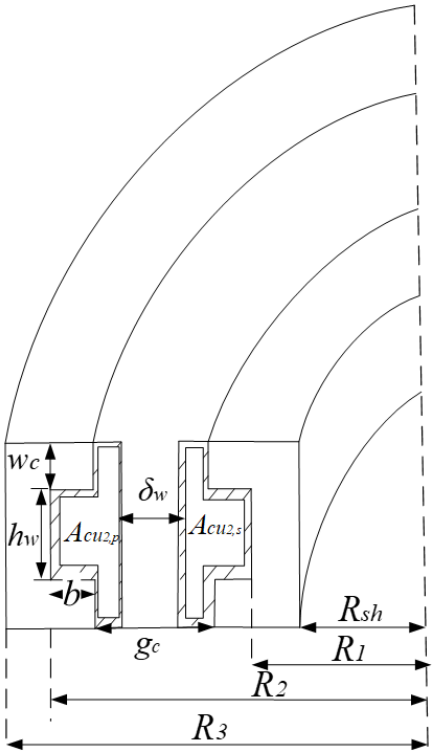


Figure 3.4 Full-hat (NEW2) type rotary transformer geometry

For the idealised NEW2 magnetic path, the two principal core gaps are equal. Equation (3.19), therefore reduces to

$$B_g \approx \frac{\mu_0 N I_{\text{mag}}}{2 g_c} \tag{3.26}$$

For the symmetric case, as for NEW1, B_g is determined by the applied ampere turns and total magnetic gap, the winding turns are subsequently coordinated with Equation (3.1).

Compared with the half hat and original radial types, the full hat structure offers a more compact magnetic path and allows more winding area to be enclosed by the core, which can be advantageous for improving magnetic performance and structural compactness.

The NEW2 winding window is defined using the window length h_w, width b and aspect ratio parameter β:

$$h_w = \beta b_w \tag{3.27}$$

where β is the ratio between the winding window length and width. Retaining the original geometrical formulation, the required window width is

$$b_w = -\frac{g_c - \delta_w}{4} + \frac{\sqrt{[(g_c - \delta_w)\beta]^2 - 4\beta[w(g_c - \delta_w) - A_w]}}{2\beta} \tag{3.28}$$

where g_c is the core-to-core magnetic airgap and s_w is the primary-to-secondary winding separation. Increasing g_c directly increases the principal magnetic reluctance, whereas s_w primarily alters winding position, leakage and mutual coupling. The two dimensions are therefore treated independently in the Chapter 4 sensitivity studies.

The dimensionless geometrical ratio is:

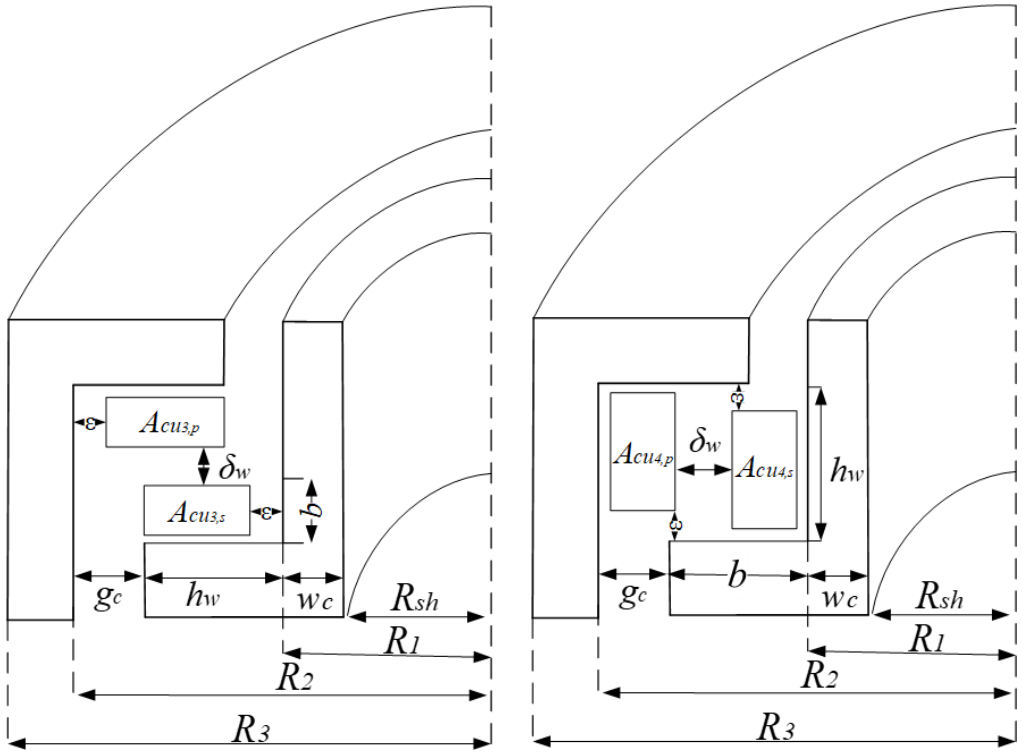
$$k_2 = \frac{g_c}{\delta_w} \tag{3.29}$$

The ratio k_2 replaces the NEW1 upper-to-lower gap ratio and is used only as a geometrical descriptor. The more enclosed geometry changes both the magnetic return path and the available winding access. Its suitability is assessed from the linked magnetic and converter results in Chapter 4.

3.2.5 L-Type 1 and L-Type 2

The L-type candidates use the same general winding-sizing relationships as the radial reference but arrange the magnetic limb and winding window differently. Figure

3.5 shows the two orientations. The primary-to-secondary winding separation is denoted by δ_w ,the winding-to-core clearance by ε and the core-to-core magnetic airgap by g_c. These dimensions retain the same physical definitions used elsewhere in this chapter.



(a) L-type 1 (b) L-type 2

Figure 3.5 L-type rotary transformer geometries

L-type 1 places a larger part of the winding region along the lateral magnetic limb. The open window provides direct access to the winding and allows a different radial-to-axial distribution from the radial C-type structure. The altered winding position also changes the leakage path, local field distribution and effective inductance presented to the DAB.

L-type 2 retains the open L-shaped arrangement but changes the winding orientation. This gives a second installation direction and produces a different mean conductor length and magnetic return path from L-type 1. Its electrical behaviour therefore depends on the combined winding resistance, leakage, coupling and local magnetic loading.

The winding areas are obtained from Equations (3.4) and (3.5), while Figure 3.5 defines how those areas are accommodated within each L-type geometry. The corresponding active sections are listed in Table 3.2.

3.3 DAB Converter Design and Operating Principles

The RT requires a power electronic stage to generate the medium frequency excitation and regulate transferred power across the rotating interface. This function is provided by a dual active bridge (DAB) converter, comprising active bridges on the two sides of the RT and an effective series transfer inductance. Under single-phase-shift (SPS) modulation, the relative displacement between the bridge voltage waveforms controls the magnitude and direction of average power transfer[10][11].

The electrical characteristics of the RT enter directly into the converter design. The turns ratio determines the referred voltage, while RT leakage contributes to the inductance through which the bridge-voltage difference drives the transfer current. Switching frequency and bridge voltage also determine the flux excursion imposed on the magnetic core through the voltage-frequency relationship developed in Section 3.2. The converter and RT parameters are therefore selected together.

The RT leakage inductance referred to the primary side is denoted by L_σ. The total effective transfer inductance referred to the same side is L_{eq}. When an additional series inductance L_{ext} is included,

$$L_{\mathrm{eq}} = L_\sigma + L_{\mathrm{ext}} \tag{3.30}$$

All inductance terms used in the following equations are referred to the same side of the RT. For the three-phase arrangement, the corresponding per-phase quantity is denoted by $L_{eq,ph}$.

The phase-shift angle is denoted by φ, while Φ is reserved for magnetic flux. $V_{\mathrm{dc},1}$and $V_{\mathrm{dc},2}$denote the converter DC link voltages. The instantaneous primary bridge voltage and the secondary bridge voltage referred to the primary side are written as $v_p(t)$ and $v_s'(t)$, respectively. V_p and $V_s$are reserved for RMS RT terminal voltages where these quantities are reported in Chapter 4.

3.3.1 Design Basis and Investigation Cases

Three electrical cases are used in the subsequent analysis. The reduced-scale platform provides the experimental RT-DAB case, the 600 V/100 kW design provides the intermediate electromagnetic case, and the 1.8 kV/1 MW model provides the MW-class linked field-circuit case. Their ratings and operating frequencies follow the requirements of the individual studies and are summarised in Table 3.3.

The reduced-scale platform uses a common 42 V DC source for the two active bridges, a ferrite C-core RT and a nominal 1 mm assembled core-to-core airgap. The quantitative measurements used in Chapter 4 are obtained at 20 kHz. This operating frequency is selected after the lower-frequency tests showed insufficient magnetic operating margin for the available laboratory core. The platform is used to examine the RT terminal waveforms, voltage ratio and phase-shift-controlled transfer under practical converter operation.

The intermediate RT is designed for a nominal 600 V RMS, 100 kW requirement at 2 kHz. The resulting core and winding geometry are used in the 2D and 3D FEM models. For the transient comparison presented in Chapter 4, the external sinusoidal source has a peak amplitude of 600 V and the secondary winding is connected to a 3.6 Ω resistive load.

The MW-class investigation uses a nominal 1 MW transfer requirement and a three-phase RT-DAB linked field-circuit model at 2 kHz. The initial RT sizing uses 24 turns and a 1.8 kV RMS winding design voltage. The converter DC link voltages are separate circuit quantities and are defined independently in the linked model. This investigation is used to compare the candidate RT geometries, winding parameters, turns ratio and converter interaction under a common numerical boundary.

These design roles are summarized in Table 3.3.

Table 3.3 Design conditions of the three RT-DAB investigations

Investigation	Electrical and frequency basis	Implemented circuit	Power and loss boundary	Purpose
Reduced-scale experiment	Common 42 V DC source, 20 kHz, nominal 1 mm core airgap	Single-phase DAB-RT-DAB platform	Measured RT AC-terminal voltage/current and derived terminal power quantities	Examination of waveform, voltage ratio and phase-shift behaviour
Intermediate RT design	RT design basis: 600 V RMS/100 kW, 2 kHz	Transient FEM comparison: 600 V peak sinusoidal source-RT-3.6 Ωload	RT input/load output and modelled magnetic/winding loss	Comparison of the 2D and 3D electromagnetic models
MW-class RT-DAB	1 MW requirement, initial RT sizing at 1.8 kV RMS winding voltage, 2 kHz	Three-phase DAB-RT-DAB linked field-circuit model	RT losses and DC port powers	Comparison of RT geometry, winding parameters and voltage transformation

Switching frequency is selected together with the magnetic design. For prescribed winding voltage, turns and effective core area, increasing frequency reduces the required flux excursion according to Equation (3.1). This must be balanced against semiconductor switching loss, magnetic loss and frequency-dependent winding loss. The high power numerical studies use 2 kHz, while the 20 kHz laboratory condition reflects the characteristics of the reduced-scale ferrite core and converter hardware.

The effective transfer inductance is selected with the required voltage, power and phase-shift range. A smaller L_{eq} produces a larger current for a given bridge-voltage difference, whereas a larger value limits the transferable power. Since the candidate RT geometries do not have identical leakage inductances, the corresponding converter currents are obtained using their geometry-specific electromagnetic models in Chapter 4.

3.3.2 Single-Phase DAB converter

Figure 3.6 shows the single-phase DAB used to define the SPS power transfer relationships. Each side comprises a full bridge connected to a DC link. The two bridge outputs are coupled through the RT and the effective transfer inductance referred to the primary side.

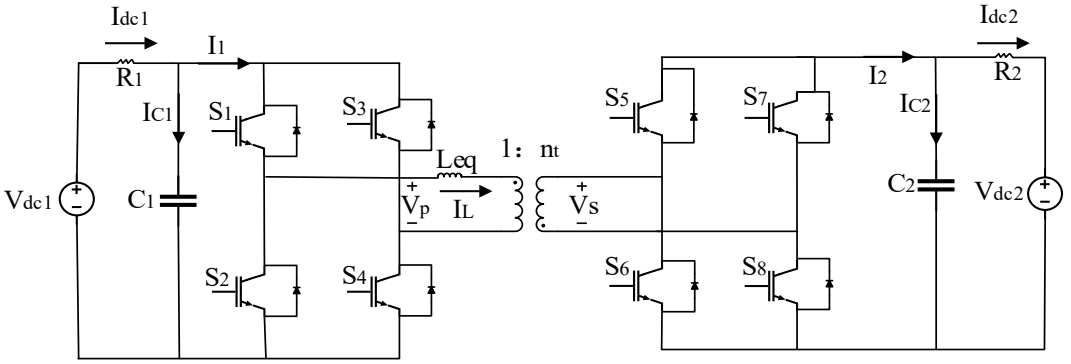


Figure 3.6 Circuit schematics of single-phase DAB converter interfaced with the RT windings

In Figure 3.6,V_{dc1} and V_{dc2} are the primary- and secondary-side DC link voltages, and C_1 and C_2 are the corresponding DC link capacitors. The RT winding turns are N_p and N_s, and all referred secondary-side quantities in the following equations are referred to the primary side. The bridge switches are labelled S_1-S_4 and S_5-S_8 on the primary and secondary sides, respectively.

The RT turns ratio is defined as

$$n_t = \frac{N_p}{N_s} \tag{3.31}$$

where N_p and N_s are the primary and secondary side winding turns, respectively. When secondary side quantities are referred to the primary side, the referred secondary bridge voltage is written as

$$v_s'(t) = n_t v_s(t) \tag{3.32}$$

Under SPS modulation, the secondary bridge waveform is displaced from the primary bridge waveform by the phase shift angle φ. The corresponding time displacement is

$$t_{\varphi} = \frac{\varphi}{2\pi f_s} = \frac{\varphi}{2\pi} T_s \tag{3.33}$$

where f_s is the switching frequency and $T_s = 1/f_s$ is the switching period.

For ideal single-phase shift operation and $0 \leq \varphi \leq \pi$, the average transferred power referred to the primary side can be expressed as [10]

$$P_{\mathrm{DAB}} = \frac{n_t V_{\mathrm{dc},1} V_{\mathrm{dc},2}}{2\pi^2 f_s L_{\mathrm{eq}}} \varphi(\pi - \varphi) \tag{3.34}$$

The expression shows that transferred power is determined jointly by the two DC link voltages, RT turns ratio, switching frequency, effective transfer inductance and phase shift. For the ideal symmetrical case, the analytical maximum occurs at $\varphi = \frac{\pi}{2}$ [10][11]. Semiconductor current, magnetic loading, circulating current, switching loss and soft-switching requirements can restrict the practical operating range.

The current through the effective transfer path is governed by

$$\frac{di_L(t)}{dt} = \frac{v_p(t) - v_s'(t)}{L_{\mathrm{eq}}} \tag{3.35}$$

where $v_p(t)$ is the primary bridge voltage, $v_s'(t)$ is the primary referred secondary bridge voltage and $i_L(t)$ is the current through the effective transfer inductance and RT winding path. Because the bridge voltages are piecewise constant within each switching interval, the ideal current is piecewise linear.

Figure 3.7 shows the corresponding ideal SPS waveforms. The primary bridge voltage $v_p(t)$ and primary-referred secondary bridge voltage $v_s'(t)$ have the same switching frequency and are separated by φ. Their difference is applied across L_{eq}, producing the transfer current $i_L(t)$. The current slope within each switching interval follows directly from Equation (3.35).

At $\varphi = 0$, the bridge waveforms are aligned, and Equation (3.31) gives zero ideal average transferred power for matched referred voltages. Increasing φ changes the duration of the differential voltage applied across L_{eq}, thereby changing the current waveform and transferred power.

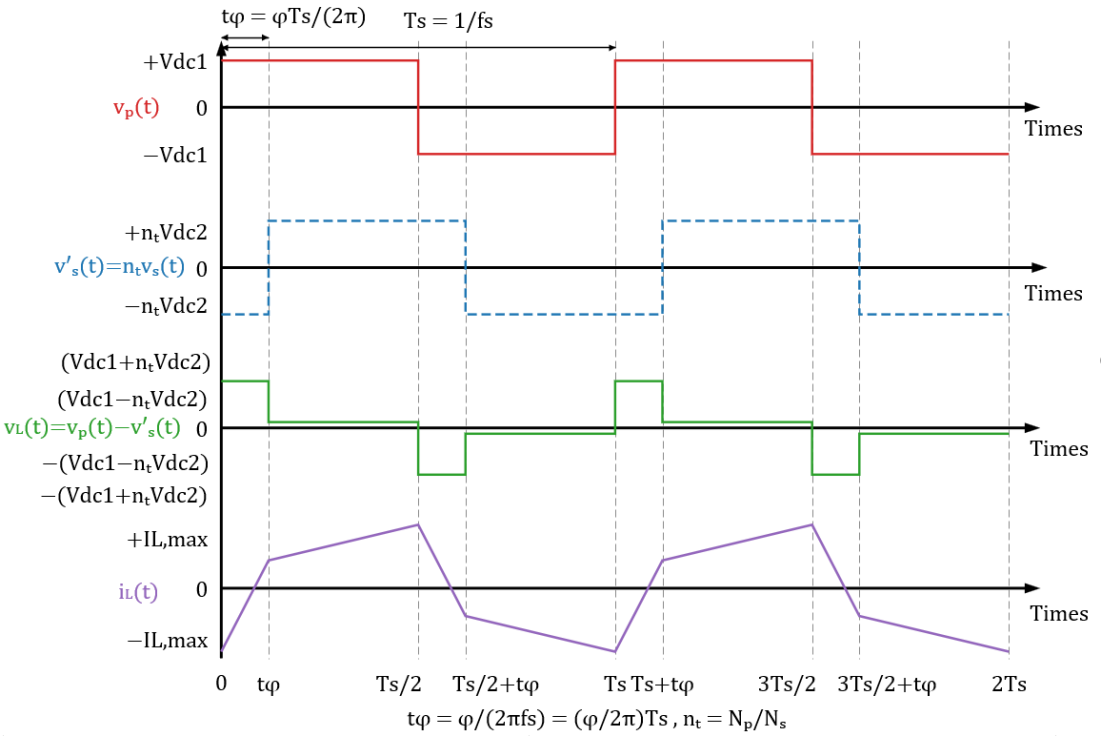


Figure 3.7 Single-phase DAB voltage and current waveforms under SPS control

3.3.3 Three-Phase DAB converter

The three-phase DAB applies the same SPS principle to three coordinated bridge legs on each side of the RT. Three-phase DAB arrangements have been investigated for high power isolated conversion and allow the transferred power to be distributed among three phase channels[12]- [16]. The MW-class model used in this thesis employs this arrangement with balanced Y-Y-connected RT windings.

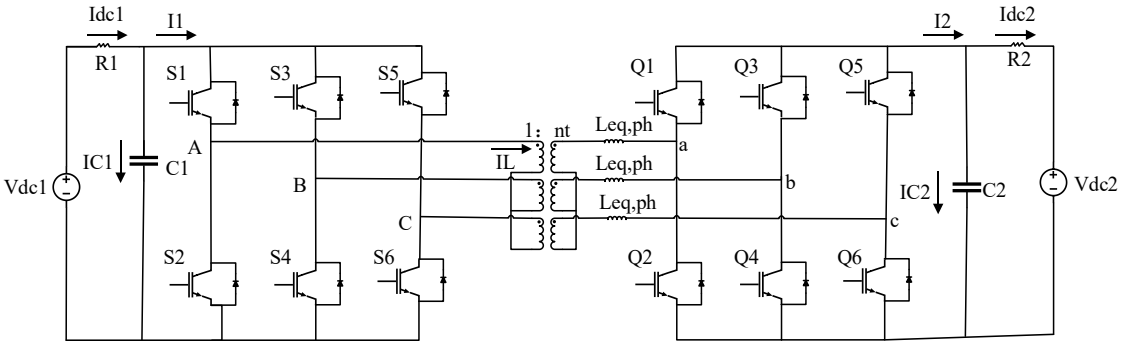


Figure 3.8 Circuit schematics of three-phase DAB converter interfaced with the RT windings

Within each bridge, the three phase-leg switching functions are displaced by 120°. The same inter-bridge phase-shift command φ is applied between corresponding primary and secondary-side phases

Figure 3.8 shows the three-phase DAB and Y-Y-connected RT used in the linked field-circuit model.

For each phase, the primary-referred effective transfer inductance is

$$L_{eq,ph} = L_{\sigma,ph} + L_{ext,ph} \tag{3.36}$$

where the RT leakage contribution and any deliberately introduced external inductance are referred to the same side. The corresponding phase current satisfies

$$\frac{di_{ph}(t)}{dt} = \frac{v_{p,ph}(t) - v'_{s,ph}(t)}{L_{\mathrm{eq}}} \tag{3.37}$$

For ideal three-phase SPS operation over the interval stated in Equation (3.38), the analytical transferred-power relationship used in this thesis is [12][15]

$$P_{3ph} = \frac{n_t V_{dc1} V_{dc2}}{12\pi^2 f_s L_{eq,ph}} \phi(4\pi - 3\varphi) \tag{3.38}$$

V_{dc1} and V_{dc2} in this equation are the converter DC link voltages. They are distinct from the RT terminal RMS voltages V_p and V_s.

Rearranging Equation (3.38) gives the corresponding phase-shift estimate

$$\varphi = \frac{2\pi}{3}\left(1 - \sqrt{1 - \frac{9 f_s L_{eq,ph} P_{3ph}}{n_t V_{dc1} V_{dc2}}}\right) \tag{3.39}$$

Equation (3.39) is provided that the radicand is non-negative and the assumptions of Equation (3.38) remain valid.

The MW-class numerical study evaluates phase-shift commands of 0°, 30°, 60°and 90°. Equation (3.38) is used only within its stated analytical interval, extending to 60°. The 90°operating point is obtained directly from the linked field-circuit simulation rather than from extrapolation of the closed-form expression.

The Y-Y connection is retained throughout the MW-class study so that the phase-voltage and turns-ratio definitions remain unchanged when the five RT geometries are compared. Alternative winding connections would alter the line-to-phase voltage relationship and phase current and are outside the comparisons presented in Chapter 4.

The single and three-phase relationships defined here provide the converter quantities required by the integrated RT-DAB design procedure in Section 3.4. The same voltage, inductance, turns-ratio and phase-shift definitions are retained in the Chapter 4 numerical and experimental analyses.

3.4 Integrated RT-DAB Design Procedure

The analytical RT relationships developed in Section 3.2 and the DAB converter relationships established in Section 3.3 are combined here to define the design procedure used for the Chapter 4 investigations. The magnetic design establishes the winding, core and clearance requirements, while the converter calculation checks whether the resulting turns ratio and transfer inductance are compatible with the required voltage, current and phase-shift operating range.

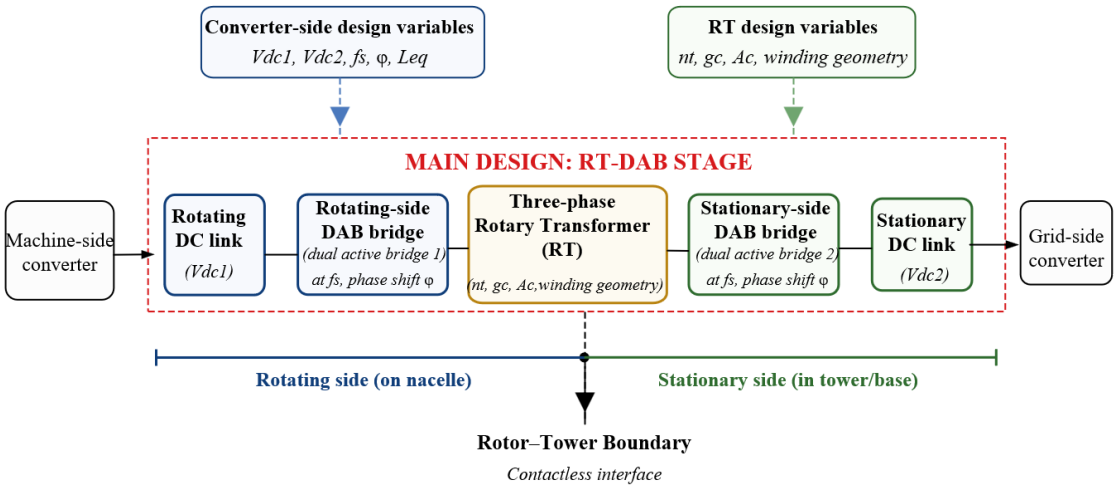


Figure 3.9 RT-DAB power transfer stage and principal design variables

The complete electrical path from the secondary generator to the stationary grid interface is shown in Figure 2.3. Figure 3.9 isolates the RT-DAB stage from that system and identifies the quantities used directly in the present design. On the converter side these are the DC link voltages V_{dc1} and V_{dc2}, switching frequency f_s, phase-shift angle φ and effective transfer inductance L_{eq}, The RT-side variables include the turns ratio n_t, core-to-core magnetic airgap g_c, effective core area A_c, and winding geometry.

For a prescribed winding voltage and switching frequency, the winding turns and effective core area determine the magnetic flux excursion through Equation (3.1). Core

geometry and g_c determine the principal magnetic reluctance, while winding position, window dimensions and δ_w affect conductor accommodation and leakage. The resulting RT leakage forms part of L_{eq}, which together with the bridge voltages and φ determines the transfer current and power described in Section 3.3.

The design calculation starts from the electrical rating and geometrical constraints of the investigation under consideration. The required transferred power, winding or converter voltage, switching frequency and magnetic material are specified first. Suitable values of magnetic flux density, current density and winding fill factor are then selected together with the available annular dimensions and the required magnetic and winding clearances. The relationships developed in Section 3.2 are used to determine the initial winding turns, effective core area, conductor area and winding window dimensions.

These quantities are then applied to the selected RT geometry. Because the magnetic path and winding arrangement differ among the original radial, NEW1, NEW2, L-type 1 and L-type 2 structures, each geometry has its own magnetic reluctance, mean turn length and leakage inductance.

The resulting RT design is then checked against the DAB operating requirements. The selected turns ratio must provide the required voltage relationship, while L_{eq}, switching frequency and phase shift must provide the required transfer range without excessive current under the specified operating condition. If the magnetic loading, winding accommodation or converter current falls outside the selected limits, the relevant magnetic, winding or converter parameter is revised and the calculation is repeated.

The procedure in Figure 3.10 represents an iterative engineering design procedure, no objective function or numerical optimisation algorithm is used. Designs that meet the specified magnetic, geometrical and converter limits are subsequently examined using the FEM or linked field-circuit models in Chapter 4.

The analytical calculation provides the initial magnetic and winding dimensions but does not resolve local fringing, non-uniform flux distribution, magnetic saturation or geometry-dependent leakage. These quantities are obtained from the electromagnetic models in Chapter 4.

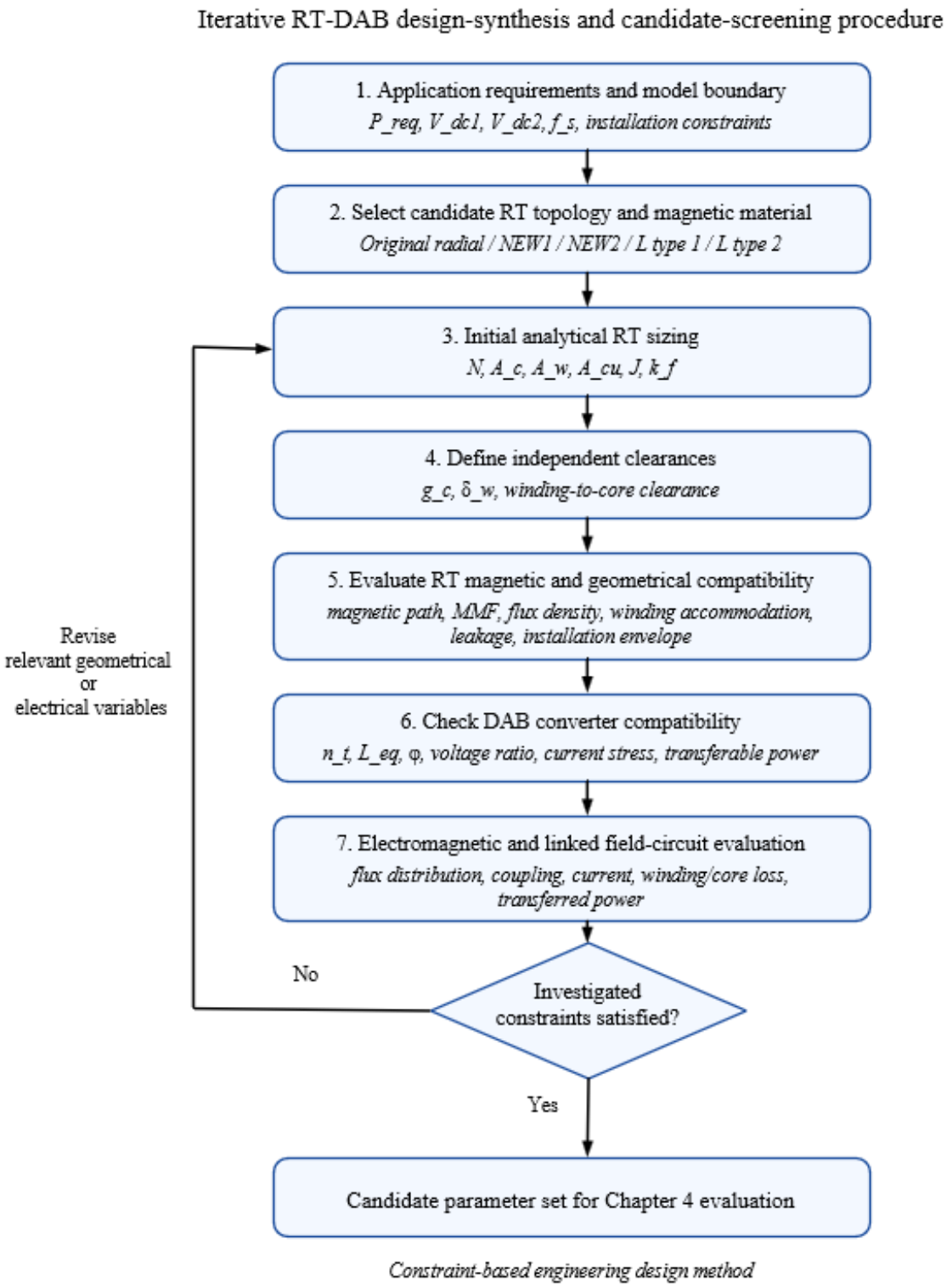


Figure 3.10 RT-DAB design procedure

Table 3.4 summarises the principal RT and DAB quantities carried from the analytical design into the Chapter 4 investigations.

Table 3.4 lists the RT and DAB quantities used in the Chapter 4 analyses

Design quantity	Role in Chapter 3	Use in Chapter 4
B_c, B_g, A_c, and magnetic reluctance and g_c	Define the initial core dimensions and magnetic operating condition	Flux-density distributions and magnetic-gap studies
k_f, A_w, A_{Cu},J and winding geometry	Define winding dimensions, copper occupation and first-order winding resistance	Winding-separation and fixed-window fill-factor studies
Candidate RT geometry	Define the magnetic return path and winding position	Comparison of the original radial, NEW1, NEW2, L type 1 and L type 2 geometries
$n_t = N_p/N_s$	Define the nominal voltage ratio and referred secondary quantities	Voltage-ratio comparison for the investigated winding arrangements
φ, L_{eq}, V_{dc1}, V_{dc2} and f_s	Define the DAB excitation and transfer-current relationship	Experimental waveforms and MW-class linked field-circuit results
P_{cu}, $P_{\mathrm{core}}$and electrical input/output powers	Define the winding/core losses and electrical power balance	Loss and efficiency calculations at the stated model boundary

3.5 Chapter Summary

This chapter developed the analytical design basis for the RT-DAB power transfer stage selected in Chapter 2. The RT calculation relates winding voltage and excitation frequency to winding turns, magnetic flux density and effective core area, while current density, conductor area and winding fill factor determine the initial winding dimensions. Magnetic reluctance and mean turn length are included to estimate the principal magnetic-path and winding-resistance quantities required before numerical modelling. The core-to-core magnetic airgap, primary-to-secondary winding separation and winding-to-core clearances are defined separately because they enter the magnetic and winding design in different ways.

Five RT geometries are considered: the original radial type, NEW1, NEW2, L-type 1 and L-type 2. The radial structure provides the analytical reference, while NEW1 and NEW2 are developed in this work to provide alternative magnetic-return and winding window arrangements for the X-ROTOR installation space. The L-type structures

provide further comparison with more open winding regions and different conductor orientations. Each geometry retains its own magnetic path, active section, winding position and mean conductor length, the same analytical relationships therefore lead to different physical RT designs.

The converter analysis established the quantities required to operate these RTs within a DAB power transfer stage. The single-phase formulation defined the turns ratio, primary-referred secondary voltage, effective transfer inductance and SPS phase-shift relationship. The RT leakage inductance contributes to the effective transfer inductance seen by the converter, so the bridge voltages, switching frequency, phase shift and RT magnetic design cannot be selected independently. The same notation and operating relationships are then applied to the balanced three-phase DAB arrangement used for the MW-class linked field-circuit study.

The electrical conditions used in the subsequent investigations are also defined. The reduced-scale RT-DAB platform operates from the common 42 V DC source at 20 kHz with a nominal 1 mm assembled core airgap. The intermediate 600 V/100 kW RT is examined using analytical and 2D and 3D electromagnetic models at 2 kHz. The MW-class study uses a three-phase RT-DAB model at 2 kHz, with a 1 MW transfer requirement and a 1.8 kV RMS winding voltage for the initial RT design. These cases serve different stages of the analysis and retain their respective electrical and modelling conditions.

The RT and DAB calculations are finally combined in the iterative design procedure of Section 3.4. Initial magnetic and winding dimensions are obtained from the analytical equations and checked against the required turns ratio, effective transfer inductance, converter current and phase-shift operating range. The resulting dimensions and operating quantities provide the inputs to Chapter 4, where local flux distribution, magnetic saturation, geometry-dependent leakage, winding and core losses, voltage transformation and converter-coupled behaviour are examined using experimental measurements, FEM and linked field-circuit simulation.

3.6 Chapter References

[1]*E. E. Landsman, "Rotary transformer design," in Proc. IEEE Power Electronics Specialists Conference, Greenbelt, MD, USA, Apr. 1970, pp. 139-152.*

[2]*K. D. Papastergiou and D. E. Macpherson, "Contact less transfer of energy by means of a rotating transformer," in Proc. IEEE International Symposium on Industrial Electronics, Dubrovnik, Croatia, 2005, pp. 1735-1740, doi: 10.1109/ISIE.2005.1529194.*

[3]*N. L. Zietsman and N. Gule, "Design and evaluation of a 1.2 kVA single-phase rotary transformer," in Proc. 22nd International Conference on Electrical Machines (ICEM), Lausanne, Switzerland, 2016, pp. 1466-1472.*

[4]*W. G. Hurley, W. H. Wölfle, and J. G. Breslin, "Optimised transformer design: inclusive of high frequency effects," IEEE Transactions on Power Electronics, vol. 13, no. 4, pp. 651 659, 1998, doi: 10.1109/63.704133.*

[5]*W. T. McLyman, Transformer and Inductor Design Handbook, 4th ed. Boca Raton, FL, USA: CRC Press, 2011.*

[6]*M. A. Bahmani, T. Thiringer, and M. Kharezy, "Design methodology and optimization of a medium frequency transformer for high power DCDC applications," IEEE Transactions on Industry Applications, vol. 52, no. 5, pp. 4225-4233, Sep./Oct. 2016, doi: 10.1109/TIA.2016.2582825.*

[7]*J. P. C. Smeets, L. Encica, and E. A. Lomonova, "Comparison of winding topologies in a pot core rotating transformer," in Proc. 12th International Conference on Optimization of Electrical and Electronic Equipment (OPTIM), Brasov, Romania, 2010, pp. 103-110, doi: 10.1109/OPTIM.2010.5510563.*

[8]*J. Legranger, G. Friedrich, S. Vivier, and J. C. Mipo, "Comparison of two optimal rotary transformer designs for highly constrained applications," in Proc. IEEE International Electric Machines & Drives Conference (IEMDC), Antalya, Turkey, 2007, vol. 2, pp. 1546-1551, doi: 10.1109/IEMDC.2007.383658.*

[9]*J. Godbehere, A. Hopkins, and X. Yuan, "Design and thermal analysis of a rotating transformer," in Proc. IEEE International Electric Machines & Drives Conference (IEMDC), San Diego, CA, USA, 2019, doi: 10.1109/IEMDC.2019.8785234.*

[10]*B. Zhao, Q. Song, W. Liu, and Y. Sun, "Overview of dual active bridge isolated bidirectional DC DC converter for high frequency link power conversion system," IEEE Transactions on Power Electronics, vol. 29, no. 8, pp. 4091-4106, 2014, doi: 10.1109/TPEL.2013.2289913.*

[11]*S. Shao, H. Chen, X. Wu, J. Zhang, and K. Sheng, "Circulating current and ZVS on of a dual active bridge DC DC converter: a review," IEEE Access, vol. 7, pp. 50561-50572, 2019, doi: 10.1109/ACCESS.2019.2911009.*

[12]*R. W. De Doncker, D. M. Divan, and M. H. Kheraluwala, "A three-phase soft switched high power density DC/DC converter for high power applications," IEEE Transactions on Industry Applications, vol. 27, no. 1, pp. 63-73, 1991, doi: 10.1109/28.67533.*

[13]*S. Haghbin, M. Alatalo, F. Yazdani, T. Thiringer, and R. Karlsson, "The design and construction of transformers for a 50 kW three-phase dual active bridge DC/DC converter," in Proc. IEEE Vehicle Power and Propulsion Conference (VPPC), 2017, pp. 1-5, doi: 10.1109/VPPC.2017.8330965.*

[14]*H. J. Choi, B. G. Seo, M. H. Ryu, Y. P. Cho, and J. H. Jung, "Effective magnetic component design of three-phase dual active bridge converter for LVDC distribution system," IEEE Transactions on Industrial Electronics, vol. 68, no. 3, pp. 1828-1840, 2021, doi: 10.1109/TIE.2020.2972462.*

[15]*D. D. Nguyen, N. T. Bui, and K. Yukita, "Design and optimization of three-phase dual active bridge converters for electric vehicle charging stations," Energies, vol. 13, no. 1, 2020, doi: 10.3390/en13010150.*

[16]*S. P. Engel, N. Soltau, H. Stagge, and R. W. De Doncker, "Dynamic and balanced control of three-phase high power dual active bridge DC DC converters in DC grid applications," IEEE Transactions on Power Electronics, vol. 28, no. 4, pp. 1880-1889, 2013, doi: 10.1109/TPEL.2012.2209461.*

[17]*H. Vardhan, M. Odavic, and K. Atallah, "Design optimization methodology for high frequency rotary transformers for contactless power transfer systems," in Proc. IEEE Energy Conversion Congress and Exposition (ECCE), Detroit, MI, USA, 2022, doi: 10.1109/ECCE50734.2022.9948210.*

[18]*N. Toscani, M. Brunetti, M. S. Carmeli, F. Castelli Dezza, and M. Mauri, "Design of a rotary transformer for installations on large shafts," Applied Sciences, vol. 12, no. 6, Art. no. 2932, 2022, doi: 10.3390/app12062932.*

[19]*D. Bortis, L. Fässler, A. Looser, and J. W. Kolar, "Analysis of rotary transformer concepts for high speed applications," in Proc. 28th Annual IEEE Applied Power Electronics Conference and Exposition (APEC), Long Beach, CA, USA, 2013, pp. 3262-3269, doi: 10.1109/APEC.2013.6520768.*

[20]*T. Raminosoa, R. H. Wiles, and J. Wilkins, "Novel rotary transformer topology with improved power transfer capability for high speed applications," IEEE Transactions on Industry Applications, vol. 56, no. 1, pp. 277-286, 2020, doi: 10.1109/TIA.2019.2955050.*

[21]*R. Manko, S. Čorović, and D. Miljavec, "Analysis and design of rotary transformer for wireless power transmission," in Proc. 2020 IEEE Problems of Automated Electrodrive: Theory and Practice (PAEP), 2020, pp. 1-6, doi: 10.1109/PAEP49887.2020.9240870.*

[22]*S. Botha and N. Gule, "Design and evaluation of a laminated three-phase rotary transformer for DFIG applications," Energies, vol. 15, no. 11, Art. no. 4061, 2022, doi: 10.3390/en15114061.*

[23]*H. Krupp and A. Mertens, "Rotary transformer design for brushless electrically excited synchronous machines," in Proc. 2015 IEEE Vehicle Power and Propulsion Conference (VPPC), Montreal, QC, Canada, 2015, pp. 1-6, doi: 10.1109/VPPC.2015.7353009.*

[24]*S. Ditze, A. Endruschat, A. Schriefer, and M. März, "Inductive power transfer system with a rotary transformer for contactless energy transfer on rotating applications," in Proc. 2016 IEEE International Symposium on Circuits and Systems (ISCAS), Montreal, QC, Canada, 2016, pp. 1622-1625, doi: 10.1109/ISCAS.2016.7538876.*

[25]*Y. Zhang, J. Yang, D. Jiang, D. Li, and R. Qu, "Design, manufacture, and test of a rotary transformer for wireless power transfer system," IEEE Transactions on Magnetics, vol. 58, no. 2, Art. no. 8400206, 2022, doi: 10.1109/TMAG.2021.3094135.*

Chapter 4

4 Design and Evaluation of Medium and High Power RT-Based WPT Systems

4.1 Introduction

Previous chapters define the X-ROTOR drivetrain and its rotating electrical power transfer requirement[1], and consider contactless alternatives to conventional slip ring interface[2]-[5]. Chapter 3 develops the analytical design of the rotary transformer and the associated DAB converter, including magnetic dimensions, winding arrangement, turns ratio, transfer inductance and power transfer relationships for phase-shift control[6]-[8]. These calculations provide the initial RT dimensions and converter operating quantities. Finite-element and circuit models are required to determine the local magnetic-field distribution, geometry-dependent leakage, magnetic non-linearity and converter waveforms that are not obtained from the analytical calculation alone.

The reduced-scale RT-DAB platform is examined first. The hardware operates from a common 42 V DC source at 20 kHz with a nominal 1 mm assembled core-to-core airgap. Section 4.2 describes the experimental arrangement, measurement positions and FFT processing before presenting the measured results. A Maxwell-Simplorer model of the same RT and electrical arrangement is then compared with the measured terminal voltages, currents and power quantities. The 1 mm configuration is the experimental condition, the larger core-airgap cases considered later in Section 4.2 are numerical studies.

Section 4.3 considers the intermediate single-phase RT. The analytical design is based on a nominal 600 V RMS/100 kW requirement at 2 kHz. The corresponding transient FEM comparison retains the implemented 600 V peak sinusoidal excitation and 3.6 Ω secondary load. The 2D and 3D representations are compared under these common circuit conditions before the selected magnetic and winding parameters are examined.

Section 4.4 considers the MW-class RT-DAB model. The original radial, NEW1, NEW2, L type 1 and L type 2 RTs are connected to the same three-phase converter arrangement and are subjected to the same converter commands for the geometry comparison. Further simulations examine primary-to-secondary winding separation, fixed-window winding fill factor and winding turns ratio. The final part of the chapter relates the resulting electrical operating points to the variable generator output and regulated DC link arrangement of the X-ROTOR.

4.2 Reduced-Scale Experimental Platform and Prototype-Matched Validation

The reduced-scale laboratory platform is used to examine the practical operation of the phase-shift-controlled RT-based WPT system described in Chapter 3[6][7][8]. The experiment records the primary- and secondary-side RT terminal voltages and currents for four phase-shift commands under a common 42 V DC supply, 20 kHz operation and a nominal 1 mm core-to-core airgap. A Maxwell-Simplorer model is constructed using the same RT geometry, magnetic material and principal circuit conditions.

4.2.1 Experiment Platform, Operating Conditions and Measurement Method

The experimental platform uses two STEVAL-IPM30B power converter boards[9] controlled by a TI Delfino F28379D digital signal processor[10]. The controller generates the complementary switching commands for the converter stages and applies

the required phase displacement between the primary- and secondary-side bridge voltages. Both converter boards are supplied from the same 42 V DC source.

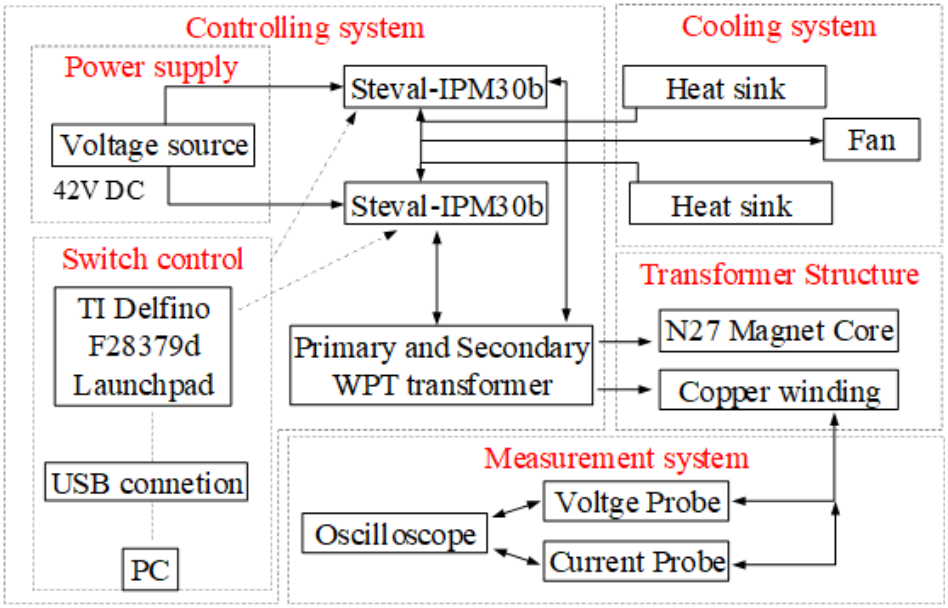
Figure 4.1 shows the converter arrangement, controller, RT and laboratory implementation. The primary voltage v_p, primary current i_p, secondary voltage v_s and secondary current i_s are measured at the AC terminals of the RT using voltage and current probes connected to the oscilloscope. These measurement positions define the AC-terminal quantities used in the subsequent waveform and FFT analyses.

The reduced-scale RT uses an N27 ferrite C core[11] with enamelled 16-AWG copper windings[12]. Figure 4.2 shows the fabricated RT and the N27 magnetic characteristic used in the corresponding Maxwell model. The nominal assembled core-to-core airgap for the quantitative measurements is 1 mm. The same winding turns and winding regions are used in the numerical model.

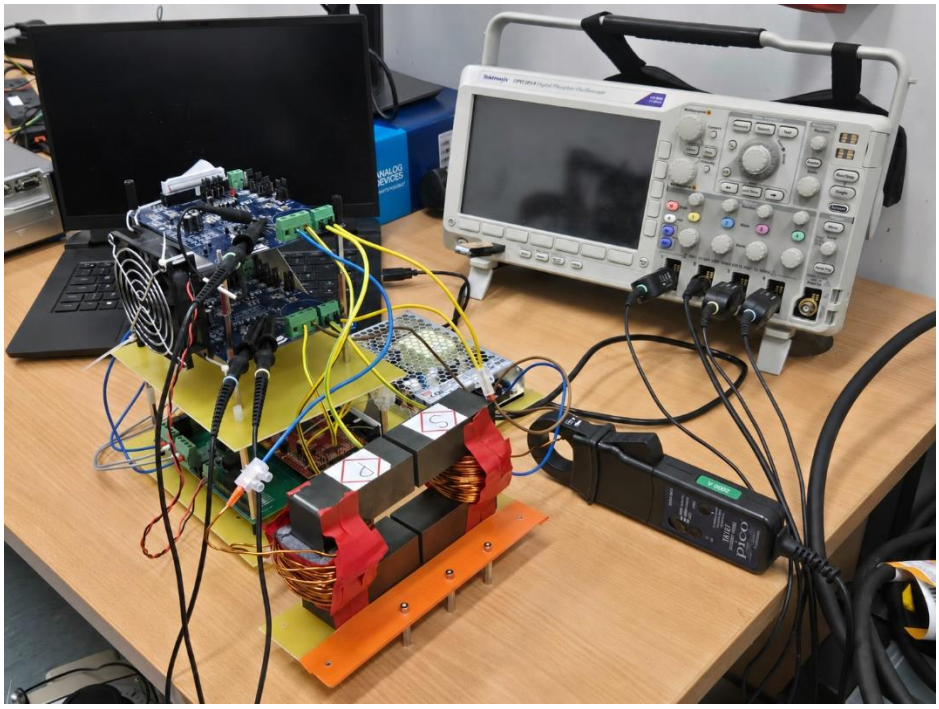
Preliminary tests at 2 kHz show current behaviour consistent with excessive magnetic excitation of the available ferrite core. The quantitative measurements are therefore obtained at 20 kHz. For fixed applied voltage, winding turns and effective core area, the voltage-frequency-flux relationship in Chapter 3 shows that increasing the excitation frequency reduces the required magnetic flux excursion. The 20 kHz condition consequently provides greater magnetic operating margin for the N27 core. All quantitative experimental results in this section use the 20 kHz switching frequency and the nominal 1 mm core-to-core airgap.

The four phase-shift commands are applied while the primary- and secondary-side voltages and currents are recorded at the RT AC terminals. The power quantities derived from these measurements therefore refer to the RT AC-terminal measurement positions. They do not include a complete DC port loss measurement of the two converter stages.

The measured waveforms are sampled at 10 MHz and processed using the FFT procedure described in Section 4.2.3 and Appendix B. The 20 kHz switching-frequency component is used as the fundamental component for the reported RMS and power calculations. The same procedure is applied to the simulated waveforms for direct comparison with the experimental quantities.

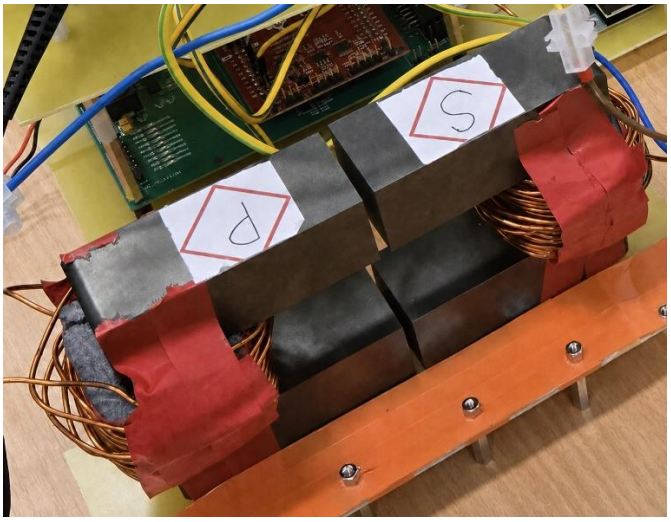


(a) converter, control and RT-terminal measurement arrangement

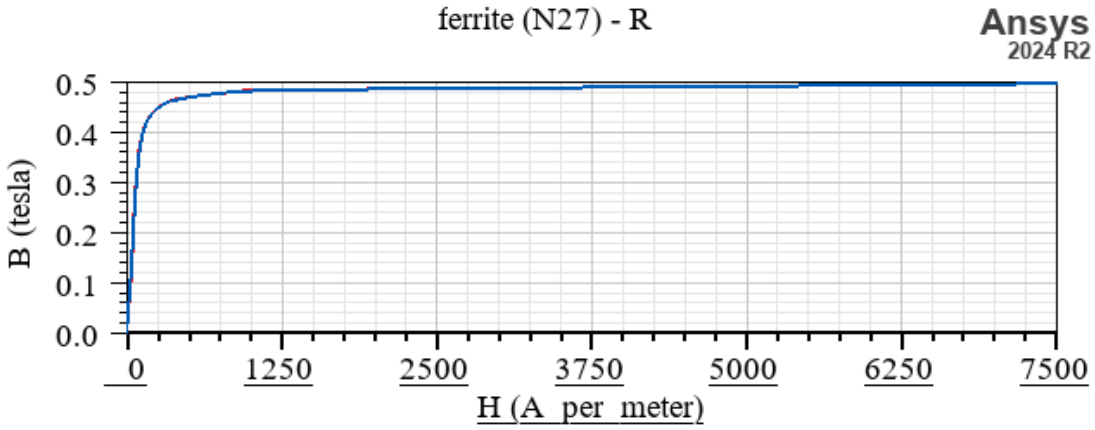


(b) laboratory hardware implementation

Figure 4.1 Configuration and implementation of the reduced-scale RT-based WPT platform



(a) N27 C core RT prototype

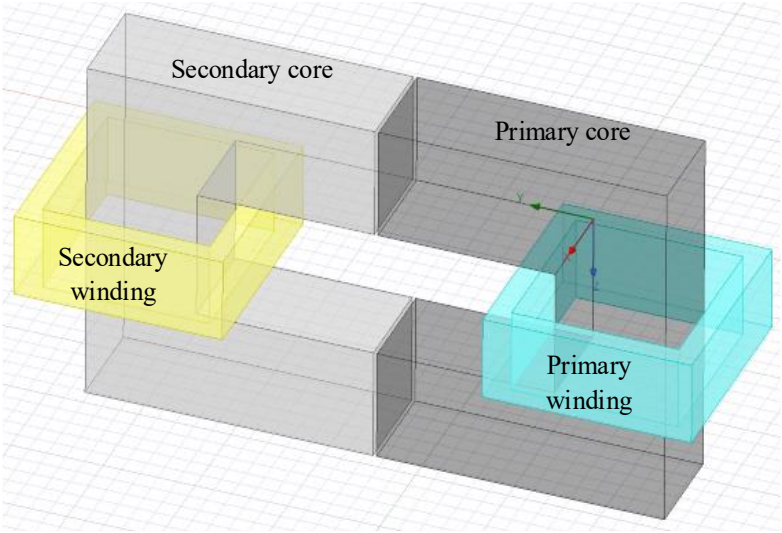


(b)N27 magnetic characteristic assigned to the prototype-matched Maxwell model

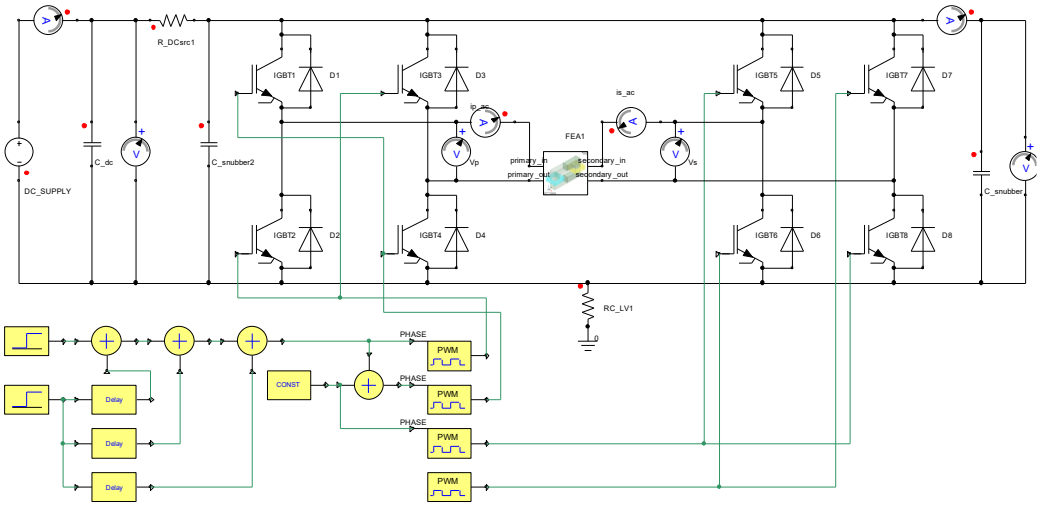
Figure 4.2 Reduced-scale RT and magnetic material

The prototype-matched model consists of the N27 C-core RT represented in Maxwell and the associated converter circuit represented in Simplorer[13]. Figure 4.3 shows the electromagnetic and circuit models. The model uses the documented core geometry and winding regions, a 1 mm core-to-core airgap, the common 42 V DC source, a 20 kHz switching frequency and the same four phase-shift commands used in the experiment. The primary- and secondary-side voltages and currents are extracted at the corresponding RT AC-terminal locations.

The prototype-matched model uses the documented hardware geometry, material, excitation and converter conditions summarised in Table 4.1. The comparison is therefore based on an independently specified parameter set, allowing the measured and numerical responses to be assessed on a common physical and electrical basis.



(a)N27 C core RT



(b)linked circuit model

Figure 4.3 Prototype-matched Maxwell-Simplorer model of the reduced-scale RT-based WPT platform

Table 4.1 Operating conditions and measurement boundaries for the reduced-scale experiment and prototype-matched model

Quantity	Experimental platform	Prototype-matched simulation
DC source	One common 42 V source supplying both converter boards	Common 42 V source supplying both converter stages
Switching frequency	20 kHz	20 kHz
Core material	N27 ferrite	N27 magnetic characteristic

Core-to-core airgap	1mm	1mm
Phase-shift commands	0°, 30°, 60° and 90°	0°, 30°, 60° and 90°
RT geometry	Fabricated C-core RT	Prototype-matched C-core geometry
Winding definition	Fabricated primary and secondary windings	Documented turns and winding regions
Measurement position	Primary and secondary RT AC terminals	Corresponding RT AC terminals
Quantities	v_p, i_p, v_s, i_s	v_p, i_p, v_s, i_s
Sampling frequency	10 MHz	Exported numerical waveforms
Fundamental frequency for FFT	20 kHz	20 kHz
Post-processing	FFT, RMS, active power, reactive power and PF	Same procedure

The measured and simulated waveforms obtained under these conditions are compared in Sections 4.2.2 and 4.2.3.

4.2.2 Comparison of Measured and Simulated Terminal Waveforms

The same phase-shift sequence is applied to the experimental platform and the prototype-matched model described in Section 4.2.1, The commanded phase shift is increased through 0°, 30°, 60°and 90°, as shown in Figure 4.4(a). Figure 4.4(b) and Figure 4.4(c) how the measured RT terminal voltages and currents, while Figure 4.4(d) and Figure 4.4(e) show the corresponding simulated quantities. The steady-state RMS values, active and reactive powers and power factors are considered separately in Section 4.2.3.

The displacement between the primary- and secondary-side terminal voltages follows the commanded phase-shift sequence in both the measured and simulated waveforms. The primary and secondary voltage levels also remain similar, consistent with the common 42 V DC source and the 1:1 winding arrangement.

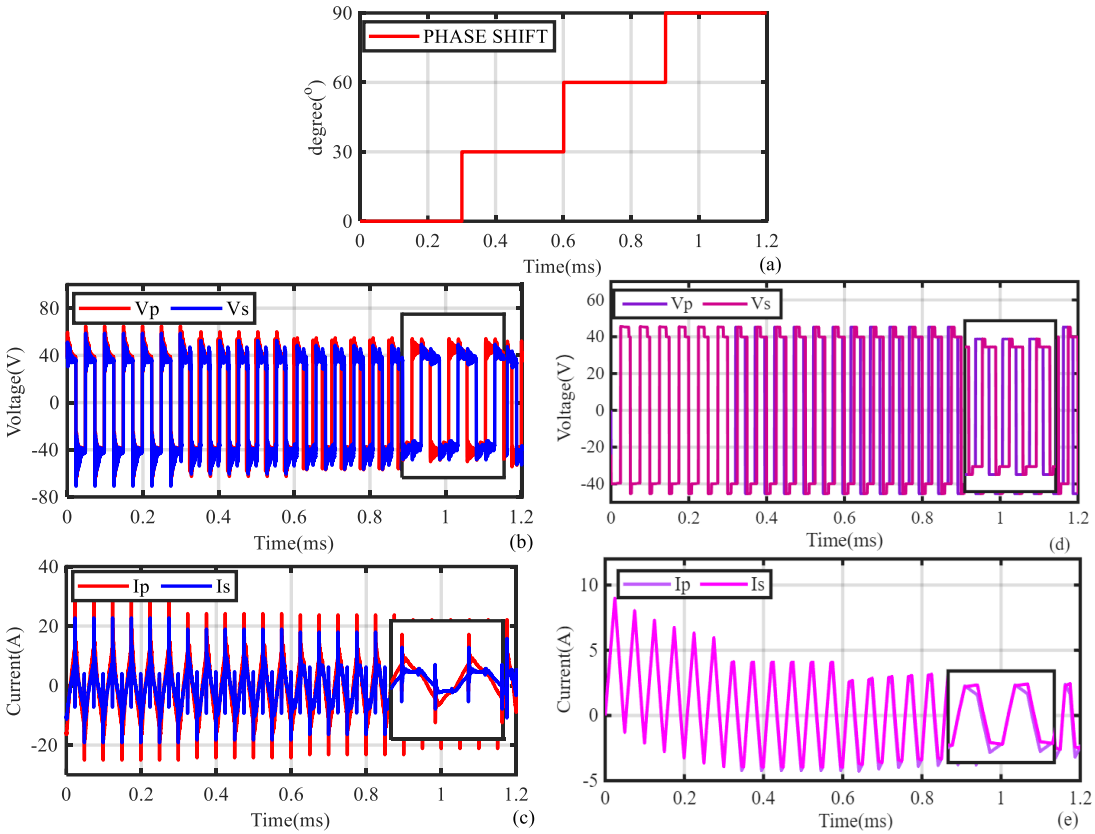


Figure 4.4 Comparison of measured and simulated RT terminal waveforms under the laboratory operating condition (a) Phase shift angle (b) Measured V_p and V_s (c) Measured I_p and I_s (d) Simulated V_p and V_s (e) Simulated I_p and I_s

The measured voltage waveforms contain overshoot, ringing and distortion around the switching transitions, whereas the simulated waveforms show more uniform voltage levels and sharper transitions. These differences are consistent with hardware effects that are simplified or omitted in the numerical model, including semiconductor voltage drops, dead time, cable and connector impedance, parasitic capacitance, probe bandwidth and board-level switching behaviour[14][15]. The model therefore captures the switching frequency, phase displacement and terminal-voltage level without reproducing all the high frequency features present in the measured waveforms.

The measured and simulated currents have the same periodic switching behaviour, but their instantaneous magnitudes and transition peaks differ. The simulated primary- and secondary-side currents are close to one another because the model uses symmetric 1:1 windings and a simplified representation of converter and interconnection parasitics. In the experiment, the difference between i_p and i_s, together with the larger switching-related peaks, is associated with the combined effects of magnetising current, effective

leakage inductance, winding and connection resistance, semiconductor dead time and circuit parasitic[14][15][16][17].

The continuous current record in Figure 4.5 includes the initial energisation transient and the response following each change in phase-shift command. It is therefore used to examine the temporal evolution and switching behaviour of the current rather than to quantify a steady-state phase-shift characteristic. The corresponding steady-state RMS quantities and cycle-averaged powers are obtained from the selected analysis intervals in Section 4.2.3, where reactive and circulating components are treated explicitly.

The time domain comparison shows closer correspondence in switching frequency, phase displacement and terminal-voltage level than in current magnitude. The current difference is examined quantitatively using the FFT-derived values in the following section.

4.2.3 FFT Based Quantitative Comparison

The measured and simulated waveforms are processed using the same MATLAB-based FFT procedure. The complex voltage and current components at the 20 kHz switching frequency are extracted and converted to RMS phasors. The voltage, current and power quantities reported in this section therefore refer to the 20 kHz fundamental component of the switching waveforms. The definitions of fundamental active power, reactive power and power factor follow[18]. and the MATLAB procedure is given in Appendix B.

For either RT terminal $x \in p, s$, the magnitude of the fundamental power factor is calculated from

$$\left|PF_{1,p}\right| = \frac{\left|P_{x,1}\right|}{V_{x,1,\mathrm{rms}} I_{x,1,\mathrm{rms}}} \tag{4.1}$$

where $P_{x,1}$ is the fundamental active-power component. The signs of the active-power values in Table 4.2 result from the adopted voltage, current and probe reference directions. Power factor magnitudes are therefore used when comparing the operating points.

Because the primary and secondary bridges are supplied from a common DC source, non-zero circulating and magnetizing components are present at the 0° operating point. Similar non-power transferring current components are recognised in phase-shift-controlled DAB converters and influence converter current stress and conduction loss [19][20][21]. The phase-shift-dependent changes are consequently evaluated relative to the 0° baseline:

$$\Delta P_x(\delta) = P_{x,1}(\delta) - P_{x,1}(0^\circ), \Delta Q_x(\delta) = Q_{x,1}(\delta) - Q_{x,1}(0°), x \in \{p, s\} \quad (4.2)$$

and

$$PF_{\Delta,x} = \frac{|\Delta P_x|}{\sqrt{(\Delta P_x)^2 + (\Delta Q_x)^2}} \quad (4.3)$$

An incremental AC terminal power transfer efficiency is also defined as

$$\eta_{\Delta,AC} = \frac{|\Delta P_s|}{|\Delta P_p|} \times 100\% \quad (4.4)$$

The incremental AC-terminal transfer efficiency quantifies the proportion of the phase-shift-induced change in primary fundamental active power that appears at the secondary RT terminal. It is a baseline-referenced AC-terminal metric, complete DC to DC efficiency additionally includes the converter conduction, switching and auxiliary losses.

Table 4.2 Experimental fundamental phasors and power components from the FFT analysis

Primary side quantities				
φ	0^o	30^o	60^o	90^o
$V_{p,1rms}$(V)	37.7375 ∠ 69.46°	38.2675 ∠ 69.50°	38.7233 ∠ 69.76°	39.0777 ∠ 70.15°
$I_{p,1rms}$(A)	9.0235 ∠ 165.47°	8.7596 ∠ 176.80°	7.9693 ∠ 172.46°	6.6613 ∠ 163.25°
$P_{p,1}$(W)	-35.6600	-99.7010	-143.8277	-155.2070
$Q_{p,1}$(Var)	338.6505	320.0388	273.0309	208.9774
Secondary side quantities				
$V_{s,1rms}$(V)	37.1315 ∠ 70.38°	36.7520 ∠ 100.64°	36.3110 ∠ 130.77°	35.9218 ∠ 160.81°

$I_{s,1rms}$(A)	5.5484 ∠ 170.76°	5.3775 ∠ 171.36°	4.8172 ∠ 153.29°	3.9627 ∠ 134.46°
$P_{s,1}$(W)	-37.1467	6.8631	42.5033	60.7523
$Q_{s,1}$(Var)	202.6445	197.5129	169.6757	128.7303

Table 4.2 gives the measured fundamental phasors and power components for the four phase-shift commands. The primary RMS voltage remains between 37.7375 V and 39.0777 V, while the secondary voltage remains between 35.9218 V and 37.1315 V. The primary reactive-power component decreases from 338.6505 Var at $\varphi = 90°$, while the magnitude of the primary active-power component increases over the same range. The phase-shift command therefore changes the balance between active and reactive power at the RT terminals.

Table 4.3 Comparison of measured and simulated fundamental RMS quantities

Voltage components				
φ	0^o	30^o	60^o	90^o
$V_{p,1,exp}$(V)	37.7375	38.2675	38.7233	39.0777
$V_{p,1,sim}$(V)	38.0779	38.7357	39.2515	39.7081
$V_{s,1,exp}$(V)	37.1315	36.7520	36.3110	35.9218
$V_{s,1,sim}$(V)	38.0840	37.4994	37.0525	36.6267
Current components				
$I_{p,1,exp}$(A)	9.0235	8.7596	7.9693	6.6613
$I_{p,1,sim}$(A)	2.8164	2.6900	2.4017	1.9731
$I_{s,1,exp}$(A)	5.5484	5.3775	4.8172	3.9627
$I_{s,1,sim}$(A)	2.8106	2.6840	2.3900	1.9507

Table 4.3 compares the measured and simulated fundamental RMS voltages and currents. The primary-side voltage difference is approximately 0.9-1.6%, while the

secondary-side difference is approximately 2.0-2.6%. The terminal-voltage levels are therefore represented more closely than the current magnitudes.

The simulated primary current is approximately 69% lower than the measured value, and the simulated secondary current is approximately 49% lower. The difference indicates that the prototype-matched model does not reproduce the effective impedance and current distribution of the experimental assembly with the same accuracy as the terminal voltage. Possible contributors include differences in leakage and magnetising inductance, winding and connection impedance, semiconductor dead time and voltage drop, and circuit parasitic[14]-[17]. The available measurements do not separate the contribution of each effect.

Table 4.4 Measured and simulated power factor and AC-terminal transfer metrics

δ	0^o	30^o	60^o	90^o
$\lvert PF_{1,p}\rvert_{exp}$	0.1047	0.2974	0.4661	0.5962
$\lvert PF_{1,p}\rvert_{sim}$	0.0806	0.2303	0.4265	0.5910
$PF_{\Delta,p,exp}$		0.9600	0.8540	0.6770
$PF_{\Delta,p,sim}$		0.9481	0.9143	0.7820
$PF_{\Delta,s,exp}$		0.9930	0.9210	0.7980
$PF_{\Delta,s,sim}$		0.8934	0.7654	0.5951
$\eta_{\Delta,AC,exp}(\%)$		68.72	73.63	81.89
$\eta_{\Delta,AC,sim}(\%)$		65.41	72.76	73.81

The measured primary fundamental power factor increases from 0.1047 at $\varphi = 0°$ to 0.5962 over the investigated phase-shift sequence. The corresponding simulated values increase from 0.0806 to 0.5910. At the highest investigated phase shift, the difference between the measured and simulated fundamental power factors is 0.0052, even though the current magnitudes differ substantially. The phase relationship between the fundamental voltage and current is therefore represented more closely than the current amplitude.

The incremental power factors show the changes produced by the phase-shift command after removal of the $\varphi = 0°$ baseline. Their variation is not identical on the primary and secondary sides because the incremental active and reactive-power components change at different rates.

The experimental values of $\eta_{\Delta,\mathrm{AC}}$ are 68.72%, 73.63% and 81.89% at $\varphi = 30°, 60°$ and $90°$. respectively. The corresponding simulated values are 65.41%, 72.76% and 73.81%. The differences are therefore 3.31, 0.87 and 8.08 percentage points. These quantities refer only to the baseline-referenced fundamental active-power change between the two RT AC terminals.

Power factor also affects the current and apparent-power requirements of the converter. For a given active-power transfer, a lower power factor requires a higher apparent-power rating and a higher RMS current, increasing the current rating required of the semiconductor devices and conductors[19][20][21]. A numerical converter-cost difference is not calculated here because the present study does not include a component-level converter cost model.

The comparison therefore shows similar terminal-voltage levels and similar fundamental power factor trends in experiment and simulation, but a substantial difference in current magnitude remains. Section 4.2.4 uses the numerical model to examine the effect of changing the core-to-core airgap, only the 1 mm condition corresponds to the experimental hardware.

4.2.4 Effect of Core-to-Core Airgap on the Prototype-Matched Model

The experiment-simulation comparison in Section 4.2.2 and 4.2.3 uses the nominal 1 mm assembled core-to-core airgap of the fabricated RT. The prototype-matched Maxwell-Simplorer model is then evaluated with core-to-core airgaps of 1, 5, 10 and 15 mm. The core geometry, winding arrangement, material properties, common 42 V DC supply, 20 kHz switching frequency and phase-shift commands remain unchanged.

The core airgap g_c, considered here is the mechanical clearance between the opposing core surfaces. It is distinct from the primary-to-secondary winding separation

and the winding-to-core clearance defined in Chapter 3. Increasing g_c increases the reluctance of the principal magnetic path and generally reduces magnetising inductance and magnetic coupling[22][23]. Table 4.5 gives the simulated magnetic parameters for the four airgap values.

The primary self-inductance decreases from 641.4699 at $g_c = 1$mm to 175.8998 at $g_c = 15$ mm, a reduction of approximately 72.6%. The secondary self-inductance changes by a similar amount. Over the same range, the coupling factor decreases from 0.8307 to 0.3301, corresponding to a reduction of approximately 60.3%. This trend is consistent with the magnetic-reluctance relationship developed in Chapter 3.

Table 4.5 Simulated magnetic parameters of the prototype-matched RT at different core-to-core airgaps

g_c(mm)	$L_p(\mu$H)	$L_s(\mu$H)	Coupling factor (k)
1	641.4699	640.2795	0.83070
5	267.7435	269.0302	0.58299
10	197.9598	197.0557	0.42172
15	175.8998	175.3462	0.33010

The simulated waveforms for each airgap are processed using the FFT procedure described in Section 4.2.3. Table 4.6 gives the corresponding incremental active-power components, power factors and AC-terminal transfer metric. Each incremental quantity is referenced to the $\varphi = 0°$ operating point for the same airgap.

Table 4.6 Incremental power transfer quantities for different core-to-core airgaps and phase-shift angles

g_c(mm)	φ°	$\lvert\Delta P_p\rvert$(W)	$\lvert\Delta P_s\rvert$(W)	$PF\Delta, p$	$PF\Delta, s$	$\eta_{\Delta,\mathrm{AC}}(\%)$
1	30	31.4447	20.5757	0.9481	0.8934	65.43
1	60	48.8453	35.5399	0.9143	0.7654	72.76
1	90	54.9419	40.5511	0.7820	0.5951	73.81
5	30	25.4992	15.2096	0.9870	0.8740	59.635

5	60	39.0654	26.7078	0.9200	0.7446	68.37
5	90	43.6468	30.6251	0.7920	0.5750	70.17
10	30	21.2500	11.1772	0.9898	0.8488	52.60
10	60	32.1408	20.1086	0.9255	0.7229	62.56
10	90	35.2938	23.1855	0.7990	0.5549	65.69
15	30	18.2724	8.5434	0.9902	0.8232	46.76
15	60	27.0589	15.7575	0.9270	0.6998	58.23
15	90	29.7477	18.2892	0.8040	0.5355	61.48

The fundamental terminal-voltage and current magnitudes change less than the magnetic parameters under the fixed converter commands. At $\varphi = 60°$, for example, the primary voltage changes from 39.2515 V at 1 mm to 38.7812 V at 15 mm, while the secondary voltage changes from 37.0525 V to 37.5065 V. Over the same range, the primary and secondary current magnitudes change from 2.4017 A and 2.3900 A to 2.3107 A and 2.2922 A, respectively. The bridge-voltage levels and switching states are fixed by the converter arrangement, while the magnetic coupling changes with g_c.

The change in transferred active power is more pronounced. At $\varphi = 60°$, $|\Delta P_p|$ decreases from 48.8453 W at 1 mm to 27.0589 W at 15 mm, while $|\Delta P_s|$ decreases from 35.5399 W to 15.7575 W. The corresponding $\eta_{\Delta,\mathrm{AC}}$ decreases from 72.76% to 58.23%. At $\varphi = 90°$, $|\Delta P_s|$ decreases from 40.5511 W to 18.2892 W, while $\eta_{\Delta,\mathrm{AC}}$ decreases from 73.81% to 61.48%.

The primary incremental power factor increases slightly as the airgap is increased under the investigated conditions, whereas the secondary incremental power factor decreases. The two quantities therefore follow different trends because the corresponding incremental active- and reactive-power components do not change at the same rate.

The 1 mm case corresponds to the assembled experimental RT. The 5, 10 and 15 mm cases are numerical variations of the same prototype-matched model. The self-

inductance and coupling-factor values in Table 4.5 are also obtained from the numerical model.

4.3 Intermediate-Scale RT Design and Comparative FEM Assessment

Section 4.2 examines the reduced-scale RT-DAB platform under converter-generated phase-shift excitation. This section considers the separate 600 V/100 kW single-phase RT introduced in Chapter 3 and examines its electromagnetic behaviour using 2D and 3D finite-element models. The analytical dimensions are first transferred to the FEM geometry, after which the two representations are compared under the same electrical conditions. The 2D model is then used for the parameter studies in Section 4.3.3.

4.3.1 Design Basis and Electromagnetic Model

The intermediate RT is analytically sized for a primary voltage of 600 V RMS, a transferred-power requirement of 100 kW and an excitation frequency of 2 kHz[24]. M250-35A electrical steel is used for the magnetic core and copper for the primary and secondary windings. Figure 4.5 shows the magnetic characteristic implemented in Ansys Maxwell.

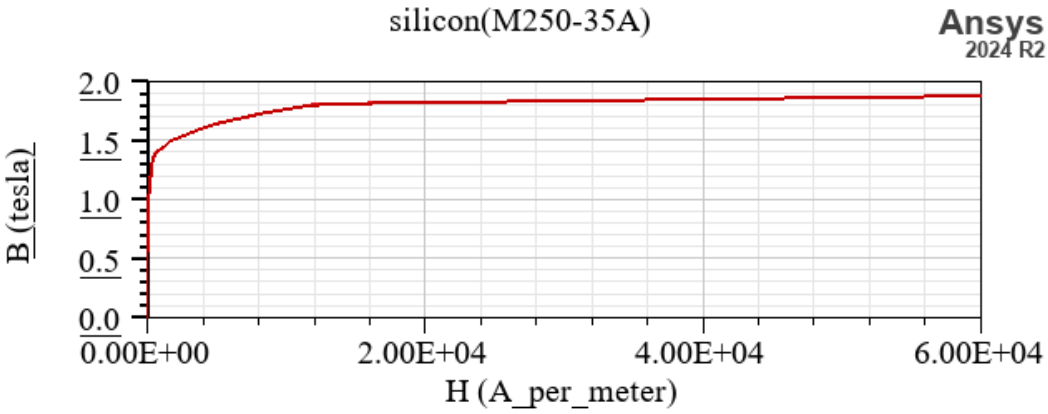


Figure 4.5 Magnetic characteristic of the M250-35A electrical steel implemented in the FEM model.

The value $B_0 = 0.7$ T is selected as the analytical design flux-density target. This value defines the magnetic loading used to calculate the initial core cross-sectional area from the voltage-frequency-flux relationship developed in Chapter 3. The design point lies below the strongly nonlinear region of the material characteristic shown in Figure 4.5, leaving allowance for the local flux concentration subsequently obtained from the field solution. The FEM result is therefore assessed using the local flux-density distribution rather than by assuming that the analytical design value is the maximum field anywhere in the core.

Using the analytical voltage relationship from Chapter 3 with the specified voltage, frequency, turns and flux-density target gives the required core cross-sectional area of approximately 2000 mm². The primary and secondary windings each use 48 turns. For the initial resistive-load sizing, the 100 kW/600 V requirement gives an analytical winding-current value of approximately 166.6 A. This value is used to determine the conductor and winding window dimensions[25][26].

The winding fill factor is calculated from the effective conductor area occupying the available winding window, $N_p = 48$, $A_{\mathrm{cu}} = 41.65\ \mathrm{mm}^2$ and $A_w = 7177.2\ \mathrm{mm}^2$.

$$k_f = \frac{N_P A_{Cu}}{A_w} = \frac{48 \times 41.65}{7177.2} \approx 0.279 \approx 0.28 \tag{4.5}$$

The remaining window area accommodates conductor insulation, spacing, placement tolerances and unused winding space. The value $k_f = 0.28$ therefore follows from the conductor and window dimensions used for this design. The fixed-window fill-factor study in Section 4.4 considers a different condition in which the established winding window is held constant while the represented copper occupation is varied.

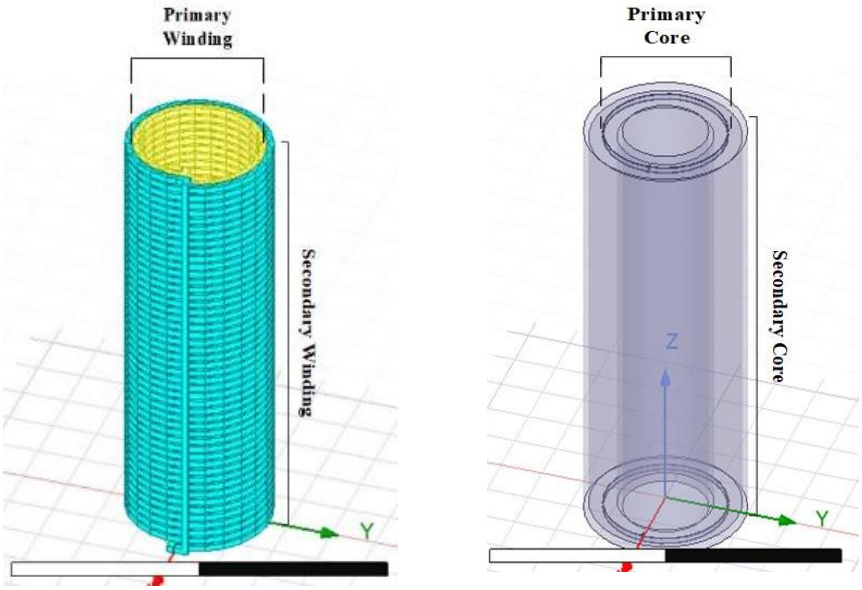
The remaining window area accounts for conductor insulation, turn separation, placement tolerances and unused manufacturing space. The resulting analytical-design parameters and numerical model conditions are summarised in Table 4.7.

Table 4.7 Principal analytical design parameters and retained FEM conditions of the intermediate scale RT

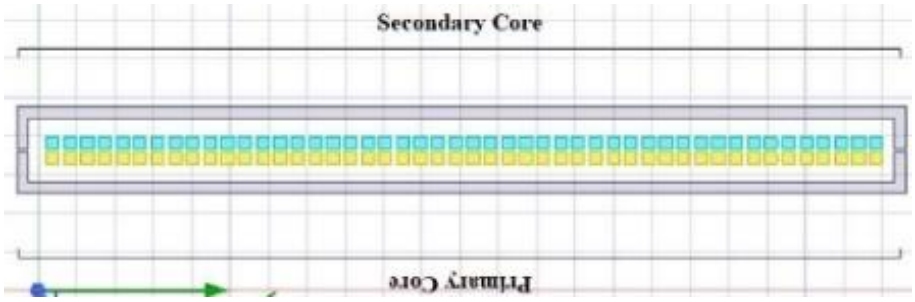
Category	Symbol	Definition	Value
Analytical requirement	$V_{p,rms,req}$	Required Primary RMS voltage	600 V
	P_{req}	Required transferred power	100 kW
	B_0	Analytical design flux density target	0.7 T
	f_{RT}	Electrical excitation frequency	2000 Hz
	k_f	winding fill factor	0.28
	J	current density	4 A/mm^2
Material		Magnetic core material	M250-35A
		Winding material	Copper
Electrical Design	$N_p = N_s$	Primary and secondary number of turns	48
	R_L	Secondary load resistance	3.6 Ω
	$I_{w,rms,calc}$	Analytical winding current used for initial sizing	166.6 A
Magnetic geometry	A_C	Minimum core cross section area	2000 mm^2
	A_w	Winding window cross section area	7177.2 mm^2
	h_w	Axial length of the winding window	451.11 mm
	b_w	Width of the winding window	15.91 mm
	g_c	Core-to-core airgap	1 mm
	w	Cross section width	6.01 mm
	R_{mean}	Mean winding radius	72.42 mm
	R_1	Outer radius of the first effective core section section area A_{C1}	88.8 mm
Winding	ρ_C	Copper resistivity	1.72×10^{-8}Ωm

	l_c	Equivalent conductor cross section side length	6.45 mm
	A_{Cu}	Required conductor cross-sectional area	41.65 mm^2
FEM MODEL	$V_{\mathrm{p,rms,FEM}}$	Applied primary RMS voltage	600 V
	$d_{2\mathrm{D}}$	Equivalent depth of the 2D model	455mm
Reference quantities used in the sensitivity study	$P_{Cu,ref}$	Copper-loss metric	249.54 W
	$P_{core,ref}$	core loss metric	210.36 W
	η	efficiency	98.8%
	L_σ	leakage inductance	17.37 µH
	L_{m}	magnetizing inductance	6.237 mH

The winding regions are represented using the stranded-winding formulation. Current density is therefore assumed to be uniformly distributed over each equivalent conductor cross-section. The reported stranded loss represents the corresponding I^2R winding-loss component and does not include the additional AC resistance associated with strand-level skin and proximity effects. The core loss output is obtained from the material-loss model assigned to the M250-35A regions.



(a) 3D winding regions (b) 3D magnetic cores



(c) 2D axisymmetric model

Figure 4.6 2D and 3D FEM representations of the 600 V/100 kW radial RT

The 3D model represents the complete annular core and winding structures. In the 2D representation, the curved active region is unfolded using an equivalent depth of 455 mm, obtained from the effective circumferential length of the 3D airgap region. This transformation retains the principal active cross-sectional area but omits circumferential curvature, local fringing and end-region effects.

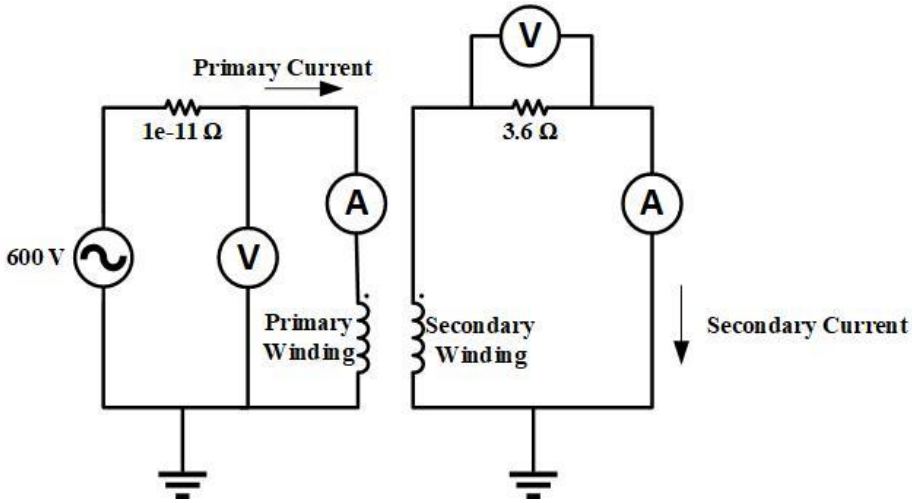


Figure 4.7 Electrical circuit used for the 2D/3D FEM comparison with a 600 V peak, 2 kHz source and 3.6 Ω secondary load.

The model boundary in Figure 4.7 consists of sinusoidal source, RT and secondary resistive load. The 10^{-11} Ω series element shown in Figure 4.7 is a numerical circuit regularization and does not represent physical winding resistance. It is excluded from the RT loss interpretation, the winding-loss contribution is instead obtained from the stranded conductor regions in the electromagnetic model.

The circuit contains no active converter bridges, DC links or phase-shift control. Its purpose is to assess the isolated RT and compare the two electromagnetic

representations before the magnetic component is incorporated into the complete RT-DAB system.

4.3.2 Comparison of 2D and 3D FEM Model

The 2D model is compared with the 3D model before it is used for the repeated parameter studies in Section 4.3.3. Both models use the same winding arrangement, magnetic material, secondary load and nominal 1 mm core-to-core airgap. For the transient comparison, the external sinusoidal source has a peak amplitude of 600 V at 2 kHz.

For a reported quantity (x), the relative difference between the two models is defined as

$$\varepsilon_x = \frac{|x_{2D} - x_{3D}|}{|x_{3D}|} \times 100\% \tag{4.6}$$

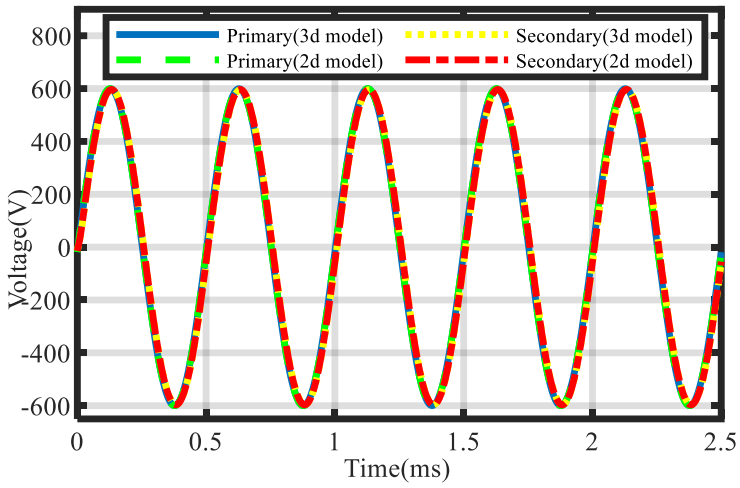
Figure 4.8 compares the primary- and secondary-side voltage and current waveforms and the secondary-load power obtained from the two FEM models. The waveform shapes and magnitudes are closely matched between the 2D and 3D representations. The corresponding steady-state quantities extracted from the FEM results are listed in Table 4.8.

The secondary winding is connected to a 3.6 Ω resistive load. The output power is therefore obtained from the measured RMS secondary voltage and current as

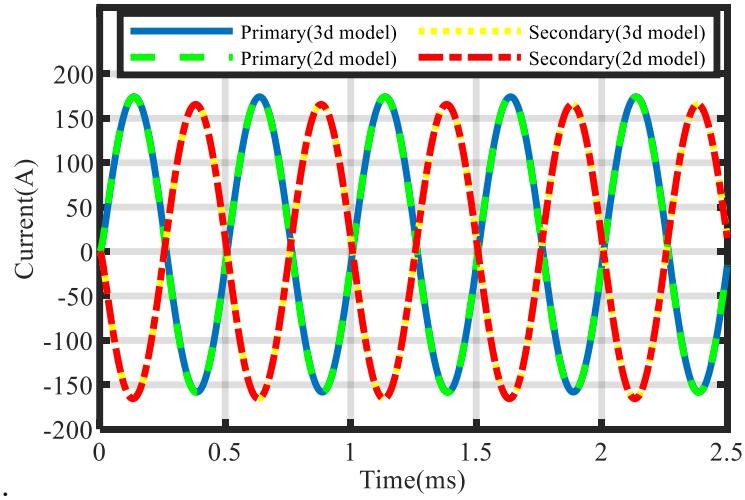
$$P_{out} = V_{s,rms} I_{s,rms} = \frac{V_{s,rms}^2}{R_L} \tag{4.7}$$

where R_L is the secondary load resistance. The measured RMS quantities give output powers of 98.832 kW and 98.787 kW for the 2D and 3D models, respectively.

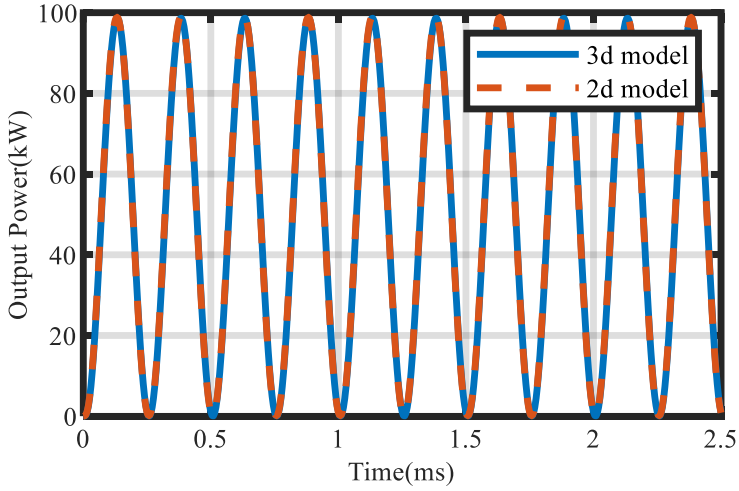
Table 4.8 shows that the circuit-level quantities obtained from the two models are very similar. The primary RMS voltage is 600 V in both models. The secondary RMS voltages are 596.487 V and 596.350 V, giving a deviation of 0.023%. The primary RMS currents are 174.053 A and 174.49 A, while the secondary RMS currents are 165.689 A and 165.652 A. The corresponding deviations are 0.25% and 0.022%, respectively. The output power difference is 0.045%.



(a) Voltages of primary and secondary winding



(b) Currents of primary and secondary windings



(c) Secondary load power

Figure 4.8 Comparison of voltage, current and load power waveforms obtained from the 2D and 3D FEM models

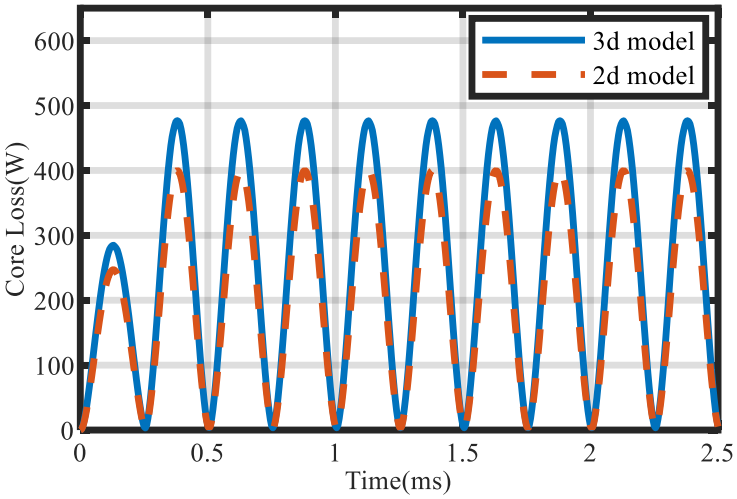


Figure 4.9 Instantaneous core loss outputs obtained from the 2D and 3D FEM representations under the retained excitation conditions

The magnetic quantities show larger differences. Figure 4.9 gives a maximum core-loss value of 479.014 W, compared with 399.563 W for the 2D model, corresponding to a difference of 16.586%. The maximum local flux density is 0.673 T in the 3D model and 0.392 T in the 2D model. The larger local value in the 3D model reflects the influence of circumferential curvature, local fringing and flux concentration in the complete annular structure.

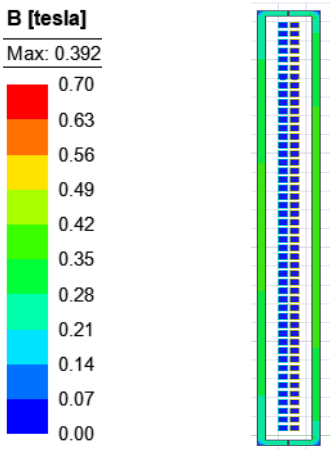
Figure 4.10 shows the magnetic-flux-density distributions. The maximum local flux density is 0.673 T in the 3D model and 0.392 T in the 2D model. The larger local value in the 3D model reflects the influence of circumferential curvature, local fringing and flux concentration in the complete annular structure.

The comparison shows that the 2D model gives closely corresponding terminal voltage, current and output power results under the same operating conditions, while larger differences remain in the local magnetic quantities. The 2D representation is therefore used for the repeated parameter studies in Section 4.3.3, with the differences in local flux density and core loss considered when interpreting the results.

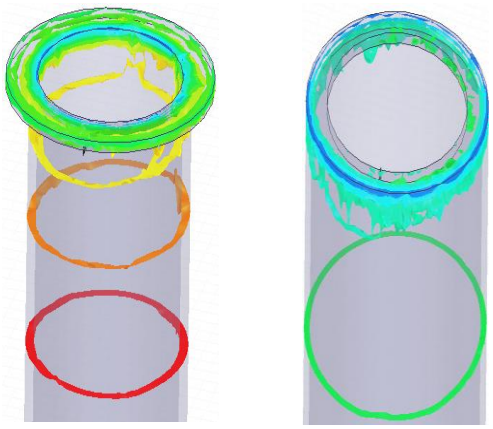
The MW-class study in Section 4.4 uses different RT geometries and a three-phase linked field-circuit model. The present 2D/3D comparison applies to the intermediate RT considered in this section and is not used as a direct 3D comparison of the MW-class candidate geometries.

Table 4.8 Quantitative comparison of key outputs obtained from the 2D and 3D FEM models

Parameter	2D FEM	3D FEM	Deviation
Primary RMS voltage	600V	600V	0%
Secondary RMS voltage	596.487V	596.350V	0.023%
Primary RMS current	174.053A	174.49A	0.25%
Secondary RMS current	165.689A	165.652A	0.022%
Output power	98.832 kW	98.787 kW	0.045%
Core loss	399.563 W	479.014 W	16.586%
Maximum local magnetic flux density	0.392T	0.673T	41.753%



(a)2D model



(b) 3D model

Figure 4.10 Magnetic flux-density distributions of the 2D and 3D RT models

4.3.3 Sensitivity Analysis and RT Design Parameters

The 2D representation is used for the parameter studies in this section. Four design variables are considered: the core-to-core airgap g_c, design flux-density target B_0, current density J, and winding window width b_w. The investigated ranges and nominal values are listed in Table 4.9.

Each parameter is varied separately while the electrical specification, excitation frequency, turns ratio, magnetic material and radial RT topology remain unchanged. Where a selected parameter enters the analytical sizing equations, the dimensions dependent on that parameter are recalculated before the corresponding FEM model is solved. The B_0, J and b_w sweeps therefore represent related RT designs derived from the same electrical specification rather than changes applied to one unchanged transformer geometry. For the airgap sweep, g_c is varied directly while the remaining principal core and winding dimensions are retained.

The quantities compared in Figure 4.11 are the winding copper loss P_{Cu}, core loss P_{core}, and leakage inductance L_σ. P_{Cu} denotes the winding loss obtained from the stranded-conductor representation, P_{core} is obtained from the assigned magnetic-material loss model, and L_σ is the RT leakage inductance used in the transfer-path description developed in Chapter 3.

Figure 4.11(a) shows the effect of increasing the core-to-core airgap. As g_c increases, the leakage inductance increases, reflecting the reduction in magnetic coupling between the primary and secondary windings. The winding copper loss also increases moderately, while the reported core loss decreases over the investigated range. The airgap therefore affects both the magnetic coupling and the electrical quantities presented to the external circuit.

Figure 4.11(b) shows the results obtained when the design flux-density target B_0 is varied. Increasing B_0 reduces the core cross-sectional area required by the voltage relationship in Chapter 3. The resulting change in core dimensions also changes the winding path and magnetic geometry. The corresponding changes in P_{Cu}, P_{core} and L_σ therefore describe the resized RTs associated with the different B_0 values.

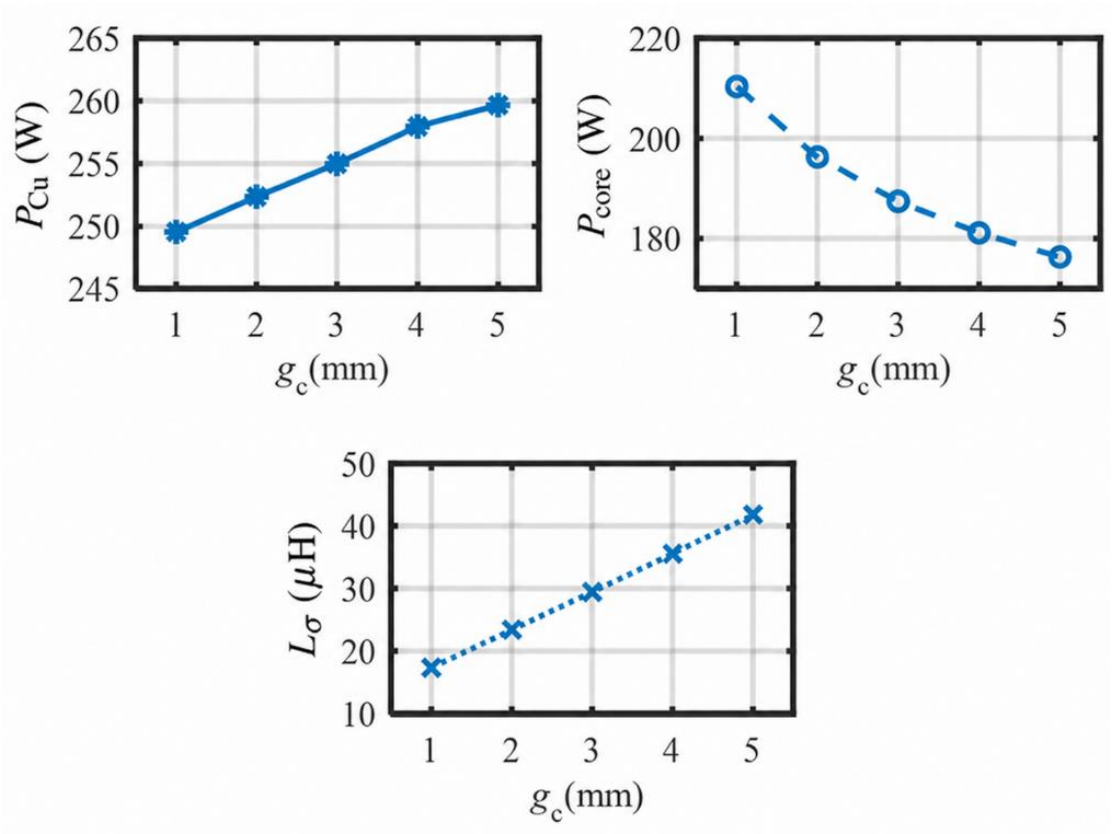
Figure 4.11(c) shows the current-density study. Increasing J reduces the conductor area required for the specified winding current and changes the corresponding winding dimensions. The reduction in P_{Cu} shown in this sweep results from this geometrical recalculation. It does not represent the effect of increasing current density in one unchanged conductor.

Figure 4.11(d) shows the effect of winding window width. Changing b_w alters the winding geometry and mean conductor path. Over the investigated range, increasing $b$produces moderate increases in P_{Cu} and L_σ, together with a reduction in the reported P_{core}.

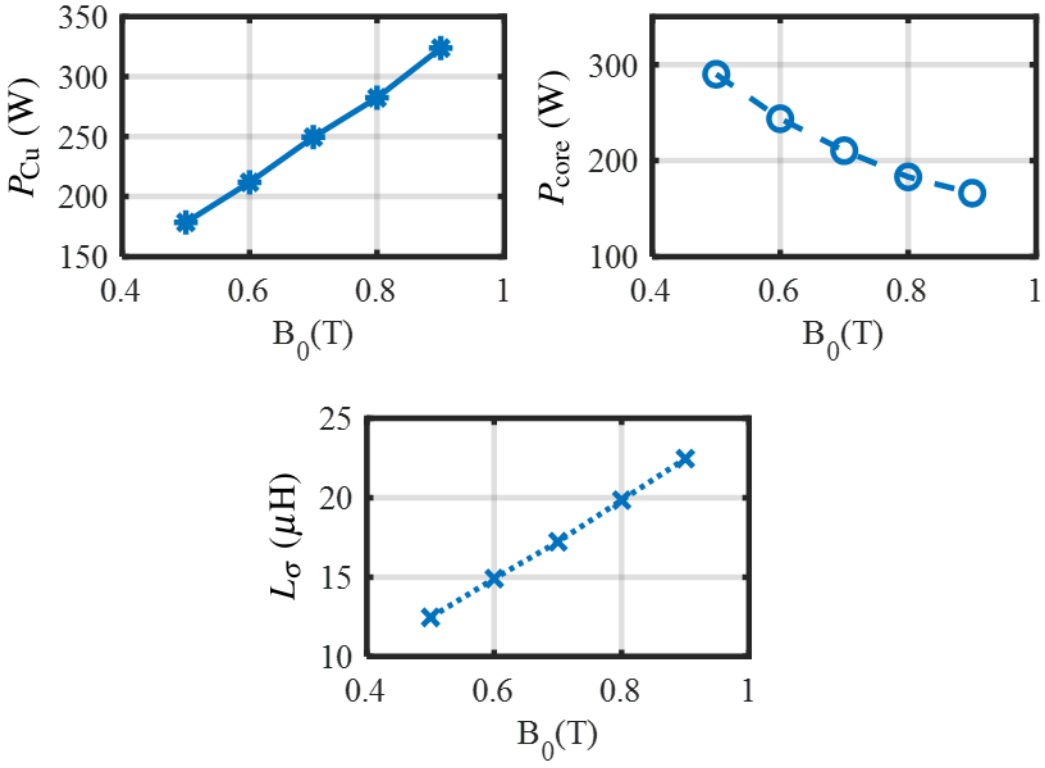
The parameter sweeps show that the analytical design variables affect both the RT geometry and the calculated electromagnetic response. These dependencies are retained when the candidate MW-class geometries are examined in Section 4.4.

Table 4.9 Definition of the intermediate-scale RT sensitivity study

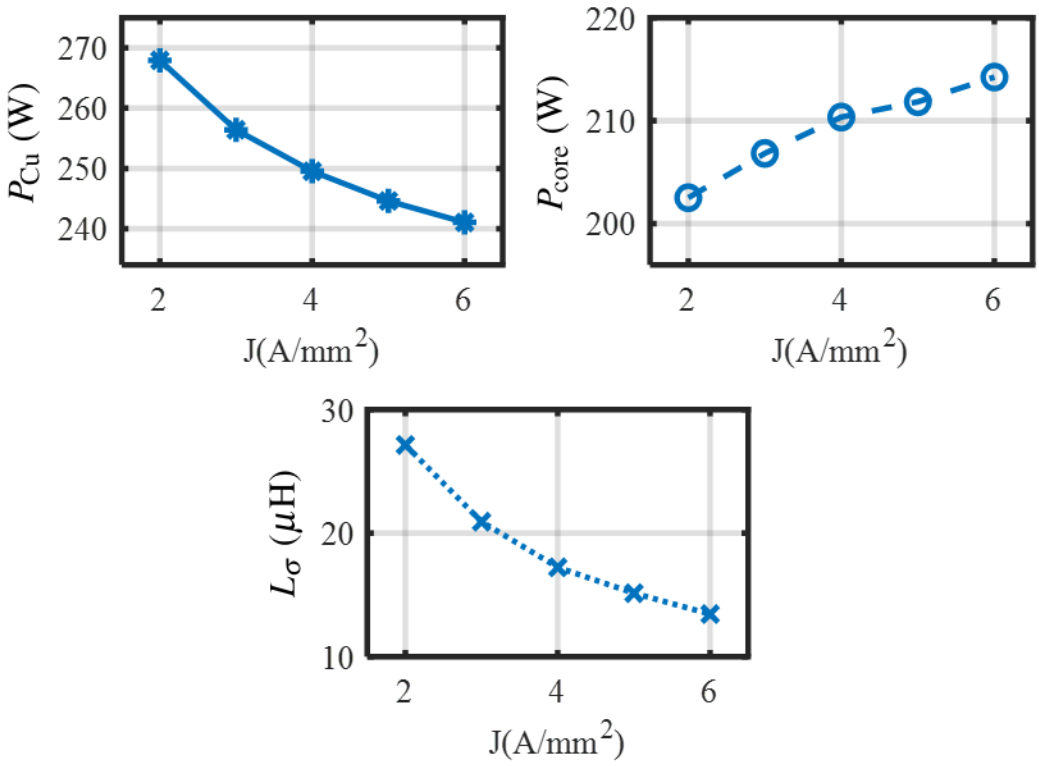
Design variable	Investigated range	Nominal value	Change represented in the study
Core-to-core airgap, g_{c}	1-5mm	1mm	g_c varied directly, magnetic coupling, leakage and loss quantities recalculated
Design flux-density target, B_0	$0.5 - 0.9T$	$0.7T$	Core cross-sectional area and dependent geometry recalculated
Current density, J	$2 - 6\ A/mm^2$	$4\ A/mm^2$	Required conductor area and dependent winding dimensions recalculated
Winding window width, b_w	approximately 15.3-16.1mm	15.91 mm	Winding geometry and mean conductor path changed



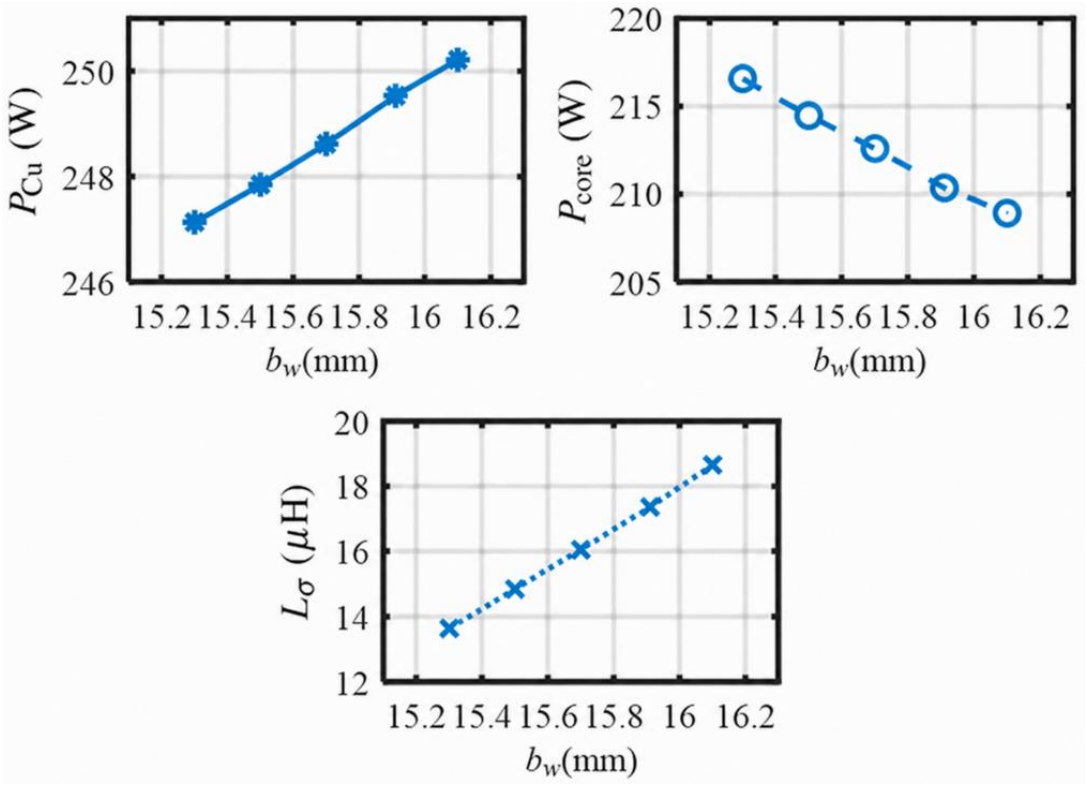
(a) Core-to-core airgap g_c



(b) Design flux density target B_0



(c) Current density J



(d) Winding window width b_w

Figure 4.11 Effects of the investigated RT design variables on P_{Cu}, P_{core} and L_σ

4.4 MW-Class Linked Field-Circuit Analysis of the Candidate Rotary Transformers

Section 4.3 examines the 600 V/100 kW RT using analytical and finite-element models. This section considers the five candidate RT geometries within the three-phase MW-class RT-DAB linked field-circuit model. The original radial, NEW1, NEW2, L type 1 and L type 2 structures are coupled to the same converter circuit so that their electrical and magnetic responses can be compared under common converter commands.

The core geometries are compared first in terms of transferred power, current, RT terminal voltage and magnetic-flux-density distribution. The effects of primary-to-secondary winding separation and winding fill factor are then examined under separately defined conditions. The final numerical study changes the winding turns ratio of the selected geometry to examine voltage transformation. Section 4.4.5 relates these operating points to the variable electrical output of the X-ROTOR powertrain.

4.4.1 Numerical Model and Common Operating Conditions

The MW-class model combines a 2D transient electromagnetic representation of the RT in Ansys Maxwell with a three-phase DAB circuit implemented in Ansys Simplorer. Maxwell calculates the winding electromagnetic quantities, magnetic-field distribution and RT losses, while Simplorer represents the active bridges, DC links, external transfer inductance and phase-shift control. The electromagnetic and circuit models are solved together during the transient simulation.

The original radial, NEW1, NEW2, L type 1 and L type 2 RTs are connected to the same external converter circuit. The switching frequency, baseline winding turns, phase-shift sequence and post-processing procedure are retained for the topology comparison. The different core geometries retain their corresponding magnetic paths

and winding arrangements and therefore produce different current, coupling and transferred-power responses under the same converter command.

The MW-class RT design uses a nominal transferred-power requirement of 1 MW at 2 kHz. The analytical magnetic sizing in Chapter 3 uses a winding design voltage of 1.8 kV RMS, an analytical design flux density of 1.7 T and a baseline winding fill factor of 0.60. The baseline winding arrangement uses $N_p = N_s = 24$, corresponding to $n_t = 1$. The linked circuit quantities and numerical settings are listed separately in Table 4.10, while the analytical and geometrical parameters used to construct the RT models are given in Table 4.11.

Each phase-shift command is maintained for 3ms, corresponding to six switching cycles at 2 kHz. The electrical and loss quantities are calculated from the final four complete cycles after the response immediately following the command change is excluded. The same procedure is applied to each candidate geometry. Table 4.12 gives the phase-shift sequence and the corresponding averaging intervals.

The input and output powers are obtained from the linked simulation and vary with phase-shift angle and RT geometry. The nominal 1 MW requirement therefore defines the design scale of the RT-DAB stage rather than the power obtained at every simulated operating point.

The winding loss, P_{Cu}, is obtained from the Maxwell Stranded Loss output. Under the stranded-winding representation, the current density is uniform over the equivalent conductor region and conductor-level skin and proximity effects are not resolved. The core loss, P_{core}, is obtained from the material-loss model assigned to the M250-35A core. These RT loss quantities are considered separately from the DC port powers calculated by the linked circuit.

The phase-shift commands and the corresponding post-processing intervals are given in Table 4.12. Each command is maintained for 3 ms, corresponding to six switching cycles at 2 kHz. The final four complete cycles are used to calculate the RMS electrical quantities, mean DC port powers and RT losses after the initial response to each command change is excluded.

Table 4.10 Operating and model settings of MW-class linked field-circuit simulation

Category	Symbol	Parameter	Value/model setting
System	$V_{dc,p}$	Primary DC link voltage	1800 V
	$V_{dc,s}$	Secondary DC link voltage	1800 V
Converter		Converter configuration	Three-phase DAB
	f_s	Switching frequency	2 kHz
	T_s	Switching period	0.5 ms
DC link	$C_{dc,p}, C_{dc,s}$	Primary and secondary side capacitance	20μF
Transfer branch	L_{ext}	External transfer inductance	110μH
	R_{ext}	Assigned series resistance	1×10^{-6} Ω
Semiconductor model	$V_{f,IGBT}$	IGBT forward voltage drop	1.7 V
	$V_{f,D}$	Diode forward voltage drop	1 V
DCside circuit	$R_{dc,p}$	Protective slide rheostats on primary DC side	0.01 Ω
	$R_{dc,s}$	Protective slide rheostats on secondary DC side	0.05 Ω
FEM		Electromagnetic formulation	Maxwell 2D transient
Circuit model		External circuit environment	Ansys Simplorer
Winding model		Winding representation	Stranded
Magnetic material		Core material	M250-35A electrical steel
FEM	d_{2D}	Active model depth	455 mm
	Δt	Transient time step	1 μs

Table 4.11 Analytical and geometrical reference parameters of the MW-class RT

Parameter	Symbol	Value
Nominal transferred-power requirement	P_{nom}	1 MW
Design winding voltage	V_{rms}	1.8 kV RMS
Analytical design flux density	B_{design}	1.7 T
Baseline winding fill factor	$k_{f,design}$	0.6
Current density	J	2 A/mm^2
Window aspect ratio	α	3.9
Shaft radius	R_{shaft}	100 mm
Primary turns	N_p	24
Secondary turns	N_s	24
Nominal turns ratio	$n_t = N_p/N_s$	1
Power to-voltage current base	I_{base}	555.56 A
Minimum core cross-sectional area	A_c	4894.16 mm^2
Winding window area	A_w	24169.7 mm^2
Baseline effective copper occupation	$A_{Cu,design}$	14501.8 mm^2
Window length	h_w	209.73 mm
Window width	b_w	53.78 mm
Core-to-core magnetic airgap	g_c	5 mm
Winding-to-winding separation	δ_w	5 mm
Core width	w_c	7.789 mm
Equivalent conductor diameter	$d_{c,eq}$	18.806 mm
Copper resistivity	ρ_{Cu}	1.72×10^{-8} Ωm

Table 4.12 Phase-shift sequence and steady-state post-processing intervals

Phase shift command φ	Command interval	Number of switching cycles	Excluded transition interval	Steady-state averaging interval	Number of averaged cycles
$10°$	$0-3$ ms	6	$0-1$ ms	$1-3$ ms	4
$30°$	$3-6$ ms	6	$3-4$ ms	$4-6$ ms	4
$50°$	$6-9$ ms	6	$6-7$ ms	$7-9$ ms	4
$70°$	$9-12$ ms	6	$9-10$ ms	$10-12$ ms	4
$90°$	$12-15$ ms	6	$12-13$ ms	$13-15$ ms	4

The same averaging intervals are used for all five RT geometries. The RMS voltages and currents, mean DC port powers, Maxwell Stranded Loss and Maxwell Core Loss are calculated over the final four complete switching cycles of each phase-shift interval.

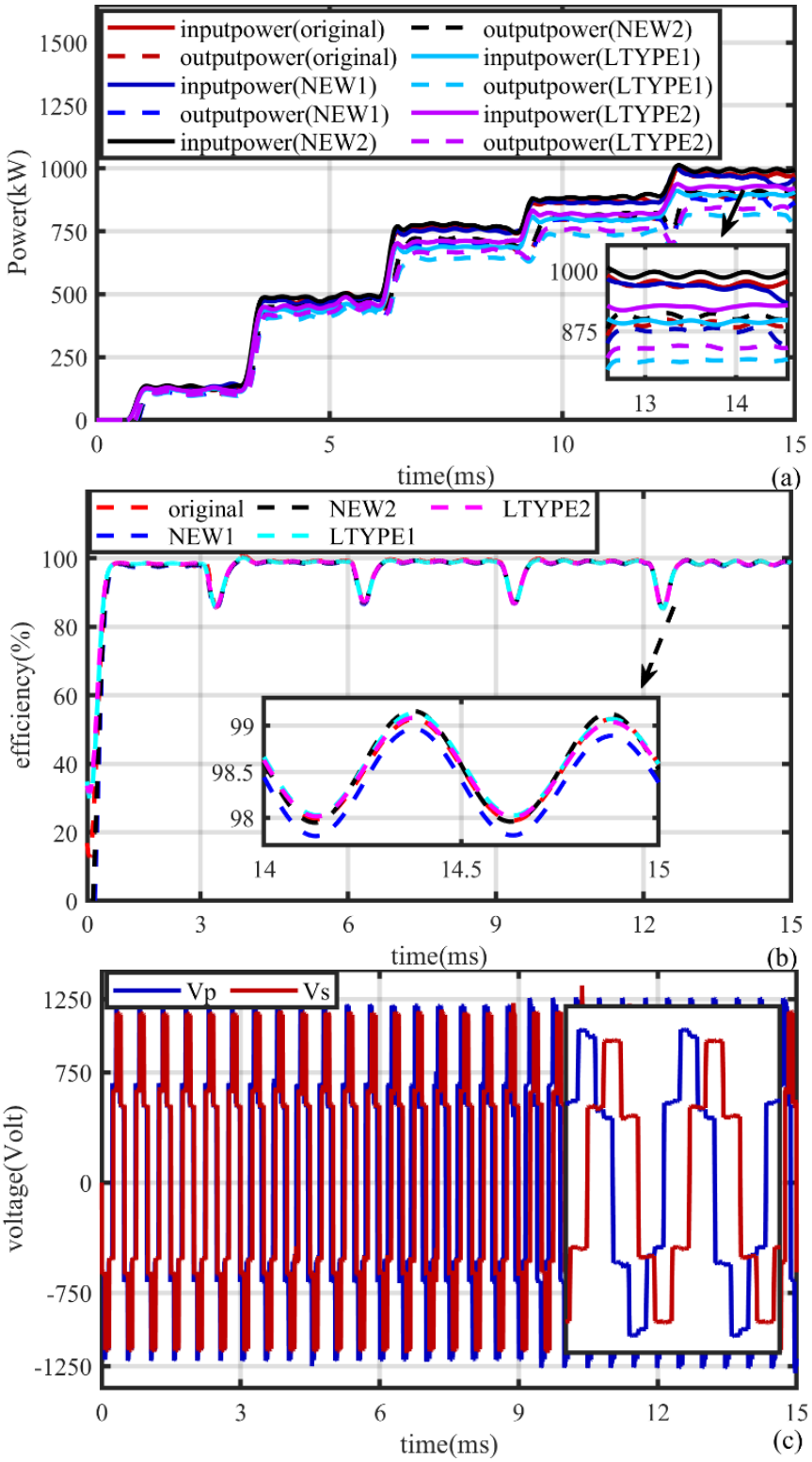
4.4.2 Comparison of Candidate RT Geometries

The original radial, NEW1, NEW2, L type 1 and L type 2 RT geometries are evaluated using the linked field-circuit model described in Section 4.4.1. Each RT is connected to the same three-phase DAB circuit and is subjected to the phase-shift sequence defined in Table 4.12. The linked Maxwell-Simplorer arrangements for the five RT models are provided in Appendix A.

Figure 4.12 compares the input and output DC port powers, power transfer efficiency, RT terminal voltages and transfer-path current obtained for the five geometries. The phase-shift command is common to all cases, while the current and transferred power are determined by the corresponding RT electromagnetic parameters.

The input and output powers increase as the phase shift is increased. This follows the SPS operating relationship described in Chapter 3: a larger displacement between the primary- and secondary-side bridge voltages changes the voltage applied across the effective transfer inductance and increases the transferred power. The five geometries do not produce identical power at the same phase-shift command because their

magnetic paths and winding arrangements give different coupling and leakage characteristics.



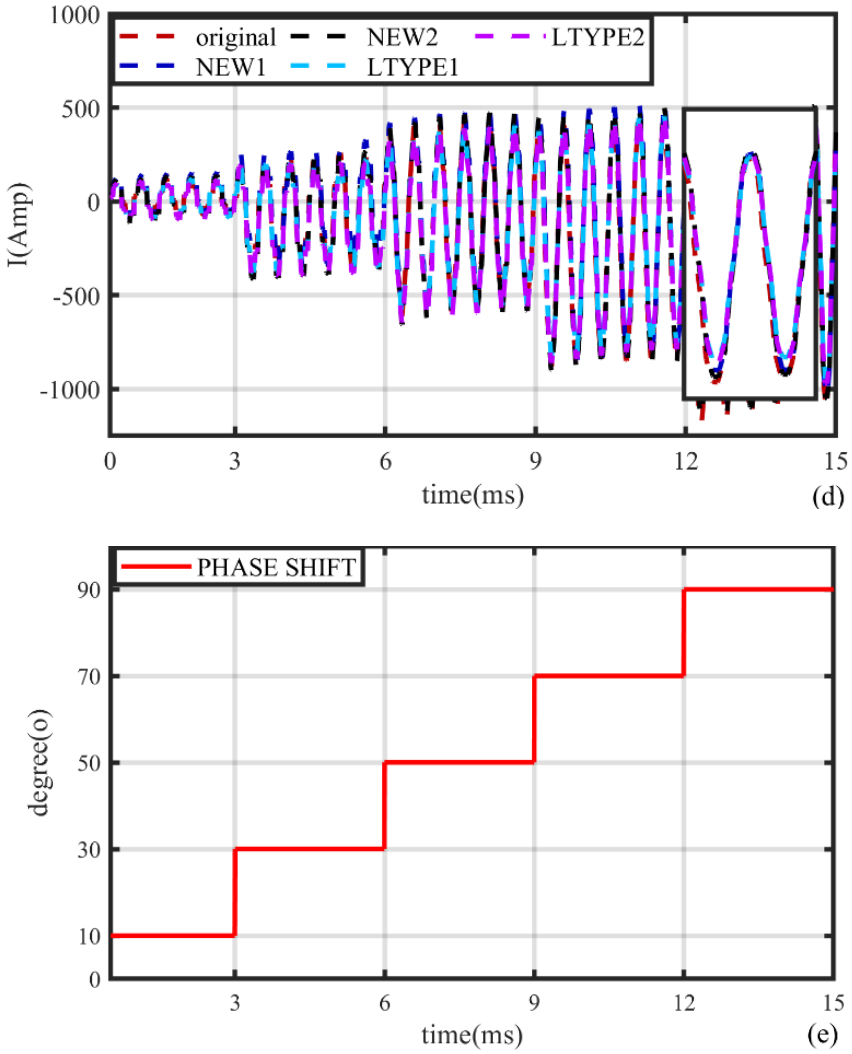
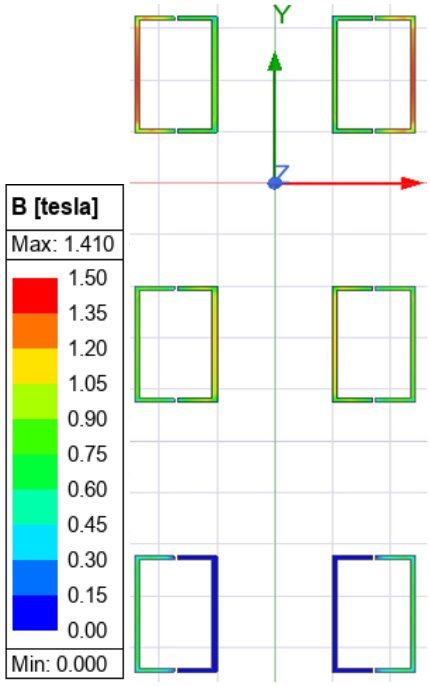


Figure 4.12 Electrical responses of the candidate RT geometries in the three-phase RT-DAB model: (a) input and output powers, (b) power transfer efficiency, (c) primary and secondary side RT terminal voltages, (d) transfer inductance current and (e) phase shift command

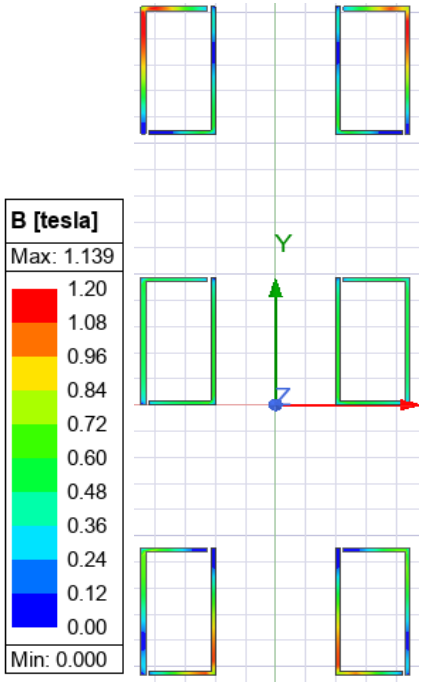
The current responses in Figure 4.12(d) show the same dependence on RT geometry. The transfer-path current increases with electrical loading, while its magnitude and waveform differ among the five structures. These current differences are considered together with the winding-loss results in Section 4.4.3, since P_{Cu} depends on both winding resistance and RMS current.

Figure 4.12(b) shows the corresponding power transfer efficiencies. The short changes following each phase-shift transition are associated with the transient response of the linked circuit. The steady-state comparison uses the averaging intervals defined in Table 4.12 rather than the transition periods.

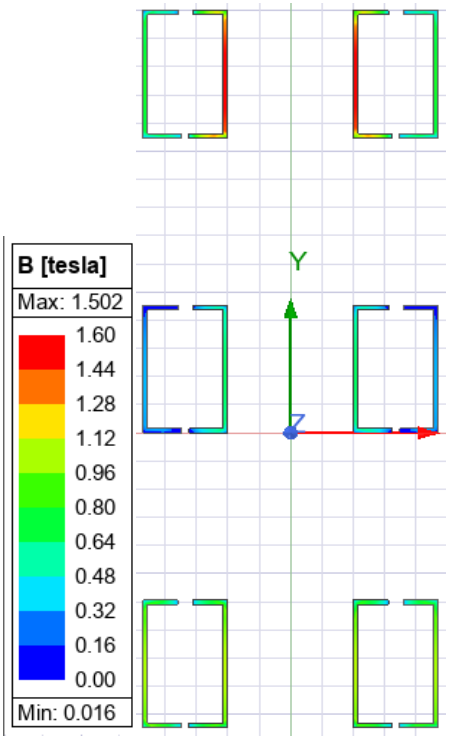
The primary and secondary-side RT terminal voltages in Figure 4.12(c) retain the imposed switching frequency and phase displacement for all five models. Differences in transferred power and current therefore arise from the interaction between the common converter circuit and the electromagnetic characteristics of each RT geometry.



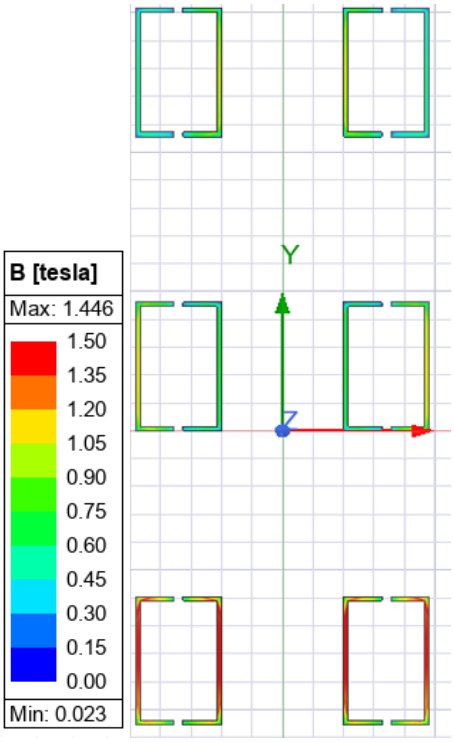
(a) Original radial type



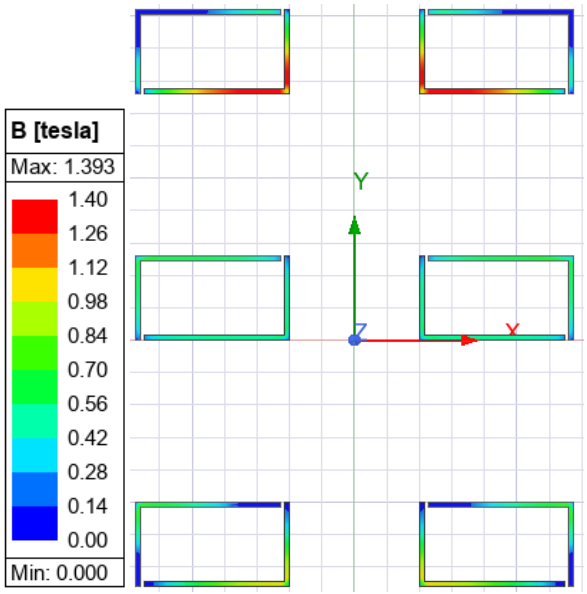
(b) L-type 2



(c) NEW1



(d) NEW2



(e) L-type 1

Figure 4.13 Magnetic flux density distributions of the candidate RT geometries

These field distributions are considered together with the winding and core-loss results in Section 4.4.3.

4.4.3 Effects of Winding Separation and Winding Fill Factor on RT Losses

The candidate RT geometries in Section 4.4.2 are compared further by varying two winding parameters: the primary-to-secondary winding separation, δ_w, and the winding fill factor, k_f. These parameters affect RT in different ways. Changing s_w changes the relative position of the two winding regions and therefore alters magnetic coupling and leakage, whereas changing k_f within a fixed winding window changes the effective copper area and winding resistance.

The topology-specific core-to-core magnetic gaps, g_c, remain unchanged throughout both studies. The original radial, L type 1 and L type 2 structures retain their 5 mm core gaps, NEW1 retains its 15 mm and 5 mm upper and lower core gaps, and NEW2 retains its 15 mm core gap. The 5, 10 and 15 mm values examined in Section 4.4.3.2 therefore refer only to δ_w, not to g_c.

The same converter circuit, switching frequency, winding turns and phase-shift sequence defined in Section 4.4.1 are used throughout. The resulting current and transferred power are allowed to change with the winding parameter under investigation.

4.4.3.1 Definition of the Parameter Studies

The investigated cases are summarized in Table 4.13. The reference configuration of each topology employs a winding-to-winding separation of $\delta_w = 5mm$ and a winding fill factor of $k_f = 0.60$.

In the winding-separation study, δ_w is varied from 5 mm to 10 mm and 15 mm. The winding cross-sectional dimensions, winding window, fill factor, number of turns, topology-specific core gaps, magnetic material and converter settings remain unchanged. The three cases therefore differ only in the relative positions of the primary and secondary winding regions.

In the fill-factor study, $\delta_w = 5$ mm is retained and $k_f$is varied from 0.60 to 0.40 and 0.28. The winding window, winding positions, number of turns, core geometry and magnetic material remain unchanged, while the effective copper area within the winding window is changed.

The phase-shift sequence defined in Table 4.12 is applied to each case. The resulting winding currents and transferred powers are obtained directly from the linked field-circuit simulation and are allowed to vary with the parameter under investigation.

Table 4.13 Definition of the MW-class winding-separation and fixed-window fill-factor studies

Study	Varied parameter	Investigated values	Quantities retained
Reference configurations	None	$\delta_w = 5$ mm, $k_f = 0.6$	Topology-specific core and winding geometry, $N_p = N_s = 24$, magnetic material and converter settings
Winding separation	δ_w	5,10,15 mm	Winding cross-sections, winding window, $k_f = 0.60$, $N_p = N_s = 24$,

			topology-specific g_c, magnetic material and converter settings
Winding fill factor	k_f	0.28, 0.4 and 0.6	$\delta_w = 5$ mm, fixed winding window and winding positions, $N_p = N_s = 24$, topology-specific g_c, magnetic material and converter settings

4.4.3.2 Effect of Winding Separation

The effect of winding separation is examined by increasing δ_w from 5 mm to 10 mm and 15 mm for each candidate RT geometry. The remaining winding and converter conditions are those defined in Section 4.4.3.1.

Figure 4.14 the resulting three-phase winding loss, P_{Cu}. For all five geometries, the winding loss increases with phase-shift angle. At a given phase-shift command, however, a larger winding separation generally gives a lower absolute winding loss. For example, at the highest phase-shift command, P_{Cu} decreases from 1.7865 kW to 1.0309 kW for NEW2 and from 1.4639 kW to 0.5517 kW for L type 2 as $s_w$is increased from 5 mm to 15 mm.

Since the conductor dimensions are unchanged within each topology-specific series, the reduction in winding loss is not caused by a reduction in winding resistance. It is associated mainly with the lower winding current produced as the magnetic coupling between the two windings is reduced.

Figure 4.15 shows the corresponding core-loss results. Unlike the winding loss, P_{core} does not follow the same monotonic trend for all five geometries. For the original radial geometry, the core loss decreases from 9.9323 kW at $\delta_w = 5$ mm to 9.2600 kW at 15 mm, while L type 2 decreases from 12.0120 kW to 10.7906 kW. NEW1 and NEW2 give their lowest values at $\delta_w = 10$ mm, with 9.0133 kW and 8.3089 kW, respectively. L type 1 instead increases from 11.2336 kW at 5 mm to 12.1304 kW at 15 mm.

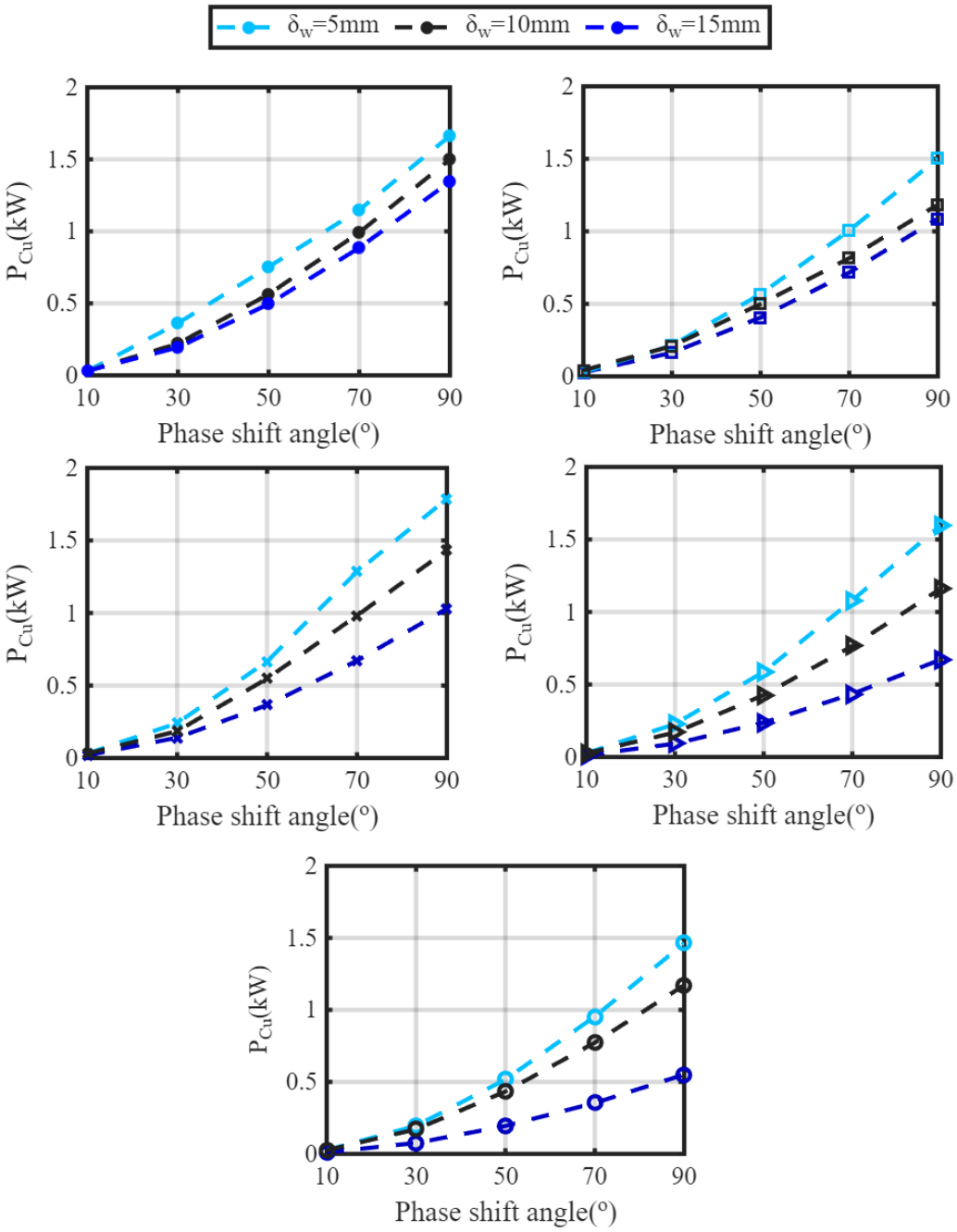


Figure 4.14 Simulated three-phase winding loss, P_{Cu}, as a function of phase-shift angle and winding-to-winding separation: (a) Original radial, (b) NEW1, (c) NEW2, (d) L-type 1 and (e) L-type 2

The variation in core loss reflects the change in leakage-field distribution and magnetic excitation as the winding positions are changed. Because the magnetic paths differ between the five RT structures, the effect of $s_w$on P_{core} is geometry dependent.

The corresponding electrical quantities are summarised in Table 4.14 summarises the corresponding electrical and loss quantities. The coupling factor decreases as δ_w is

increased for every candidate geometry. Between 5 mm and 15 mm, $k$decreases from 0.9562 to 0.9142 for the original radial geometry, from 0.9443 to 0.8836 for NEW1, from 0.9391 to 0.9084 for NEW2, from 0.9580 to 0.9132 for L type 1 and from 0.9566 to 0.9123 for L type 2.

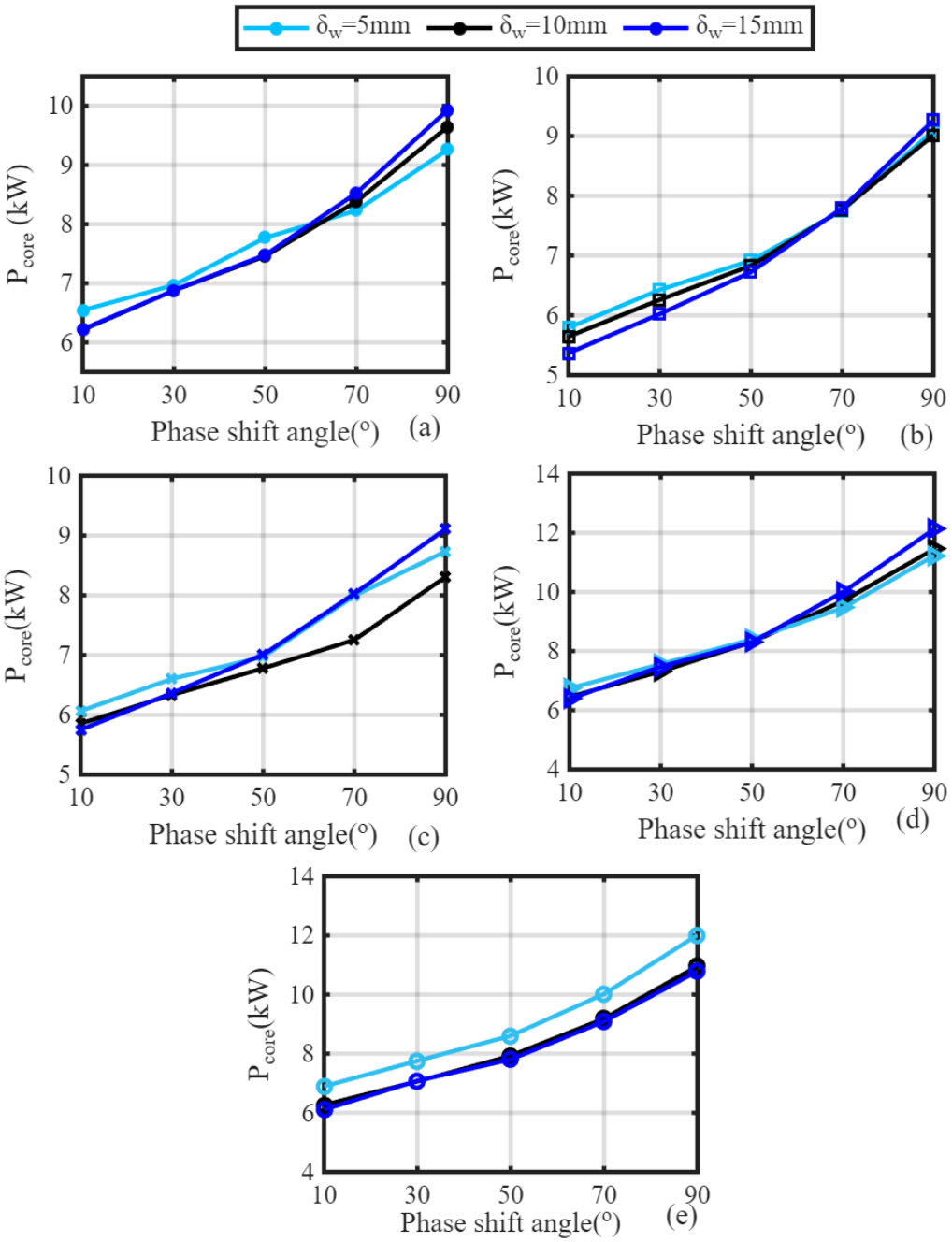


Figure 4.15 Simulated three-phase core loss, P_{core}, for different winding separations: (a) Original radial, (b) NEW1, (c) NEW2, (d) L-type 1 and (e) L-type 2.

The reduction in coupling is accompanied by lower winding current and transferred power. For NEW2, for example, P_{out} decreases from 991.3189 kW at $\delta_w = 5\text{mm}$ to

843.9418 kW at 15 mm. The lower absolute winding loss at larger separation therefore occurs at a lower electrical loading.

Increasing δ_w reduces the coupling factor and transferred power for all five geometries. Although the absolute winding loss is generally lower at larger separations, this reduction is accompanied by lower winding current and electrical loading. The 5 mm winding separation is therefore retained as the reference condition for the fill-factor study in Section 4.4.3.3.

Table 4.14 Mean per-phase coupling factor, electrical loading, DCport powers and RT loss components for the winding-separation study at phase shift angle $= 90°$.

Topology	δ_w (mm)	$I_{p/s,3\emptyset,rms}$ (A)	$k_{\mathrm{ps,ph}}$	P_{in} (kW)	P_{out} (kW)	P_{Cu} (kW)	P_{core} (kW)
Original	5	$\frac{619.262}{599.396}$	0.956	983.279	969.448	1.662	9.932
	10	$\frac{578.728}{569.338}$	0.935	902.600	888.679	1.499	9.647
	15	$\frac{544.879}{540.797}$	0.914	840.025	826.487	1.345	9.260
NEW1	5	$\frac{585.032}{543.679}$	0.944	932.253	919.498	1.508	9.088
	10	$\frac{553.111}{535.654}$	0.903	847.441	833.643	1.184	9.013
	15	$\frac{527.394}{524.282}$	0.883	782.516	770.603	1.087	9.263
NEW2	5	$\frac{709.873}{634.303}$	0.939	1005.672	991.318	1.786	8.736
	10	$\frac{595.397}{549.675}$	0.924	929.061	913.110	1.434	8.308
	15	$\frac{583.221}{561.171}$	0.908	858.337	843.941	1.030	9.110
L-type 1	5	$\frac{608.253}{595.301}$	0.958	946.070	932.878	1.598	11.233
	10	$\frac{549.379}{547.848}$	0.934	857.296	844.367	1.161	11.456
	15	$\frac{509.785}{506.951}$	0.913	782.004	769.165	0.672	12.130
L-type 2	5	$\frac{571.105}{570.180}$	0.956	904.917	892.031	1.463	12.012
	10	$\frac{539.401}{532.644}$	0.927	837.924	824.831	1.172	10.958
	15	$\frac{512.129}{509.661}$	0.912	785.880	772.997	0.551	10.790

4.4.3.3 Effect of Winding Fill Factor

The fill-factor study retains the reference winding separation of $\delta_w = 5\text{mm}$. For each candidate RT geometry, the winding window dimensions, winding positions, number of turns, topology-specific core gaps and magnetic material remain unchanged. The winding fill factor, k_f, is varied by changing the effective copper area within the existing winding window. Following the definitions introduced in Chapter 3, $A_{\text{Cu}} = k_f A_w$, and the equivalent conductor area per turn is $a_{\text{Cu}} = \frac{A_{\text{Cu}}}{N}$. The investigated values are $k_f = 0.60, 0.40$ and 0.28. Table 4.15 gives the corresponding winding window and copper areas for the five RT geometries.

Table 4.15 Fixed winding window and copper areas used in the fill-factor study

Topology	k_f	Fixed A_w (mm^2)	A_{Cu} (mm^2)	Equivalent conductor area per turn $a_{\text{Cu}} = \frac{A_{\text{Cu}}}{N}$ (mm^2)
Original	0.60	14157.310	8494.386	353.932
	0.40	14157.310	5662.924	235.955
	0.28	14157.310	3964.046	165.168
NEW 1	0.60	14280.350	8568.221	357.009
	0.40	14280.350	5712.14	238.005
	0.28	14280.350	3998.498	166.604
NEW 2	0.60	14594.566	8756.740	364.864
	0.40	14594.566	5837.826	243.242
	0.28	14594.566	4086.478	170.269
L-type 1	0.60	14157.310	8494.386	353.932
	0.40	14157.310	5662.924	235.955
	0.28	14157.310	3964.046	165.168
L-type 2	0.60	14157.310	8494.386	353.932

	0.40	14157.310	5662.924	235.955
	0.28	14157.310	3964.046	165.168

The winding window area remains constant within each topology-specific series. Reducing k_f from 0.60 to 0.28 reduces the effective copper area by approximately 53.3%. With the conductor material, number of turns and winding geometry otherwise unchanged, the smaller conductor area increases the winding resistance. The resulting winding loss also depends on the current established by the linked field-circuit model.

Figure 4.16 shows the winding-loss response over the phase-shift sequence. For each candidate geometry, P_{Cu} increases as k_f is reduced. At the highest phase-shift command, reducing k_f from 0.60 to 0.28 increases P_{Cu} from 1.6626 kW to 3.7940 kW for the original radial geometry, from 1.5080 kW to 4.4251 kW for NEW1, from 1.7865 kW to 3.8646 kW for NEW2, from 1.5982 kW to 3.7691 kW for L type 1, and from 1.4639 kW to 3.2491 kW for L type 2.

The winding loss increases with phase-shift angle for every candidate geometry, reflecting the increase in electrical loading as the displacement between the converter bridge voltages is raised. At each phase shift command, reducing k_f shifts the winding-loss curve upwards. The separation between the three curves becomes more pronounced at the higher phase-shift angles because the increased winding resistance is combined with the larger current associated with the higher-power operating points.

At $\delta = 90°$, reducing k_f from 0.60 to 0.28 increases P_{Cu} from 1.6626 kW to 3.7940 kW for the original radial geometry, from 1.5080 kW to 4.4251 kW for NEW1, from 1.7865 kW to 3.8646 kW for NEW2, from 1.5982 kW to 3.7691 kW for L-type 1, and from 1.4639 kW to 3.2491 kW for L-type 2. The same trend is obtained for all five geometries.

Table 4.16 gives the corresponding electrical, magnetic and loss quantities. Within each topology-specific series, the coupling factor and phase leakage inductance change little as k_f is varied. This is consistent with the retained winding positions, winding separation and core geometry.

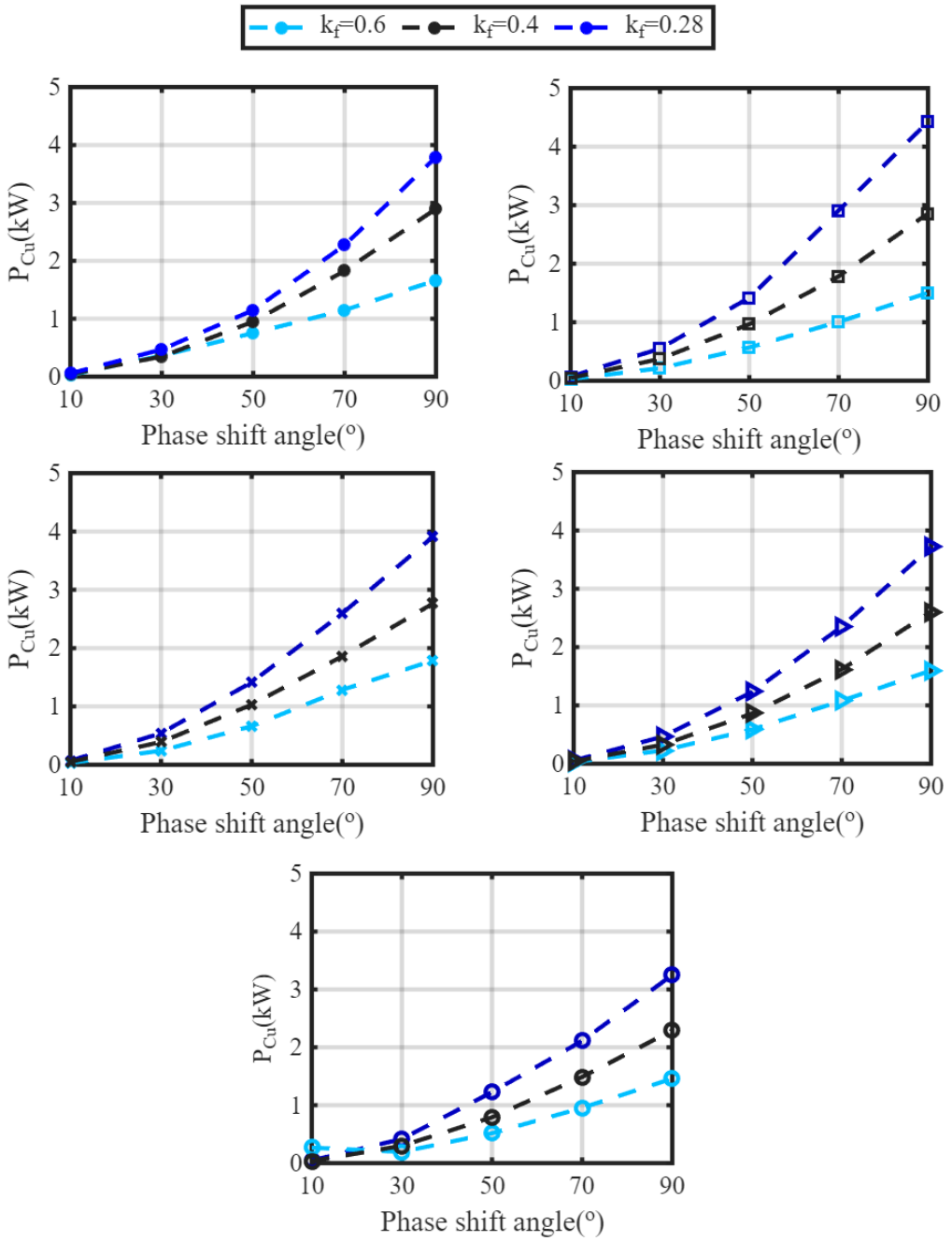


Figure 4.16 Simulated winding loss P_{Cu} for $k_f = 0.60{,}0.40\ and\ 0.28$ under the fixed winding window condition: (a) original radial type, (b) NEW1, (c) NEW2, (d) L-type 1 and (e) L-type 2.

The winding currents do not show the same monotonic dependence on k_f as the winding loss. NEW2 provides a representative example. When k_f is reduced from 0.60 to 0.28, the primary RMS current decreases from 709.873 A to 653.589 A, while the secondary RMS current changes from 634.303 A to 643.369 A. Over the same range, P_{out} changes from 991.3189 kW to 983.9241 kW, whereas P_{Cu} increases from 1.7865

kW to 3.8646 kW. The increase in P_{Cu} is therefore dominated by the reduced conductor area and the corresponding increase in winding resistance, rather than by an increase in RMS current.

Table 4.16 Representative electrical, magnetic and loss quantities for the fixed-window fill factor study at phase shift angle $= 90°$

Topology	k_f	$I_{p/s,3\emptyset,rms}$ (A)	$\bar{L}_{\sigma,ph}$ (μH)	k	P_{in} (kW)	P_{out} (kW)	P_{Cu} (kW)	P_{core} (kW)
Original	0.60	$\frac{619.262}{599.396}$	40.383	0.956	983.279	969.448	1.662	9.932
	0.40	$\frac{680.612}{625.947}$	40.429	0.956	988.134	976.243	2.898	9.662
	0.28	$\frac{632.340}{615.125}$	40.430	0.953	987.019	975.565	3.794	9.455
NEW 1	0.60	$\frac{585.032}{543.679}$	39.732	0.944	932.253	919.498	1.508	9.088
	0.40	$\frac{685.721}{654.885}$	39.269	0.944	1015.394	985.086	2.858	8.516
	0.28	$\frac{682.467}{668.964}$	39.258	0.944	1003.750	990.847	4.425	8.736
NEW 2	0.60	$\frac{709.873}{634.303}$	38.371	0.939	1005.672	991.318	1.786	8.736
	0.40	$\frac{656.824}{653.004}$	38.368	0.939	1007.249	989.402	2.765	8.821
	0.28	$\frac{653.589}{643.369}$	38.371	0.939	1009.236	983.924	3.864	8.987
L-type 1	0.60	$\frac{608.253}{595.301}$	44.206	0.958	946.070	932.878	1.598	11.233
	0.40	$\frac{620.365}{600.971}$	44.195	0.958	946.198	932.586	2.605	12.058
	0.28	$\frac{648.557}{615.830}$	44.195	0.957	944.818	937.352	3.769	11.298
L-type 2	0.60	$\frac{571.105}{570.180}$	47.119	0.956	904.917	892.031	1.463	12.012
	0.40	$\frac{588.914}{587.759}$	48.852	0.956	906.978	890.996	2.291	11.740
	0.28	$\frac{586.708}{585.375}$	48.850	0.956	907.936	890.079	3.249	11.8066

The core loss does not follow the same monotonic trend as the winding loss. The original radial and NEW1 geometries show modest reductions in P_{core} as k_f is reduced, while NEW2 and L type 1 show small increases, L type 2 varies only slightly. Since the

core geometry and winding positions are retained, these changes arise from the different current and magnetic excitation produced by the linked circuit rather than from a change in the magnetic path itself.

The combined represented RT loss, $P_{\mathrm{Cu}} + P_{\mathrm{core}}$, increases for all five geometries as k_f is reduced from 0.60 to 0.28. These quantities refer only to the Maxwell winding- and core-loss outputs and are not the DC to DC efficiency of the complete RT-DAB stage.

Within the fixed-window stranded-winding model, $k_f = 0.60$ gives the lowest represented RT loss of the three investigated fill factors. This value is retained for the subsequent reference case. Strand-level AC effects, insulation requirements and thermal constraints are not included in the present fill-factor comparison.

4.4.3.4 Design Implications

The winding-separation study shows that increasing δ_w reduces the magnetic coupling, winding current and transferred power under the same phase-shift command. The lower winding loss obtained at the larger separations therefore occurs together with a reduction in electrical loading. For the subsequent comparisons, $\delta_w = 5\,\mathrm{mm}$ is retained as the reference winding separation because it gives the highest coupling and transferred power within each topology-specific separation series. The topology-specific core-to-core magnetic gaps, g_c, remain unchanged.

For the fixed-window fill-factor study, reducing k_f decreases the effective copper area and increases the represented winding resistance. Consequently, P_{Cu} increases for all five candidate geometries as k_f is reduced from 0.60 to 0.28. Although the associated current and core-loss responses vary slightly with topology, the combined represented RT loss, $P_{\mathrm{Cu}} + P_{\mathrm{core}}$, is lowest at $k_f = 0.60$ in each of the investigated fill-factor series. This value is therefore retained for the subsequent assessment. The choice applies to the present fixed-window stranded-winding model, strand-level AC effects and the practical thermal, insulation and manufacturing constraints associated with the winding arrangement are outside the scope of this comparison.

Using the retained conditions of $\delta_w = 5\text{mm}$, $k_f = 0.60$, $N_p = N_s = 24$and $\varphi = 90°$, NEW2 produces an output power of 991.3189 kW, the closest of the five candidate geometries to the nominal 1 MW requirement. Its winding and core losses are 1.7865 kW and 8.7362 kW, respectively, giving a combined represented RT loss of 10.5227 kW, or approximately 1.06% of the corresponding output power. This is also the lowest combined winding-and-core loss among the five reference cases. Although NEW2 does not have the lowest individual winding loss, its combination of transferred power and represented RT loss makes it the preferred candidate within the investigated design set.

NEW2 is therefore retained for the voltage-transformation study in Section 4.4.4. The reference magnetic geometry and winding-position boundary are maintained, while the primary-to-secondary turns arrangement is changed to examine the resulting RT voltage ratio.

4.4.4 Effect of Winding Turns Ratio on Voltage Transformation

The NEW2 geometry retained in Section 4.4.3.4 is used to examine the voltage-transformation capability of the RT. The primary winding is fixed at $N_p = 24$ turns, while two secondary winding arrangements are considered: $N_s = 24$ and $N_s = 48$. The magnetic geometry, winding-position boundary and remaining linked field-circuit conditions are retained between the two cases. The turns ratio defined in Chapter 3 is $n_t = \frac{N_p}{N_s}$, and the simulated terminal-voltage ratio is evaluated in the secondary-to-primary direction as

$$r_v = \frac{V_{s,\text{rms}}}{V_{p,\text{rms}}} \tag{4.8}$$

For which the ideal transformer relationship is

$$r_{v,\text{ideal}} = \frac{N_s}{N_p} = \frac{1}{n_t} \tag{4.9}$$

The corresponding voltage-ratio error is evaluated from

$$\varepsilon_v = \frac{r_v - r_{v,\text{ideal}}}{r_{v,\text{ideal}}} \times 100\% \tag{4.10}$$

Figure 4.17 shows the simulated primary- and secondary-side RT AC-terminal voltages for the two winding arrangements. With $N_p = N_s = 24$, the primary and secondary voltage magnitudes remain closely matched. Doubling the secondary turns to $N_s = 48$ approximately doubles the secondary terminal voltage while retaining the switched waveform characteristic of the linked RT-DAB model.

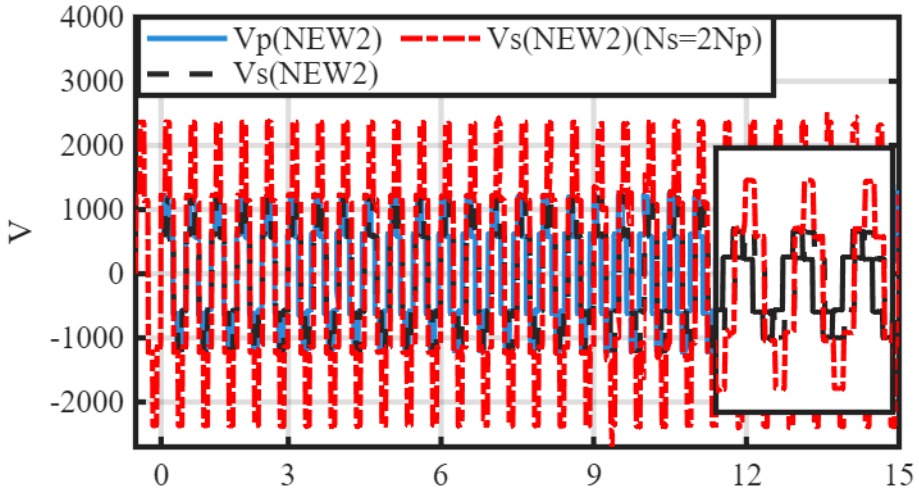


Figure 4.17 Simulated primary and secondary-side RT AC-terminal voltage waveforms of the NEW2 geometry for the $N_p : N_s = 24:24$ and $24:48$ winding arrangements.

The RMS quantities obtained from the periodic waveforms are summarised in Table 4.17.

Table 4.17 Simulated RT AC-terminal RMS voltage ratios of the selected NEW2 geometry for the investigated turns arrangements

Turns arrangment $\frac{N_p}{N_s}$	$V_{p,rms}$	$V_{s,rms}$	$r_v = \frac{V_{s,rms}}{V_{p,rms}}$	$r_{v,ideal} = \frac{N_s}{N_p}$	ε_v (%)
24: 24	1709.2	1678.1	0.981	1	-1.90
24: 48	1716.5	3364.7	1.959	2	-2.05

For the $24:24$ arrangement, the simulated RMS voltage ratio is 0.981, compared with the ideal value of 1. Increasing the secondary winding to 48 turns gives a ratio of 1.959, compared with the ideal value of 2. The deviations are therefore −1.90% and −2.05%, respectively.

The secondary terminal voltage is slightly below the ideal turns-ratio prediction in both cases. The linked model includes leakage flux, winding impedance, magnetising current and converter loading, while the reported RMS quantities are obtained from switched RT-terminal waveforms rather than from an ideal unloaded transformer. The resulting voltage ratios nevertheless remain within approximately 2.1% of the corresponding ideal values.

The numerical results therefore show that the NEW2 RT provides the expected voltage scaling when its secondary turns number is changed from 24 to 48. This assessment is limited to the electrical and electromagnetic conditions represented in the linked model, the 24: 48case does not address the insulation, thermal or manufacturing requirements of a full-scale winding. The voltage-transformation function is considered together with the variable operating requirements of the X-ROTOR powertrain in Section 4.4.5.

4.4.5 Relationship to X-ROTOR Operating Conditions

The MW-class studies in the preceding sections use discrete electrical operating points to examine the effects of RT geometry, winding parameters and DAB phase shift. In the X-ROTOR powertrain, the power available to each secondary generator channel varies with ambient wind speed and with the effective inflow experienced by the secondary rotor as the primary structure rotates. The corresponding RT-DAB power demand is therefore not constant.

As described in Chapters 1 and 2, the effective inflow at secondary rotor $i$depends on the ambient wind and the orbital motion of the rotor hub. The resulting electrical path can be written as

$$U_\infty, \theta \longrightarrow U_{\mathrm{eff},i} \longrightarrow P_{\mathrm{gen},i} \longrightarrow P^*_{dc,i} \longrightarrow \varphi^*_i \tag{4.11}$$

where U_∞ is the ambient wind speed, θ is the primary rotor azimuthal position, $P_{\mathrm{gen},i}$ is the effective inflow at secondary rotor (i), $P_{\mathrm{gen},i}$ is the corresponding generator power, $P^*_{dc,i}$ is the commanded DC power for the electrical channel, and φ^*_i is the phase-shift command applied to its DAB converter. Wind speed is therefore not mapped

directly to ϕ_i^*. The required phase shift depends on the channel power demand together with the DClink voltages, RT turns ratio, effective transfer inductance and converter operating limits.

The electrical architecture established in Chapter 2 places an active machine side converter and rotating DC link between each PMSG and the RT-DAB stage. The variable PMSG terminal voltage and electrical frequency are therefore separated from the electrical excitation of the RT-DAB stage. As secondary generator speed changes, the machine side converter regulates power into the rotating DC link within its voltage, current and modulation limits. A change in available generator power is consequently accommodated mainly through the channel current and the DAB power command rather than by requiring the RT-DAB voltage to vary directly with wind speed.

The phase-shift cases examined in Section 4.4 therefore represent discrete electrical loading conditions of the RT-DAB stage, rather than an X-ROTOR wind-speed sweep or aerodynamic power curve. The highest investigated NEW2 operating point gives $P_{\text{out}} = 991.3189$ kW, close to the nominal 1 MW requirement of the MW-class transfer stage. This value is a high power reference point of the present RT-DAB study and is distinct from the 2.5 MW project rating of each X-ROTOR secondary generator.

Table 4.18 relates the three Chapter 4 investigation levels to the operating conditions of the complete powertrain.

Table 4.18 Relationship between the Chapter 4 investigations and the variable operating conditions of the X-ROTOR powertrain

Investigation	Electrical boundary	Purpose	Relationship to X-ROTOR operation
Reduced-scale experimental platform	Common 42 V DC source, 20 kHz switching and nominal 1 mm core-to-core airgap	Experimental assessment of phase-shift-controlled transfer and RT AC-terminal behaviour	Laboratory operating case, not a scaled X-ROTOR power curve or MW-class hardware model
Intermediate-scale RT study	600 V analytical RT design at 2 kHz, with the retained single-phase FEM circuit boundary	Analytical-to-FEM assessment and 2D/3D comparison	Electromagnetic modelling case, not assigned to a specific X-ROTOR wind speed

MW-class linked field-circuit study	1 MW nominal transfer requirement, 1.8 kV RMS RT winding design basis, linked-circuit conditions and phase-shift variation	Comparison of RT geometries, winding parameters, transferred power, losses and voltage transformation	Discrete electrical loading conditions up to approximately the nominal 1 MW transfer requirement
Variable X-ROTOR operation	Wind- and azimuth-dependent generator power, converter limits and supervisory power commands	Not simulated as a complete turbine model in this thesis	Determines the time-varying power demand presented to each RT-DAB channel

The two secondary rotors may experience different effective inflows at the same instant. Their generator powers, DC link currents and RT-DAB commands may therefore differ. The associated short-term power balance depends on the machine side control, DC link capacitance and supervisory control described in Chapter 2.

A wind-energy assessment would require the RT-DAB electrical performance to be combined with the X-ROTOR power variation over wind speed and primary rotor azimuth and with a site-specific wind-speed probability distribution. If $P_{\mathrm{dc}}(U)$ denotes the mean input power presented to an RT-DAB channel at wind speed U, an energy-weighted transfer efficiency may be written as

$$\eta_{E,DAB} = \frac{\int_{U_{\mathrm{ci}}}^{U_{\mathrm{co}}} \eta_{\mathrm{RT-DAB}}\,[P_{\mathrm{dc}}(U)] P_{\mathrm{dc}}(U) f_U(U), \mathrm{d}U}{\int_{U_{\mathrm{ci}}}^{U_{\mathrm{co}}} P_{\mathrm{dc}}\,(U) f_U(U), \mathrm{d}U} \tag{4.12}$$

where $f_U(U)$ is the wind-speed probability-density function and U_{ci} and U_{co} are the cut-in and cut-out wind speeds. For the X-ROTOR, $P_{\mathrm{dc}}(U)$ would additionally require the secondary generator power to be averaged over primary rotor azimuth and mapped through the machine side converter and DC link control.

The present MW-class simulations provide discrete RT-DAB electrical operating points for such an assessment. A complete annual-energy or duty-cycle calculation would additionally require the turbine power curve, the azimuth-dependent secondary generator operating data, an RT-DAB efficiency map over the required power range and the corresponding supervisory-control strategy.

4.5 Chapter Summary

This chapter evaluates the RT-DAB design developed in Chapter 3 at three investigation levels: a reduced-scale experimental platform, an intermediate 600 V/100 kW electromagnetic model and a MW-class linked field-circuit model. The three studies address different aspects of the design and are not treated as scaled versions of one another.

The reduced-scale platform examined phase-shift-controlled contactless power transfer at 42 V, 20 kHz and a nominal 1 mm assembled core-to-core airgap. Comparison with the prototype-matched Maxwell-Simplorer model showed close correspondence in the terminal-voltage levels and the fundamental power factor trend, while the simulated current magnitude remained lower than the measured value. The additional 5, 10 and 15 mm core-airgap cases are examined numerically using the same prototype-matched model.

The intermediate RT is analytically designed for 600 V RMS/100 kW at 2 kHz and used to compare the 2D and 3D electromagnetic representations. The calculated output powers are 98.832 kW and 98.787 kW, respectively, and the terminal voltage and current quantities are also closely matched. Larger differences occur in the local flux-density and core-loss results because the 2D representation does not reproduce the complete circumferential and end-region field distribution. The 2D model is subsequently used for parameter studies with these differences considered.

The MW-class analysis compares the original radial, NEW1, NEW2, L-type 1 and L-type 2 geometries using the same three-phase DAB circuit and converter commands. Increasing the primary-to-secondary winding separation, δ_w, reduces magnetic coupling, winding current and transferred power, the associated reduction in absolute winding loss therefore occurs at a lower electrical loading. In the fixed-window study, reducing k_f decreased the effective copper area and increased the represented winding loss. The reference conditions $\delta_w = 5$ mm and $k_f = 0.60$ are retained for the final candidate comparison.

Under these conditions, NEW2 produced $P_{\text{out}} = 991.3189$ kW, with represented winding and core losses of 1.7865 kW and 8.7362 kW. Their sum corresponds to

approximately 1.06% of the output power, and NEW2 is retained as the preferred geometry within the investigated design set. For the subsequent turns-ratio assessment, the simulated secondary-to-primary RMS voltage ratios were 0.981 and 1.959 for the investigated 1:1 and 1:2 winding arrangements, respectively, remaining within approximately 2.1% of the corresponding ideal ratios.

The MW-class phase-shift cases represent discrete electrical loading conditions of the RT-DAB stage. In the X-ROTOR powertrain, the corresponding power demand depends on the secondary rotor effective inflow, generator output, machine side converter and rotating DC link. A turbine-level energy assessment would require these electrical results to be combined with the X-ROTOR operating distribution and the corresponding RT-DAB efficiency map. Chapter 5 uses the experimental and numerical results obtained here to answer the research questions and assess the contributions and limitations of the proposed RT-DAB interface.

4.6 Chapter References

[1] *W. E. Leithead, A. M. K. Amiri, A. Camciuc, L. Morgan, J. Carroll, and J. Feuchtwang, "X-Rotor, an Innovative Offshore Wind Turbine to Reduce Cost of Energy," Energies, vol. 18, no. 10, Art. no. 2549, 2025, doi: 10.3390/en18102549.*

[2] *J. Dai and D. C. Ludois, "A Survey of Wireless Power Transfer and a Critical Comparison of Inductive and Capacitive Coupling for Small Gap Applications," IEEE Transactions on Power Electronics, vol. 30, no. 11, pp. 6017-6029, 2015, doi: 10.1109/TPEL.2015.2415253.*

[3] *Z. Zhang, H. Pang, A. Georgiadis, and C. Cecati, "Wireless Power Transfer-An Overview," IEEE Transactions on Industrial Electronics, vol. 66, no. 2, pp. 1044-1058, 2019, doi: 10.1109/TIE.2018.2835378.*

[4] *R. Trevisan and A. Costanzo, "A 1-kW Contactless Energy Transfer System Based on a Rotary Transformer for Sealing Rollers," IEEE Transactions on Industrial Electronics, vol. 61, no. 11, pp. 6337-6345, 2014.*

[5] *T. Raminosoa, R. H. Wiles, and J. Wilkins, "Novel Rotary Transformer Topology With Improved Power Transfer Capability for High Speed Applications," IEEE*

Transactions on Industry Applications, vol. 56, no. 1, pp. 277-286, 2020, doi: 10.1109/TIA.2019.2955050.

[6] *R. W. A. A. De Doncker, D. M. Divan, and M. H. Kheraluwala, "A Three-Phase Soft-Switched High Power Density DC/DC Converter for High Power Applications," IEEE Transactions on Industry Applications, vol. 27, no. 1, pp. 63-73, 1991, doi: 10.1109/28.67533.*

[7] *M. N. Kheraluwala, R. W. Gascoigne, D. M. Divan, and E. D. Baumann, "Performance Characterization of a High Power Dual Active Bridge DCto-DC Converter," IEEE Transactions on Industry Applications, vol. 28, no. 6, pp. 1294-1301, 1992, doi: 10.1109/28.175280.*

[8] *B. Zhao, Q. Song, W. Liu, and Y. Sun, "Overview of Dual active bridge Isolated Bidirectional DCDC Converter for High Frequency-Link Power Conversion System," IEEE Transactions on Power Electronics, vol. 29, no. 8, pp. 4091-4106, 2014, doi: 10.1109/TPEL.2013.2289913.*

[9] *STMicroelectronics, "STEVAL-IPM30B: 2500 W motor-control power board based on the STGIB30M60TS-L SLLIMM 2nd series IPM," product documentation.*

[10] *Texas Instruments, "TMS320F2837xD Dual-Core Real-Time Microcontrollers," Data Sheet SPRS880P, revised Feb. 2024.*

[11] *TDK Electronics AG, "Ferrites and accessories—SIFERRIT material N27 and U/I cores," product and material documentation, 2022.*

[12] *Multicomp Pro, "ECW1.25 enamelled copper wire, 16 AWG, 1.17 mm² conductor area," Product No. 1230986, product data sheet.*

[13] *Ansys, Inc., "Ansys Electronics Desktop 2024 R2: Maxwell Help-Stranded Conductors and Loss Quantities," 2024.*

[14] *B. Zhao, Q. Song, and W. Liu, "Dead-Time Effect of the High Frequency Isolated Bidirectional Full-Bridge DCDC Converter: Comprehensive Theoretical Analysis and Experimental Verification," IEEE Transactions on Power Electronics, vol. 29, no. 4, pp. 1667-1680, 2014.*

[15] *F. Krismer and J. W. Kolar, "Accurate Power Loss Model Derivation of a High Current Dual Active Bridge Converter for an Automotive Application," IEEE Transactions on Industrial Electronics, vol. 57, no. 3, pp. 881-891, 2010, doi: 10.1109/TIE.2009.2025284.*

[16]*R. Manko, S. Čorović, and D. Miljavec, "Analysis and Design of Rotary Transformer for Wireless Power Transmission," in 2020 IEEE Problems of Automated Electrodrive. Theory and Practice (PAEP), Kremenchuk, Ukraine, 2020, pp. 1-6, doi: 10.1109/PAEP49887.2020.9240870.*

[17]*S. Botha and N. Gule, "Design and Evaluation of a Laminated Three-Phase Rotary Transformer for DFIG Applications," Energies, vol. 15, no. 11, Art. no. 4061, 2022, doi: 10.3390/en15114061.*

[18]*IEEE Std 1459-2025, IEEE Standard Definitions for the Measurement of Electric Power Quantities Under Sinusoidal, Nonsinusoidal, Balanced, or Unbalanced Conditions, IEEE, 2025, doi: 10.1109/IEEESTD.2025.11004570.*

[19]*H. Bai and C. Mi, "Eliminate Reactive Power and Increase System Efficiency of Isolated Bidirectional Dual active bridge DCDC Converters Using Novel Dual-Phase-Shift Control," IEEE Transactions on Power Electronics, vol. 23, no. 6, pp. 2905-2914, 2008, doi: 10.1109/TPEL.2008.2005103.*

[20]*S. Shao, M. Jiang, W. Ye, Y. Li, J. Zhang, and K. Sheng, "Optimal Phase-Shift Control to Minimize Reactive Power for a Dual Active Bridge DCDC Converter," IEEE Transactions on Power Electronics, vol. 34, no. 10, pp. 10193-10205, 2019, doi: 10.1109/TPEL.2019.2896224.*

[21]*S. Shao, H. Chen, X. Wu, J. Zhang, and K. Sheng, "Circulating Current and ZVS-on of a Dual Active Bridge DCDC Converter: A Review," IEEE Access, vol. 7, pp. 50561-50572, 2019, doi: 10.1109/ACCESS.2019.2911009.*

[22]*C.-S. Wang, G. A. Covic, and O. H. Stielau, "Power Transfer Capability and Bifurcation Phenomena of Loosely Coupled Inductive Power Transfer Systems," IEEE Transactions on Industrial Electronics, vol. 51, no. 1, pp. 148-157, 2004, doi: 10.1109/TIE.2003.822038.*

[23]*C.-S. Wang, O. H. Stielau, and G. A. Covic, "Design Considerations for a Contactless Electric Vehicle Battery Charger," IEEE Transactions on Industrial Electronics, vol. 52, no. 5, pp. 1308-1314, 2005, doi: 10.1109/TIE.2005.855672.*

[24]*Y. Teng, O. Anaya-Lara, R. Yazdanpanah, D. Campos-Gaona, and S. A. Mortazavizadeh, "Design and Analysis of a 100-kW Rotary Transformer for XROTOR Wind Generators," in 2023 IEEE Workshop on Electrical Machines*

Design, Control and Diagnosis (WEMDCD), Newcastle upon Tyne, UK, 2023, pp. 1-5, doi: 10.1109/WEMDCD55819.2023.10110930.

[25]*W. G. Hurley, W. H. Wölfle, and J. G. Breslin, "Optimised Transformer Design: Inclusive of High Frequency Effects," IEEE Transactions on Power Electronics, vol. 13, no. 4, pp. 651-659, 1998, doi: 10.1109/63.704133.*

[26]*W. G. Hurley, E. Gath, and J. G. Breslin, "Optimizing the AC Resistance of Multilayer Transformer Windings With Arbitrary Current Waveforms," IEEE Transactions on Power Electronics, vol. 15, no. 2, pp. 369-376, 2000, doi: 10.1109/63.838106.*

Chapter 5

5 Conclusions and Future Work

5.1 Summary of Research

This thesis investigates rotary transformer-based WPT as a contactless electrical interface between the rotating secondary generator structure and the stationary tower of the X-ROTOR wind turbine. The proposed interface combines a medium frequency rotary transformer with a phase-shift-controlled dual active bridge converter, allowing the magnetic and power electronic parts of the transfer stage to be considered together.

The research progresses from the system requirements to the electrical architecture, analytical design and experimental and numerical assessment of the RT-DAB interface. Chapter 1 defines the X-ROTOR operating conditions, rotor-to-tower installation requirements and the limitations associated with a sliding electrical interface. Chapter 2 establishes the two-channel secondary generator architecture and selects an inductive RT for the rotating power transfer interface. Chapter 3 develops the analytical RT-DAB design method and the original radial, NEW1, NEW2, L-type 1 and L-type 2 candidate geometries. Chapter 4 evaluates these designs using a reduced-scale experimental platform, an intermediate 600 V/100 kW electromagnetic study and a MW-class linked field-circuit model.

The three investigation levels serve different purposes. The reduced-scale platform provides experimental RT-terminal measurements under the 42 V, 20 kHz laboratory conditions. The intermediate study examines the analytical-to-FEM design route and the differences between 2D and 3D electromagnetic representations. The MW-class model compares the candidate RT geometries, winding parameters and turns arrangements under a common linked field-circuit boundary. The high power numerical

studies are therefore separate design investigations rather than scaled versions of the laboratory platform.

5.2 Answer to Research Questions

5.2.1 Research Question 1

Research Question 1: To what extent can an integrated RT-DAB interface support high power contactless power transfer across the mechanically constrained rotor-to-tower boundary of the X-ROTOR?

The reduced-scale RT-DAB platform provides experimental evidence of phase-shift-controlled contactless transfer through RT. The platform operates from a common 42 V DC source at 20 kHz with a nominal 1 mm assembled core-to-core airgap. The measured terminal quantities follow the commanded phase displacement and the corresponding changes in active and reactive power. Comparison with the prototype-matched model shows close correspondence in the terminal-voltage and fundamental power factor trends, while the simulated current magnitude remains lower than the measured value.

The intermediate 600 V/100 kW study provides the electromagnetic modelling step between analytical sizing and the MW-class assessment. The 2D and 3D models give closely corresponding terminal quantities and output power under the retained excitation, although larger differences occur in local flux density and core loss.

At MW class, the linked field-circuit model examines the interaction between the three-phase DAB and the five candidate RT geometries. Under the retained reference conditions, NEW2 gives an output power of 991.3189 kW, close to the nominal 1 MW transfer requirement. Taken together, the experimental and numerical results support the electrical and electromagnetic feasibility of the proposed RT-DAB interface within the investigated conditions. Full-scale mechanical, thermal, insulation and lifetime qualification remains outside the present study. The work associated with RQ1 provides the application-specific RT-DAB architecture for the X-ROTOR rotor-to-tower

electrical interface and a staged route for assessing its operation from laboratory measurements to MW-class numerical analysis.

5.2.2 Research Question 2

Research Question 2: How do candidate RT geometry, core airgap, winding-to-winding separation, winding fill factor, turns ratio and converter operating conditions affect transferred power, current behaviour, magnetic response and represented losses at the investigated MW-class operating points?

The candidate-geometry comparison shows that the original radial, NEW1, NEW2, L-type 1 and L-type 2 RTs present different electromagnetic characteristics to the same three-phase converter. Differences in magnetic path, winding position, leakage and local field distribution therefore produce different winding currents and transferred powers under the same converter command. A common phase-shift command does not correspond to equal electrical loading for the five geometries.

Core airgap, winding separation and winding fill factor affect the RT through different mechanisms. In the reduced-scale numerical study, increasing the core-to-core airgap reduces magnetic coupling and transferred power. In the MW-class winding-separation study, the topology-specific core gaps remain unchanged while the primary-to-secondary winding separation, δ_w, increases. The resulting reduction in coupling lowers winding current and transferred power, so the accompanying reduction in absolute winding loss occurs at a lower electrical loading.

The fixed-window fill-factor study retains the winding window, winding positions, core geometry and number of turns. Reducing k_f reduces the effective copper area and increases the represented winding resistance. The winding loss consequently increases for all five candidate geometries, even though the linked-circuit currents do not vary monotonically with k_f.

For the retained conditions $\delta_w = 5\,\text{mm}$ and $k_f = 0.60$, NEW2 gives $P_{\text{out}} = 991.3189\,\text{kW}$. The represented winding and core losses are 1.7865 kW and 8.7362 kW, giving a combined value of 10.5227 kW, approximately 1.06% of the corresponding output power. This value represents the combined RT winding- and core-loss

components rather than the DC to DC efficiency of the complete converter. NEW2 gives the preferred balance of transferred power and represented RT loss within the five investigated candidate geometries and the retained numerical conditions.

Turns ratio is treated as an additional RT design variable. Its principal quantified effect in the present model is the terminal-voltage scaling examined in RQ3. The work associated with RQ2 provides the controlled comparison of the application-driven RT geometries and separates the effects of core airgap, winding separation, effective copper occupation and converter loading.

5.2.3 Research Question 3

Research Question 3: Can voltage transformation be incorporated into the RT through winding turns-ratio selection while maintaining acceptable magnetic and converter operation?

The voltage-transformation study uses the selected NEW2 geometry. The primary winding remains at $N_p = 24$ turns, while the secondary winding is evaluated at $N_s = 24$ and $N_s = 48$. The magnetic geometry, winding-position boundary and linked-circuit operating conditions are retained between the two cases.

The simulated secondary-to-primary RMS voltage ratio is 0.981 for the 24:24 winding arrangement and 1.959 for the 24:48 arrangement. These values differ from the ideal ratios of 1 and 2 by −1.90% and −2.05%, respectively. The differences arise from the non-ideal electromagnetic and circuit behaviour represented in the linked model, including leakage flux, winding impedance and magnetising current.

The investigated RT therefore provides the expected voltage scaling through winding turns-ratio selection while remaining within the linked operating conditions used in the study. This introduces voltage transformation as an additional function of the RT-DAB interface. The 1:2 arrangement is assessed numerically, experimental assessment and insulation coordination at the corresponding full-scale voltage remain subjects for further work. The contribution under RQ3 is the integration of voltage transformation into the RT-DAB design through winding turns-ratio selection and its quantitative assessment for the investigated 1:1 and 1:2 arrangements.

Table 5.1 Traceability from research questions to methods, results and contributions

RQ	Method	Principal result	Contribution	Evidence
RQ1	System requirements, RT-DAB analytical design, reduced-scale experiment, intermediate FEM and MW-class linked field-circuit analysis	Phase-shift-controlled transfer is measured at reduced scale, NEW2 gives 991.3189 kW in the MW-class model	Application-specific RT-DAB architecture and staged evaluation route for the X-ROTOR rotor-to-tower interface	Experimental evidence applies to the reduced-scale platform, MW-class performance is numerical
RQ2	Candidate-geometry comparison, core-airgap study, winding-separation study and fixed-window fill-factor study	Geometry and winding parameters alter coupling, current, transferred power and represented losses, NEW2 gives the preferred result within the investigated candidate set	NEW1 and NEW2 geometries and controlled separation of core airgap, winding separation, copper occupation and converter loading	MW-class comparisons use linked field-circuit simulation and common converter commands
RQ3	NEW2 turns-ratio assessment using the linked field-circuit model	RMS voltage ratios of 0.981 and 1.959 are obtained for the investigated 1:1 and 1:2 winding arrangements	Integration of voltage transformation into the RT-DAB design	Numerical assessment, the 1:2 arrangement is not experimentally tested

5.3 Original Contributions and Novelty

The original contributions of the thesis are as follows:

1. An application-specific RT-DAB architecture for the X-ROTOR rotor-to-tower electrical interface.

   The architecture links the independently controlled secondary generator channels to a contactless medium frequency transfer stage between the rotating and stationary structures.
2. The application-driven NEW1 and NEW2 RT geometries.

These geometries introduce alternative magnetic return paths and winding arrangements within the X-ROTOR design space and are assessed against the original radial and two L-type reference structures.

3. A coupled RT-DAB design method.
   The method relates magnetic sizing, winding design, core airgap, winding separation, turns ratio and inductance to switching frequency, phase shift, converter current, transferred power and represented losses.
4. A staged analytical, numerical and experimental evaluation route.
   The reduced-scale experiment, intermediate electromagnetic study and MW-class linked field-circuit model provide complementary information at distinct investigation levels rather than being treated as scaled equivalents.
5. MW-class linked field-circuit assessment of the candidate RT-DAB designs.
   The model provides controlled comparisons of RT geometry, winding separation and fixed-window fill factor and incorporates winding turns ratio as a voltage-transformation variable.
   These contributions address the three research questions through the methods and results summarised in Table 5.1.

5.4 Classification of Evidence

Experimental evidence comes from the reduced-scale RT-DAB platform operating from a common 42 V DC source at 20 kHz with a nominal 1 mm assembled core-to-core airgap. The measurements provide primary- and secondary-side RT terminal voltages and currents together with FFT-derived power and power factor quantities. The experimental transfer metric reported in Chapter 4 is defined at the RT AC terminals and does not represent the total DC to DC efficiency of the complete converter system.

The remaining parameter studies are numerical. These include the reduced-scale core-airgap cases, the intermediate 2D/3D FEM comparison, the five MW-class candidate geometries, the winding-separation and fixed-window fill-factor studies and the NEW2 voltage-transformation assessment. The MW-class results are obtained

directly from the linked field-circuit model and are not derived by scaling the reduced-scale experimental platform.

At system level, the thesis relates the RT-DAB operating points to the variable X-ROTOR generator output and rotating DC interface. Full turbine operation over the wind-speed distribution, long-term maintenance benefit and lifetime performance require additional turbine-level and full-scale information and are not calculated from the present experimental or numerical results.

5.5 Limitations

A full-scale RT-DAB prototype is not included in this work. The reduced-scale platform provides experimental evidence of phase-shift-controlled transfer and RT-terminal behaviour, but it does not reproduce the voltage, current, thermal, insulation or mechanical conditions of the MW-class interface.

The MW-class electromagnetic study uses a 2D representation. The intermediate 2D/3D comparison quantifies the agreement in terminal quantities and the larger differences in local magnetic behaviour, but an equivalent 3D comparison is not performed for each MW-class candidate. The stranded-winding representation also excludes strand-level skin and proximity effects, and the electromagnetic and circuit models are not coupled to a complete thermal model.

The candidate geometries are compared mainly under common converter commands rather than equal output power. The NEW2 selection therefore applies to the investigated candidate set and retained numerical conditions. The study does not perform a formal global optimization.

The mechanical airgap is not coupled to a dynamic bearing and structural model. Eccentricity, vibration, thermal expansion, manufacturing tolerance and structural displacement require further coupled assessment. The discrete electrical operating points are also not combined with a complete X-ROTOR power curve, azimuth-dependent generator model, converter-efficiency map and site-specific wind-speed distribution, annual-energy and lifetime economic performance therefore remain outside the quantitative results of this thesis.

5.6 Future Work

Further development requires a coupled three-dimensional electromagnetic, thermal and mechanical model of the selected RT arrangement. The model should include topology-specific three-dimensional magnetic effects, conductor AC loss, temperature-dependent behaviour, insulation requirements and the airgap variation produced by the bearing and supporting structure.

A higher-power experimental platform is required to extend the present measurements towards the intended electrical and thermal operating range. Measurements of winding and core loss, leakage inductance, temperature rise and the 1:2 voltage-transformation arrangement would provide direct comparison with the corresponding numerical results. Dynamic eccentricity and misalignment can subsequently be included in both the electromagnetic model and experimental assessment.

The candidate RTs can also be compared under equal-output power and thermal constraints to complement the common-command results. Further converter studies can address circulating current, reactive power and semiconductor loading over the partial-load range. Combining the resulting RT-DAB operating map with the X-ROTOR aerodynamic power variation, azimuth-dependent secondary generator behaviour and site-specific wind-speed distribution then allows annual-energy and longer-term system performance to be assessed.

5.7 Conclusion

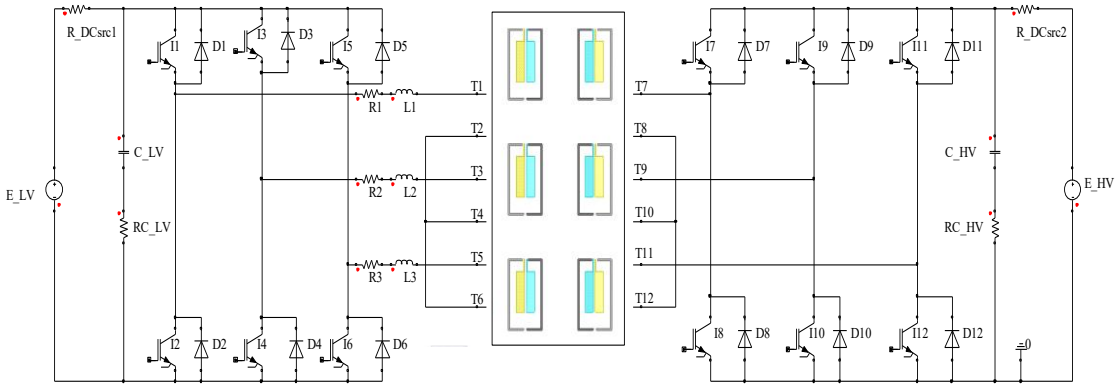
The results support the RT-DAB as a contactless power-transfer interface for the X-ROTOR rotor-to-tower boundary. Reduced-scale experiments confirm phase-shift-controlled transfer, while the intermediate and MW-class studies characterise the RT electromagnetic response and converter interaction; NEW2 is retained as the preferred geometry within the investigated set, and the turns-ratio study gives voltage ratios close to the ideal values. Full-scale implementation requires further mechanical, thermal, insulation, environmental and lifetime assessment.

Appendix

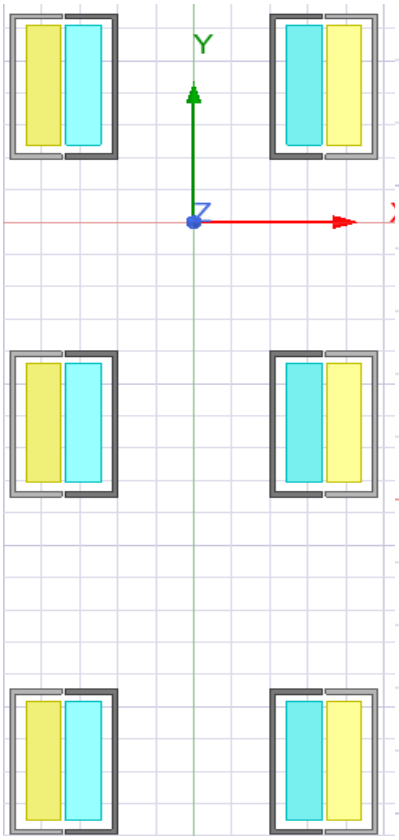
The appendices provide supplementary implementation material supporting the numerical and experimental investigations presented in the main body of the thesis. They are presented outside the numbered chapter structure so that additional model and post-processing details can be retained without interrupting the main technical narrative. Appendix A provides supplementary information on the MW-class linked field-circuit implementation, while Appendix B provides the MATLAB FFT routine used for processing the reduced-scale experimental waveforms.

Appendix A MW-Class Linked field circuit model

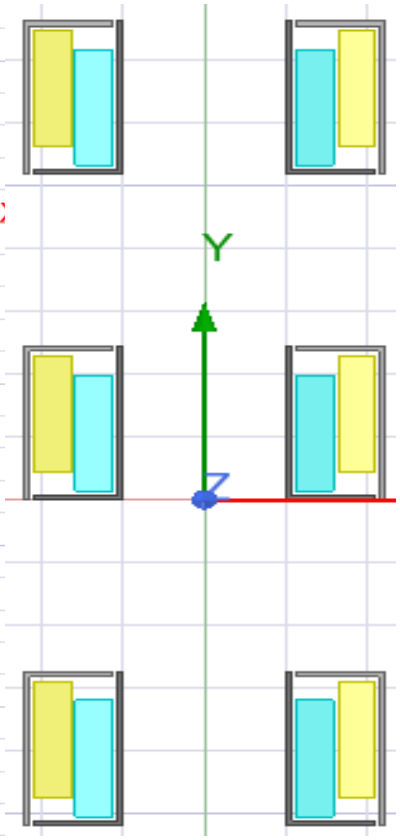
This appendix provides supplementary graphical information for the MW-class RT-DAB investigation presented in Section 4.4. Figure Appendix 1 illustrates the coupling between the Ansys Maxwell electromagnetic model and the external Simplorer circuit used for the linked field-circuit simulation described in Section 4.4.1. Figure Appendix 2 presents the 2D electromagnetic representations of the five candidate RT geometries used in the MW-class comparison.



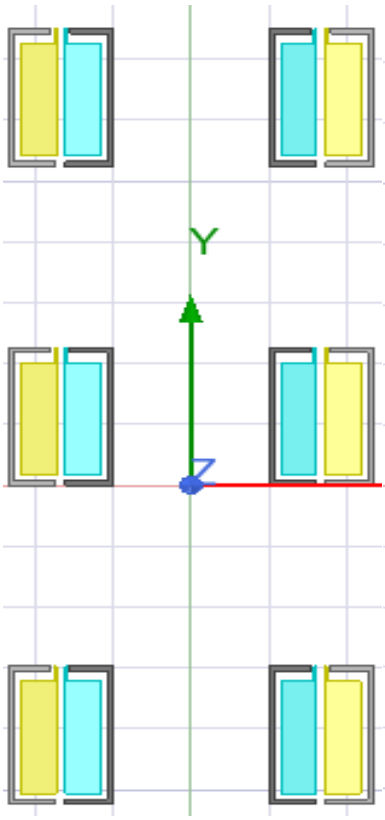
Appendix 3 Coupling relationship between the Finite Element RT model and the external power electronic circuit



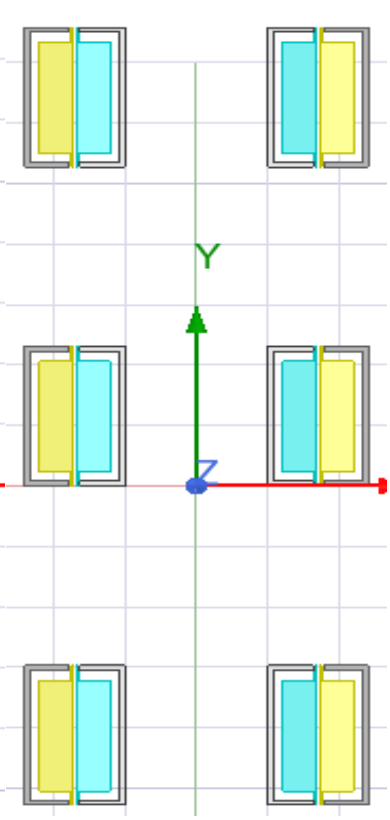
(a) Original type



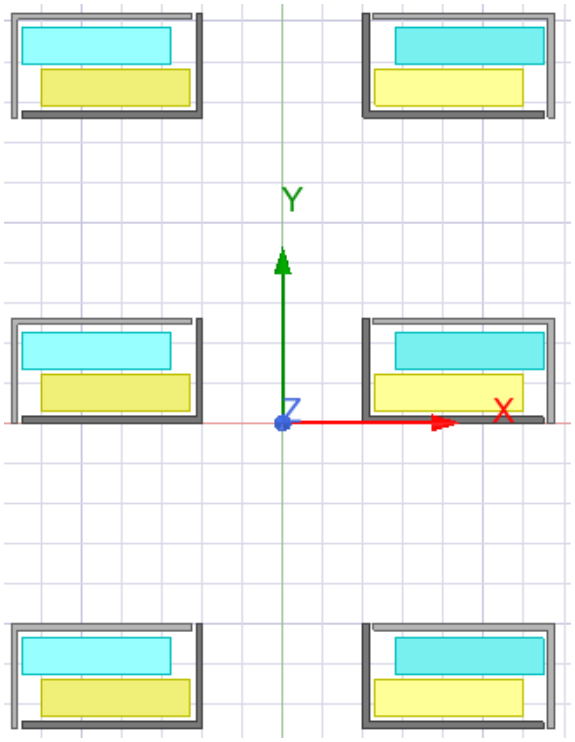
(b) L-type 2



(c) NEW1



(d) NEW2



(e) L type1

Appendix 4 2D electromagnetic models of the five-candidate MW-class rotary transformers used in the three-phase RT-DAB investigation: (a) Original radial, (b) NEW1, (c) NEW2, (d) L-type 1 and (e) L-type 2.

Appendix B Experimental FFT post processing

This Appendix provides the MATLAB FFT routine used for the reduced-scale experimental analysis presented in Section 4.2.3. The routine processes the measured primary- and secondary-side RT voltage and current waveforms exported from the oscilloscope and extracts their fundamental components at the 20 kHz switching frequency.

The extracted fundamental RMS phasors are used to obtain the corresponding primary- and secondary-side active and reactive power components. The subsequent power factor and baseline-referenced performance quantities are calculated using the definitions given in Section 4.2.3 and are therefore not repeated in this appendix.

The MATLAB routine used for this processing is provided below.

```
%% Transformer FFT and Power Calculation
% This script:
%  - Reads time-domain data for Vp, Vs, Ip, Is from 0_deg.xlsx
%  - Computes FFT and extracts the fundamental (2000 Hz) phasors
%  - Computes primary and secondary active and reactive power
clear; clc; close all;
%% User parameters
filename = '90_dgree_15mm.xlsx';    % Excel file name
f0       = 20000;            % Fundamental frequency [Hz]
%% Read data
T  = readtable(filename);
t  = T.('time_s_');              % time in seconds
Vp = T.('Vp_acVoltage__V_');    % primary voltage
Vs = T.('Vs_acVoltage__V_');    % secondary voltage
Ip = T.('Ip_A_');                % primary current
Is = T.('Is_A_');                % secondary current
%% Sampling info
dt = mean(diff(t));
Fs = 1/dt;        % sampling frequency
N  = length(t);   % number of samples
fprintf('Sampling frequency: %.3f kHz\n', Fs/1e3);
% Frequency axis for FFT
f = (0:N-1)*Fs/N;
%% FFTs of each signal
Vp_fft = fft(Vp);
Vs_fft = fft(Vs);
Ip_fft = fft(Ip);
Is_fft = fft(Is);
%% Find FFT bin closest to fundamental frequency
[~, idx_f0] = min(abs(f - f0));
f0_eff = f(idx_f0);  % actual frequency of that bin
fprintf('Fundamental (requested): %.1f Hz, FFT bin at: %.3f Hz (index %d)\n', ...
        f0, f0_eff, idx_f0);
%% Convert FFT bin value to RMS phasor
% For a pure sinusoid v(t) = sqrt(2)*Vrms*cos(ωt + φ),
% the positive-frequency DFT bin X(k0) satisfies:
% Vrms * exp(jφ) = (2/(N*sqrt(2))) * X(k0)
scale = 2/(N * sqrt(2));
```

```
Vp1 = scale * Vp_fft(idx_f0);   % primary voltage phasor (RMS)
Vs1 = scale * Vs_fft(idx_f0);   % secondary voltage phasor (RMS)
Ip1 = scale * Ip_fft(idx_f0);   % primary current phasor (RMS)
Is1 = scale * Is_fft(idx_f0);   % secondary current phasor (RMS)
%% Magnitude and angle (in degrees)
Vp_mag = abs(Vp1);   Vp_ang = rad2deg(angle(Vp1));
Vs_mag = abs(Vs1);   Vs_ang = rad2deg(angle(Vs1));
Ip_mag = abs(Ip1);   Ip_ang = rad2deg(angle(Ip1));
Is_mag = abs(Is1);   Is_ang = rad2deg(angle(Is1));
% V–I phase shifts
phi_p = Vp_ang - Ip_ang;   % primary Vp–Ip phase angle [deg]
phi_s = Vs_ang - Is_ang;   % secondary Vs–Is phase angle [deg]
%% Complex powers (single-phase)
% S = V * conj(I)  (RMS phasors)
Sp = Vp1 * conj(Ip1);   % primary complex power
Ss = Vs1 * conj(Is1);   % secondary complex power
Pp = real(Sp);   % primary active power [W]
Qp = imag(Sp);   % primary reactive power [var]
Ps = real(Ss);   % secondary active power [W]
Qs = imag(Ss);   % secondary reactive power [var]
%% Display results
fprintf('\n=== PRIMARY SIDE ===\n');
fprintf('Vp1 = %.4f V_rms ∠ %.2f°\n', Vp_mag, Vp_ang);
fprintf('Ip1 = %.4f A_rms ∠ %.2f°\n', Ip_mag, Ip_ang);
fprintf('V–I phase angle (Vp-Ip) = %.2f°\n', phi_p);
fprintf('Pp = %.4f W\n',  Pp);
fprintf('Qp = %.4f var\n', Qp);
fprintf('\n=== SECONDARY SIDE ===\n');
fprintf('Vs1 = %.4f V_rms ∠ %.2f°\n', Vs_mag, Vs_ang);
fprintf('Is1 = %.4f A_rms ∠ %.2f°\n', Is_mag, Is_ang);
fprintf('V–I phase angle (Vs-Is) = %.2f°\n', phi_s);
fprintf('Ps = %.4f W\n',  Ps);
fprintf('Qs = %.4f var\n', Qs);
%% Optional: spectra plots to *see* magnitude and phase
doPlots = true;
if doPlots
   signals = {Vp, Vs, Ip, Is};
```

```
    names   = {'Vp', 'Vs', 'Ip', 'Is'};
    fmax_plot = 600e3; % show up to 20 kHz
    for k = 1:numel(signals)
        X = fft(signals{k});
        figure('Name',['Spectrum of ', names{k}]);
        subplot(2,1,1);
        plot(f/1e3, abs(X)/N);
        xlim([0 fmax_plot/1e3]);
        grid on;
        xlabel('Frequency (kHz)');
        ylabel('|X(f)| (linear)');
        title(['Magnitude spectrum of ', names{k}]);
        subplot(2,1,2);
        plot(f/1e3, unwrap(angle(X))*180/pi);
        xlim([0 fmax_plot/1e3]);
        grid on;
        xlabel('Frequency (kHz)');
        ylabel('Phase (deg)');
        title(['Phase spectrum of ', names{k}]);
    end
end
```